Deposit & Copying of Hardbound Dissertation Declaration

UNIVERSITY OF CAMBRIDGE

Board of Graduate Studies

Please note that you will also need to bind a copy of this Declaration into your final, hardbound print copy of your dissertation - this has to be the very first page of the hardbound dissertation. Do not include this form in the electronic version of your dissertation.

1 Surname (Family Name)	Forenames(s)	Title

2 Title of Dissertation as approved by the Degree Committee

In accordance with the University Regulations in *Statutes and Ordinances* for the PhD, MSc and MLitt Degrees, I agree to deposit one or more copies of my dissertation and summary with the Secretary of the Board of Graduate Studies in a form or forms approved by the Board. The Secretary of the Board of Graduate Studies shall deposit a hardbound print copy of my dissertation and summary in the University Library under the following terms and conditions:

1. Dissertation Author Declaration

I am the author of this dissertation and hereby give the University the right to make my dissertation available in print form as described in 2. below.

My dissertation is my original work and a product of my own research endeavours and includes nothing which is the outcome of work done in collaboration with others except as declared in the Preface and specified in the text. I hereby assert my moral right to be identified as the author of the dissertation.

The deposit and dissemination of my dissertation by the University does not constitute a breach of any other agreement, publishing or otherwise, including any confidentiality or publication restriction provisions in sponsorship or collaboration agreements governing my research or work at the University or elsewhere.

2. Access to Dissertation

I confirm that I have selected an appropriate access and permission usage level for my dissertation, which is detailed on the Access Confirmation Form that I submitted with the electronic version of my dissertation. I understand that one print copy of my dissertation will be deposited in the University Library for archival and preservation purposes, and that, unless upon my application an embargo or restricted access has been granted for a specified period of time by my Supervisor or Degree Committee respectively prior to this deposit, the dissertation will be made available by the University Library for consultation by readers in accordance with University Library Regulations and copies of my dissertation may be provided to readers in accordance with applicable legislation, or on other access and permission usage terms detailed on my Access Confirmation Form and/or as may be marked on the dissertation.

3. Agreement to terms

By including this Declaration in my Hardbound Dissertation I confirm that any statements on this Declaration are correct and that I agree to the terms for access to my dissertation.

General Device Integration Strategies for Two-Dimensional Materials

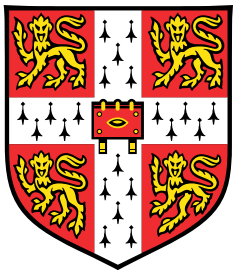

Ruizhi Wang

Department of Engineering
University of Cambridge

This dissertation is submitted for the degree of
Doctor of Philosophy

Pembroke College November 2018

For Xiaoqin, Noemie and Zhenggui.

Declaration

I hereby declare that except where specific reference is made to the work of others, the contents of this dissertation are original and have not been submitted in whole or in part for consideration for any other degree or qualification in this, or any other university. This dissertation is my own work and contains nothing which is the outcome of work done in collaboration with others, except as specified in the text and Acknowledgements. This dissertation contains fewer than 65,000 words including appendices, bibliography, footnotes, tables and equations and has fewer than 150 figures.

Ruizhi Wang
November 2018

Acknowledgements

First, I would like to thank Prof. Hofmann for his support, guidance and all the discussions that took much longer than expected. Also, I would like to thank everyone in the group for the great company. But most of all I would like to thank Noemie, Zhenggui and Xiaoqin for always believing in me. Without them this work would not have been possible.

Publications

Already published

1. **R. Wang**, P. R. Whelan, P. Braeuninger-Weimer, S. Tappertzhofen, J. A. Alexander-Webber, Z. A. Van-Veldhoven, P. R. Kidambi, B. S. Jessen, T. J. Booth, and P. Boggild, "Catalyst interface engineering for improved 2D film lift-off and transfer," *ACS Applied Materials & Interfaces*, 2016.

2. **R. Wang**, D. Purdie, Y. Fang, F. Massabuau, P. Braeuninger-Weimer, J. Burton, R. Blume, R. Schloegel, A. Lombardo, R. Weatherup, and S. Hofmann, "A peeling approach for integrated manufacturing of large mono-layer h-BN crystals," *ACS Nano*, 2019.

3. P. Braeuninger-Weimer, S. Funke, **R. Wang**, P. Thiesen, D. Tasche, W. Viöl, and S. Hofmann, "Fast, Non-Contact, Wafer-scale, Atomic Layer Resolved Imaging of 2D Materials by Ellipsometric Contrast Micrography," *ACS Nano*, vol. 12, no. 8, pp. 8555–8563, 2018

4. P. R. Whelan, K. Iwaszczuk, **R. Wang**, S. Hofmann, P. Bøggild, and P. U. Jepsen, "Robust mapping of electrical properties of graphene from terahertz time-domain spectroscopy with timing jitter correction," *Optics Express*, vol. 25, no. 3, pp. 2725–2732, 2017.

5. P. R. Whelan, B. S. Jessen, **R. Wang**, B. Luo, A. C. Stoot, D. M. A. Mackenzie, P. Braeuninger-Weimer, A. Jouvray, L. Prager, and L. Camilli, "Raman spectral indicators of catalyst decoupling for transfer of CVD grown 2D materials," *Carbon*, vol. 117, pp. 75–81, 2017.

6. S. J. Cartamil-Bueno, M. Cavalieri, **R. Wang**, S. Houri, S. Hofmann, and H. S. J. van der Zant, "Mechanical characterization and cleaning of CVD single-layer h-BN resonators," *npj 2D Materials and Applications*, vol. 1, no. 1, p. 16, 2017.

7. A. Crovetto, P. R. Whelan, **R. Wang**, M. Galbiati, S. Hofmann, and L. Camilli, "Non-destructive thickness mapping of wafer-scale hexagonal boron nitride down to a monolayer," *ACS Applied Materials & Interfaces*, 2018.

8. J. J. Velasco-Vélez, V. Pfeifer, M. Hävecker, **R. Wang**, A. Centeno, A. Zurutuza, G. Algara-Siller, E. Stotz, K. Skorupska, and D. Teschner, "Atmospheric pressure X-ray photoelectron spectroscopy apparatus: Bridging the pressure gap," *Review of Scientific Instruments*, vol. 87, no. 5, p. 53121, 2016.

9. J. A. Alexander-Webber, A. A. Sagade, A. I. Aria, Z. A. Van Veldhoven, P. Braeuninger-Weimer, **R. Wang**, A. Cabrero-Vilatela, M.-B. Martin, J. Sui, and M. R. Connolly, "Encapsulation of graphene transistors and vertical device integration by interface engineering with atomic layer deposited oxide," *2D Materials*, vol. 4, no. 1, p. 11008, 2016.

10. S. Caneva, R. S. Weatherup, B. C. Bayer, R. Blume, A. Cabrero-Vilatela, P. Braeuninger-Weimer, M.-B. Martin, **R. Wang**, C. Baehtz, R. Schloegl, J. C. Meyer, and S. Hofmann, "Controlling catalyst bulk reservoir effects for monolayer hexagonal boron nitride CVD," *Nano Letters*, vol. 16, no. 2, pp. 1250–1261, 2016.

In submission

11. R. Weatherup, **R. Wang**, P. Braeuninger-Weimer, S. Caneva, R. Blume, R. Schloegl, and S. Hofmann, "Controlling the Structure of Bi-layer Graphene by Combining Isothermal Growth with Kinetically-determined Carbon Precipitation on Cooling," *Nano Letters*, In submission.

12. P. Braeuninger-Weimer, O. Burton, R. Weatherup, **R. Wang**, P. Dudin, B. Brennan, A. Pollard, B. Bayer, V. Veigang-Radulescu, J. Meyer, B. Murdoch, P. Cumpson, and S. Hofmann, "Reactive Intercalation and Dielectric Layer Formation at the Buried Graphene-Germanium Interface," *ACS Applied Materials & Interfaces*, In submission.

Abstract

General Device Integration Strategies for Two-Dimensional Materials

Ruizhi Wang

Despite the extraordinary wealth of unique properties of 2D layered materials (2DLM), no large scale commercial application has been achieved so far. The central challenge hereby is the scalable manufacture of these materials. While mechanical exfoliation, also famously known as the scotch-tape method, leads to materials of extremely high quality, the method itself is non-scalable due to the highly stochastic deposition yield. Major advancement has been achieved in recent years regarding the scalable production of 2DLMs, especially using chemical vapour deposition (CVD). It is now common to produce large areas of graphene (Gr) or hexagonal boron nitride (h-BN), which are two members of the family of 2DLMs, in the laboratory using CVD. Often the only limit to the size of the sample is dictated by the dimensions of available equipment. Most studies have targeted the improvement of the quality of the grown material. The focus hereby has been the growth of ever-larger single-crystalline regions by lowering the nucleation density or by merging aligned domains.

Most studies fail to acknowledge the actual key challenge. Nearly all emerging applications require the integration of 2DLMs into stacks of so called van der Waals heterostructures and their deposition onto insulating substrates. Since direct deposition of such structures on dielectrics has been proven to be an elusive goal, the most promising approach so far is the growth of 2DLMs on a catalyst with a subsequent transfer to the target substrate. The bottleneck of this approach has been the lack of sufficient transfer methods. A number of these have been proposed for CVD Gr and h-BN. Still the introduction of contamination and damage remain major constraints, which is exceptionally severe in case of heterostructures that rely on atomically clean interfaces. 2DLMs will only be a true candidate for commercial applications if sufficiently clean transfer methods are found that will enable large scale fabrication.

The work presented in this thesis addresses this challenge in two ways. The first is to develop new and improved transfer methods for existing combinations of 2DLM and catalyst. Thereby the aim is to base the method on a detailed understanding of their interaction and thus to devise a general rationale for transfer. The proposed method, which is referred to as Lift-Off Transfer (LOT), makes use of the weak interaction between 2DLMs and certain types of catalysts. It is shown how intercalation processes result in the local oxidation of the substrate followed by selective oxide dissolution, which releases the 2DLM film. Not only is the method highly versatile, but it also yields Gr and h-BN films of high quality compared to traditional transfer methods without requiring additional post-transfer annealing. While LOT is a significant improvement over existing transfer method, it still requires bringing the 2DLM into contact with a solution, which is a potential source of contamination.

It has been demonstrated, that CVD Gr, when processed using optimized methods, will show similar performance as mechanically exfoliated Gr. While these results are a promising first step towards more scalable processes, it still relies on mechanically exfoliated h-BN, which acts as a stamp that is used to delaminate the Gr from the growth catalyst. Thus, the focus is shifted on how to process and transfer CVD h-BN, which can then be used as the initial capping layer for the transfer of further layers of 2DLMs. To that end, an improved deposition process of h-BN has been developed that allows the growth of h-BN with individual domain exceeding 0.5 mm. More importantly, these h-BN films can be easily transferred using an entirely delamination based approach that makes use of the weak interaction between the specifically chosen catalyst and the h-BN. This enables the sequential pick up additional layers to create multilayer h-BN with atomic precision, and also direct fabrication h-BN/Gr heterostructures.

Based on a thorough understanding of the interaction between 2DLMs and their substrate, this thesis presents new strategies for device integration. Hereby not only a method is proposed that is an incremental improvement over existing ones, but an entirely new approach is presented that enables the clean and scalable device integration of 2DLMs. This work paves the path for future large scale applications of 2DLMs.

Table of contents

Chapter 1

Introduction

"There is plenty of room at the bottom" was the title of the famous lecture given by Richard Feynman in the 1960s. In this lecture, he presented his vision of a world, where it is possible for humans to manipulate matter at the smallest atomic scale. He outlines how the consequences of such a technology would fundamentally change every aspect of our lives, from materials to electronics and even medicine. The key to this development is continuous miniaturization.

Nanotechnology has been from the onset a race to the so-called "bottom". The unparalleled developments in computing have come to epitomise the sheer incredible possibilities of fabrication at ever smaller scales. By making more and more devices in an ever small area, it has been possible to improve the performance of computers exponentially during the last decades. At the heart of this process lies our understanding of how to manipulate matter with higher precision and at increasingly smaller scales. The advancement of characterization techniques such as scanning probe and electron microscopy has enabled the research on ever-smaller structures and further down-scaling.

The ultimate limit of moving further to smaller structures is embodied by two-dimensional layer materials (2DLM), i.e. materials that are atomically thin in one dimension, but are practically of macroscopic size in the other two dimensions. Graphene, the first discovered material of this family, consists of a single layer of carbon atoms, which is also the smallest atom that forms a solid at room temperature. Thus, it is the thinnest physically possible structure. Despite being seemingly fragile, these materials were revealed to be surprisingly stable and easy to handle. Not only was a new class of materials suddenly available, but these could be processed at ease on the laboratory bench. The initial discovery and the realization of the unique properties of these materials led to an extraordinary increase in research efforts,

linked with many promises for potential applications. However, more than a decade on, these materials have still not left the laboratories. Most of the early research did not anticipate the challenge of scalability. The key in this context is the large scale production and device integration of these materials.

One of the reasons Gr has become so well-known even in popular science is related to the way it was initially synthesized. Using extremely simple everyday tools it was possible to obtain Gr, through a process called mechanical exfoliation and to perform ground-breaking research on it [1]. The fact that these researchers went on to win the Nobel Prize contributed even more to the myth surrounding Gr . Since this initial discovery more than a decade ago, researchers discovered many other two dimensional materials and have developed a multitude of sophisticated devices and uncovered a wealth of unique properties [2–7].

All the aforementioned results have in common that they still rely on the initial method of mechanical exfoliation for the synthesis of two-dimensional material. Mechanical exfoliation results in inhomogeneous, random small flakes of material. It is not scalable and the material obtained in such way is extremely challenging to integrate into devices. However, it has one advantage: It offers an atomically clean surface. Wolfgang Pauli is famously credited with the quote: “God made the bulk; surfaces were invented by the devil.”, which summarises in a humorous way the difficulties associated with surfaces in research. 2DLM consist practically only of surface. Thus, they are extremely sensitive to the environment and any potential source of contamination. The biggest challenge of experiments has always been clean processing, which is the sole and biggest advantage of mechanical exfoliation.

For any industrial scale application to emerge, a different method of creating 2DLM is imperative. In the recent years, methods have emerged for scalable production. The challenge now is to combine the new production processes with methods of device integration. The focus of the years to come will be the optimization of processes towards applications, which is also the topic of this thesis. The potential outcome of these efforts will be the key to finally unlock the potential applications of 2DLM .

1.1 A New Flat World

No physical object is truly two-dimensional. 2DLM are named as such mainly to illustrate their geometrical structure, where the size in one dimension is of atomic scale, whereas the size in the other two dimensions is of macroscopic scale. In nature, these 2DLM are usually

found as stacked layers within a bulk crystal. Thus, the adjective “layered” is commonly used as part of the name for this class of materials

Some 2DLMs consist of a single layer of atoms arranged in a plane, while others consist of three layers of atoms. A better definition is given by the electronic structure of these materials, as the wavevectors of the electrons are confined to two dimensions. All these materials have in common that within the horizontal plane, the materials are bound covalently, while they interact with other materials only through relatively weak van der Waals (vdW) interaction. Fig. 1.1 shows the lattice structure of Gr and hexagonal boron nitride, two common examples of 2DLMs.

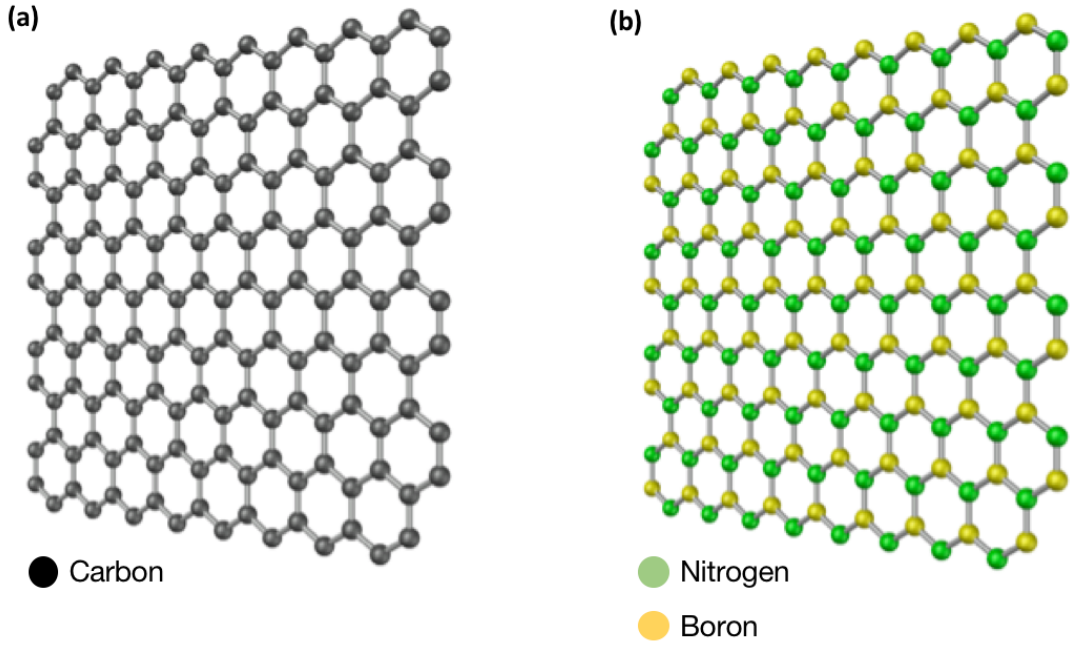

Fig. 1.1 Schematic lattice model of **(a)** Gr and **(b)** hexagonal boron nitride. Each sphere symbolizes an atom of the respective element. All bonds are covalent and in plane, as represented by the links between the atoms.

Generally speaking there are two groups of 2DLMs. One group includes materials that are made up of atoms of a single element, which are bound covalently. Examples are Gr and phosphorene. The other group includes materials consisting of multiple elements. A large set of 2DLMs containing various elements have been identified. The family of 2DLMs includes conductors, semi-metals, semiconductors and insulators.

Beside the unique individual properties of 2DLMs, it is possible to create what is being referred to as van der Waals heterostructures, i.e. stacks of different 2DLMs assembled with atomic precision. The first of these novel composites was created by stacking Gr and h-BN

[3]. The properties of a heterostructure are often more than just the sum of the properties of the constituents. For example by stacking two layers of Gr, which is not a superconductor on its own, it is possible to create a superconductor [8]. Most of the research has focused on heterostructures with embedded Gr, mostly due to the existing experience and the ease of experimental processing (some types of 2DLMs are sensitive to air and/or humidity).

There are two main reasons for the excitement about 2DLMs in the research community. The most straightforward one is that it has become possible to work with individual layers of atoms on the tabletop. Especially when using mechanical exfoliation as a way of synthesis, it is extremely easy and only requires very simple tools. But the main reason is that with heterostructures it has suddenly become possible to perform truly atomic scale assembly. Individual 2DLMs often possess interesting properties, which, can however be found in conventional bulk materials. In contrast, heterostructures really enable devices that outperform classical ones. Thus, the attention and the direction of research has been to fabricate ever more complex heterostructures for a multitude of different applications, with extraordinary characteristics unmatched by conventional materials [3–5, 7, 9, 10].

1.2 Methods of Manufacturing 2D Layered Materials

The initial discovery of 2DLMs was made with the synthesis of Gr using mechanical exfoliation. The fact that this method, which is so simple and is carried out using tools that most people have at home, played an important role in why Gr became such a widely discussed topic even outside the scientific community. Mechanical exfoliation is in fact an established method that is even used in introductory experimental physics classes for preparing samples for scanning probe microscopy. The process is outlined in Fig. 1.2 (a) and optical images in Fig. 1.2 (b) show an actual sample. It starts with a bulk crystal of the respective layered material, which is repeatedly peeled with adhesive tape. It is evident that the transfer onto the target substrate is extremely inhomogeneous. Flakes are randomly deposited on the substrate, including atomic monolayers, but also much thicker ones. Through a tedious process, flakes with the required thickness have to be searched relying only on the specific optical contrast [11].

The main reason that mechanical exfoliation is still one of the most popular methods for making devices is the fact that the obtained 2DLM has atomically clean surfaces. During the process, it comes into contact with nothing but the bulk crystal itself (not the entire flake that is peeled off is deposited, but only a few layers with some remaining on the tape). Thus, any form of contamination is minimized. Significant research efforts have been invested to

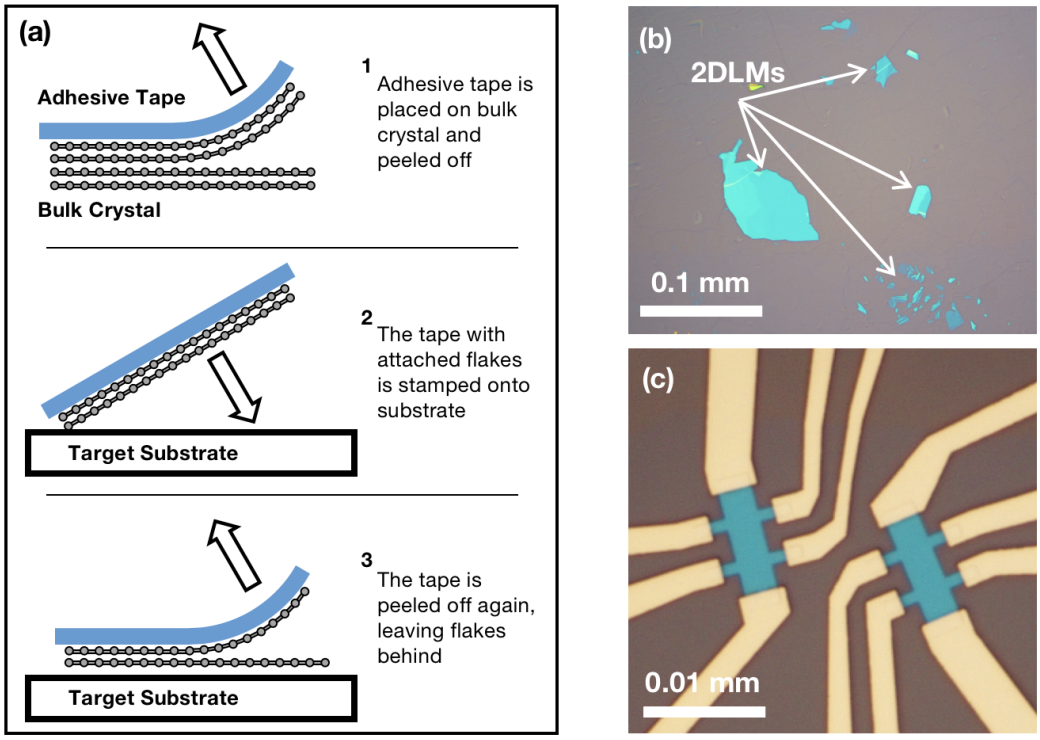

Fig. 1.2 **(a)** Schematic process of mechanical exfoliation. **(b)** Flakes of h-BN of different thicknesses on a SiO_2/Si wafer. **(c)** Final device after fabrication

improve this method [12] and even attempts have been made to automate the process [13]. Nonetheless, this method is inherently non-scalable due to the statistical process of layer deposition onto the substrate. Thus it is incompatible to industrial production, considering that large scale fabrication requires billions of devices to be produced. Already shortly after the discovery of how to exfoliate Gr, it became obvious that methods are required to improve scalable fabrication. Fig. 1.3 presents a non-exhaustive overview of the methods that have been developed, which will be discussed briefly in the following.

Liquid Phase Exfoliation Bulk crystals of the 2DLM to be synthesized are dispersed in a solution. This method was first used for the production of Gr [15], but has since been applied to produce various other 2DLMs [16]. The disadvantege of liquid exfoliation is that flakes obtained through liquid exfoliation are inhomogeneous in thickness and the size of the individual flakes is only on the order of µm [15]. Even given an ideal process, ultimately the size of individual flakes is limited by the size of the bulk crystal, which in the case of graphite is only on the order of centimeters [17]. However, it is relatively simple and does not require expensive equipment. Furthermore, it can easily be scaled up to produce large amounts of

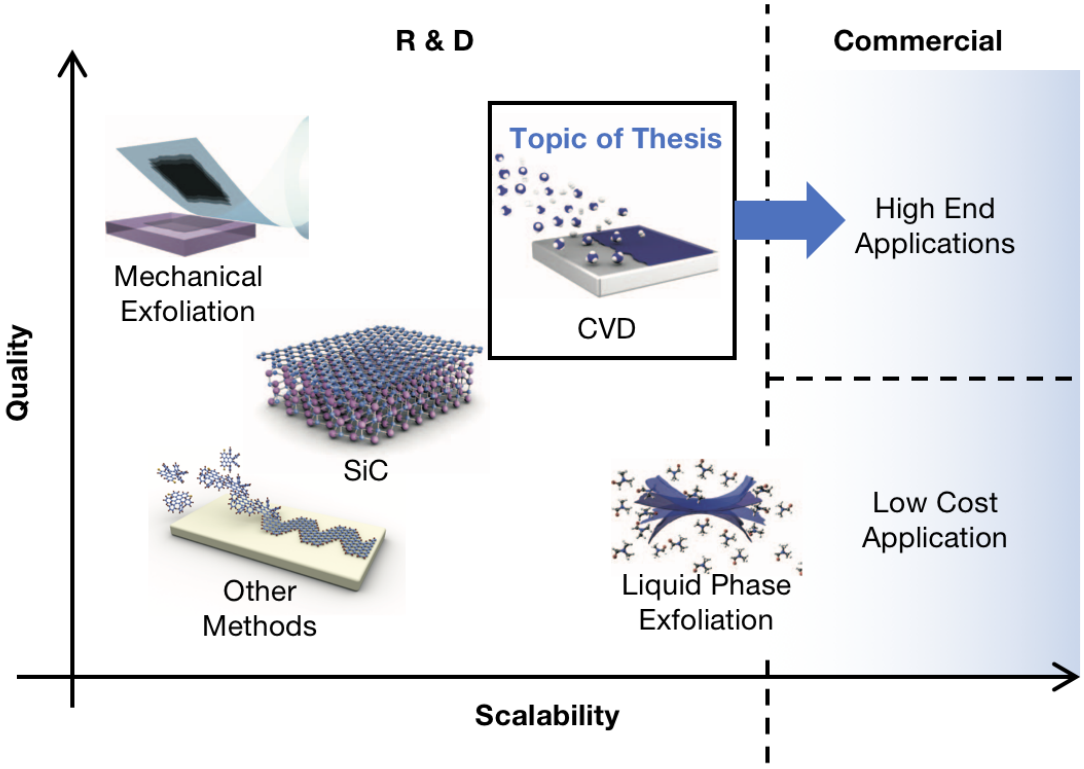

Fig. 1.3 Schematic, non-exhaustive overview comparing the existing methods of creating 2DLMs. Adapted from reference [14]

material [18]. The main advantage is that the 2DLMs obtained through liquid exfoliation can be very easily processed for example through printing [19]. Thus, this method is very attractive for low-performance applications that are very price sensitive.

Chemical Vapour Deposition (CVD) In CVD, the material of choice is deposited on a large scale by reacting a suitable gaseous precursor with a substrate at elevated temperatures [20]. It is used frequently for the growth of semiconductors in industrial processes, but also in research for nanomaterials such as nanotubes [21, 22] and nanowires [23]. CVD of 2DLMs was first demonstrated for Gr [24, 25, 17] and was soon expanded to many other materials [26–29]. It is possible to perform CVD of 2DLMs directly on the device substrate, which is often a dielectric.[30, 31]. However, most processes make use of a catalytic substrate, which has two advantages. It enables growth at lower temperatures, as the precursor dissociation requires less activation energy. Furthermore, the presence of a first layer will reduce the catalytic activity and thus allow some control over the deposition thickness, although careful tuning of the process parameters is usually required to achieve a homogeneous 2DLM film.

The disadvantage is that device integration often requires the transfer onto an insulating substrate. This method is discussed in greater detail in Chapter 2.

Other Methods A large number of other methods exists for the synthesis of 2DLMs. Sometimes a certain method is limited to one specific type of material. For example thermal desorption of silicon (Si) from silicon carbide (SiC) is an established method of producing Gr over large areas [32, 33] . The material is of high quality and can be directly used on the growth substrate [34]. However, the main drawback is the excessive cost of SiC wafers. Many additional processes have been suggested for the growth of 2DLMs [35, 36], including methods like molecular beam epitaxy [37] or growth by catalytic transformation of solid sources [38–40] . However, most of these processes cannot be scaled sufficiently or can only produce materials of low quality

The two most generally applicable and scalable methods are liquid exfoliation and CVD. Compared to liquid exfoliation, CVD requires more expensive, albeit already available, equipment. The cost during production is mainly related to the applied catalyst and whether it can be reused. The lateral dimension of the layers is practically only limited by the size of the reactors [41].

1.3 Challenges to Wide-Spread Application

Of all the methods of large scale synthesis of 2DLMs, catalytic CVD has emerged as the most promising route for scaling up production for high-end electronics applications [14, 17]. In fact it has been demonstrated that the quality of CVD grown 2DLMs is on-par with ones obtained through mechanical exfoliation, which is considered to generate the highest quality devices [42]. However, this is only the case if the device integration of the 2DLM is carried out in an optimized process that preserves a pristine surface.

In general there are two different approaches towards device integration. The most straightforward approach is to directly perform CVD on the device substrate. Unfortunately, there are many issues associated with this process. In order to break down the precursor in the absence of a catalyst, often very high temperatures of up to 1600 °C are required [43, 44]. This obviously limits the types of substrates that can be used. Furthermore, films often lack layer control and the material is of poor quality [44, 45]. The other approach is to grow via CVD on a suited metal catalyst and to transfer after initial deposition if required. A

range of different transition metals have been used for the successful growth of high quality 2DLMs [24–26, 46, 47, 17, 48]. In the ideal case, the growth substrate is also the device substrate [49, 50]. This is often not the case, which means that a transfer from the catalyst is required. The additional step of transfer does not necessarily pose a problem. The ideal process would enable the use of a 2DLM grown on one catalyst to be integrated on all other types of substrates, thus rendering the development of growth processes for different substrates obsolete. However, it seems that so far, such an ideal transfer process has not been found.

At first sight, transfer seems to be only a minor challenge compared to manufacturing the material in first place. However, despite nearly a decade of research, a general purpose transfer process still does not exist. The main problem is related to why mechanical exfoliation is still the most commonly used method, which is the required cleanliness of the samples. 2DLMs are atomically thin. Being practically only surface and no bulk, they are extremely sensitive to the environment. Any form of contamination, even a few molecules, will deteriorate the material, which itself is of similar scale. To transfer the 2DLM from one surface to another, there must be a method to handle it. If it is brought into contact with any other surface, contamination is introduced to the surface. So the questions is how to move an atomically thin layer from one surface to another one without actually touching it.

Mechanical exfoliation works so well, because the 2DLM only comes into contact with other layers of the same material while in bulk form and with the target substrate. In the case of heterostructures, where the atomically sharp interfaces are crucial for its properties, it is even more important to achieve clean transfer, which is why most heterostructure devices still rely on mechanical exfoliation. With a CVD sample, it is not straightforward to achieve clean transfer. Usually only a monolayer of the respective 2DLM is present. Thus, in order to transfer it, it is inevitable to bring it into contact with some form of stamp or handling tool. Many studies have been published and various methods have been suggested on how to solve the problem of transfer. These will be discussed in detail in Chapter 2. The sheer amount of existing literature and the fact that still more papers are being published clearly demonstrate the urgency and also lack of a solution to this problem.

1.4 Pathway and Outline of Thesis

As the focus of research is shifting towards heterostructures, clean transfer of CVD grown 2DLMs is more important than ever. Using current methods the result of an attempted fabrication would be a stack of 2DLMs with a layer of contaminants trapped at each interface.

At the same time it is of great importance to be able to create heterostructures using scalable methods, as only these structures truly outperform traditional materials. Thus new methods must be found, which are scalable and guarantee atomically clean surfaces. There are two different ways to approach this challenge.

The most straightforward approach is to find a general purpose transfer process that works for all 2DLMs. In this context it is important to investigate the interaction between the 2DLM and the catalyst, as ultimately every transfer seeks to overcome the adhesion between these. Furthermore, an understanding of the sources of contamination and how to minimize these is required. In case not all contamination can be removed, it is necessary to identify ways to clean the 2DLM post transfer. In this context the cost and environmental impact of the process has to be considered, as ultimately the goal is to develop a process that is feasible for industrial scale production. In Chapter 4 a new method of improved transfer will be discussed. The process, which is referred to as Lift-Off Transfer (LOT), makes use of the weak interaction that exists between 2DLMs and certain types of catalysts. Given such a combination, it is possible to intercalate a liquid into the interface and overcome the adhesion without destroying the catalyst and damaging the 2DLM. As the method is based on a detailed understanding of the underlying mechanisms, it is possible to deduce its range of applications and ultimately as well its limits.

The starting point of many existing transfer studies is a given combination of 2DLM and catalyst, most commonly Gr grown on copper (Cu) [51–54]. Their goal is to improve an existing process through parameter optimization or to develop a new process. However, this approach is flawed. The goal of any transfer is to bring a layer of 2DLM onto the target substrate. The catalyst it is grown on is of lesser importance as long as the device integration succeeds. The first step of a comprehensive approach is to identify a substrate that offers both high quality growth of 2DLMs and ease of transfer. Based on these first considerations the choice of 2DLM is to be made. Usually, the outermost layer of a heterostructure is h-BN, as it plays the role of a protection layer. If a layer of h-BN with at least one clean interface was available, it could be the tool to contact and handle other 2DLMs without introducing contamination. Thus, it is necessary to find methods for growth of h-BN on such substrates and to develop an associated clean transfer method. In Chapter 5 a combination of growth and transfer is presented that enables the transfer of h-BN, where one side stays pristine. Furthermore, it is demonstrated how this first layer can be used to handle other 2DLMs and how to ultimately fabricate heterostructures entirely made of CVD grown materials.

The scientific background to the new methods is discussed in detail in Chapter 2. In order to perform this project, it was necessary to develop new equipment for the synthesis

of 2DLMs. This is discussed in Chapter 3, together with all other experimental methods. The work described in this thesis does not represent a final solution to the problem of transfer. However, the new methods introduced here are a crucial step towards enabling large scale fabrication and device integration of 2DLMs. Especially the process to handle CVD materials in a way that allows the fabrication of heterostructures using scalable methods offers a promising starting point to further development.

Chapter 2

Background

This Chapter presents a detailed overview of 2DLMs, CVD. In addition, the interaction of 2DLMs with bulk substrates and existing transfer methods are discussed, with focus is on Gr and h-BN. An understanding of the materials and thestate of the art of research is of crucial importance for further improvement and the potential development of new methods.

2.1 2D Layered Materials

2.1.1 Overview of 2DLMs

Graphene (Gr) was experimentally isolated roughly a decade ago [1]. It has many exceptional properties including high electrical mobility [55, 3, 42, 56], extremely high strength [57] and also high thermal conductivity [58, 59]. This discovery marked only the beginning of research on a whole family of 2DLMs during the last decade. These materials have revealed a multitude of exciting properties making them highly interesting for a large variety of applications. Most 2DLMs consist of a compound of different elements. These can be divided into several large groups of similar materials. One of them is the group of Gr derivatives. These include fluorographene [60], graphane [61] and Gr oxide [62, 63], which are based on the structure of Gr, but contain bonds with other elements. Hexagonal boron nitride (h-BN), though not actually a member of the Gr family, is closely related to Gr. It does not share the chemical composition of Gr, but it is structurally identical. Instead of carbon atoms, N (N) and B (B) atoms are arranged in an alternating pattern. However, in contrast to Gr, h-BN is an insulator and highly chemically inert [64, 65]. The properties of h-BN and Gr are discussed in greater detail in Section 2.1.2 and 2.1.3. Other Gr halides apart

from Fluorographene have been predicted, but have not been experimentally verified to best knowledge [66].

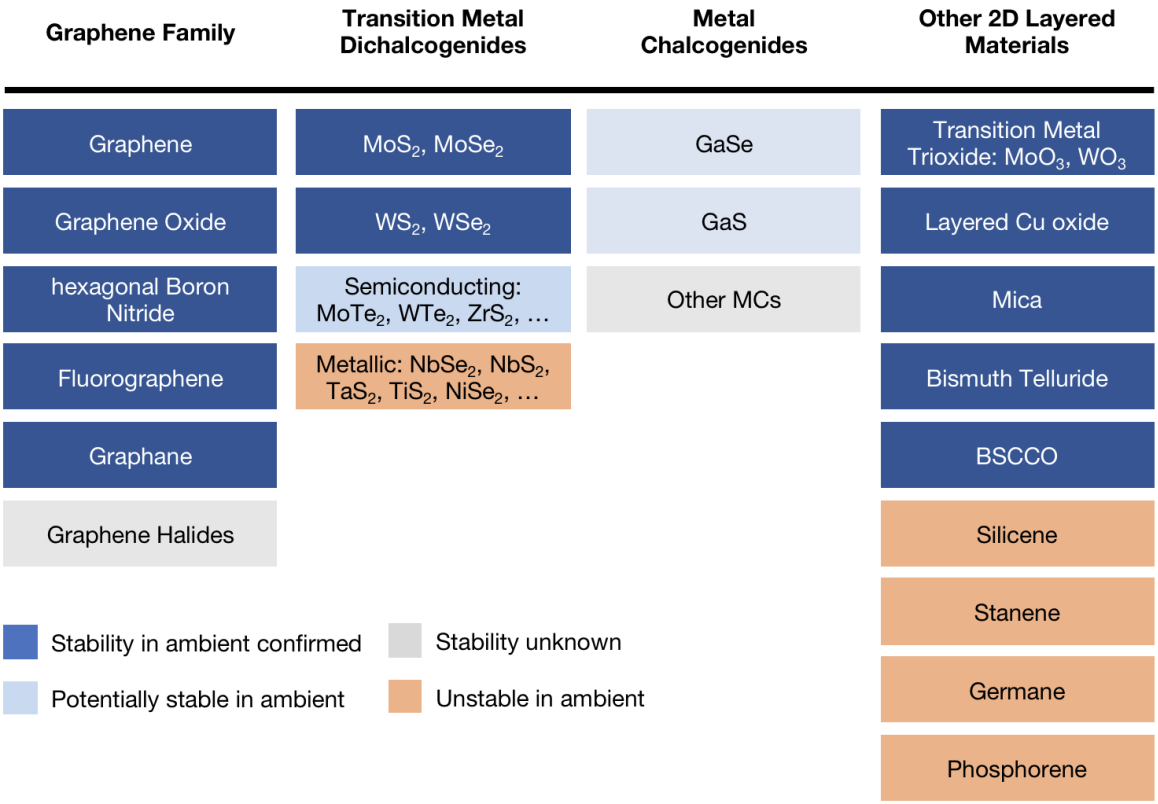

Fig. 2.1 Overview of 2DLM and the stability of monolayers. The Fig. is based on a table given in reference [67]. Additions and modifications were included.

The largest group of 2DLMs are transition metal dichalcogenides (TMD). The chemical structure of these layered materials can be best described as MX2, where M stands for a transition metal and X for a chalcogen. There are about 40 types of TMDs known [68]. The most prominent ones are compounds, where molybdenum or tungsten is bound to sulphur or selenium, such as MoS_2 [69] or WSe_2 [70]. TMDs encompass a large range of electrical properties, ranging from semi conductive to metallic [68, 71]. Chalcogens are also present in another group of 2DLMs, the metal chalcogenides (MCs). These are composed of a group III or group IV metal bound with a chalcogenide. In contrast to TMDs, the structure and dimension depends on the composition of the individual MCs. The most well-known ones are gallium selenide (GaSe) [72], which is a semiconductor, and tin selenide (SnSe) [73], which shows thermoelectric properties.

In addition to the aforementioned materials, there are several other ones that have been less in the focus of research. Certain oxides are known to have a two-dimensional structure

as well, such as molybdenum trioxide (MoO_3) [74]. Most of the other layered materials such as Mica [75], BSCCO [76] or bismuth telluride [77] are more known for their bulk properties and research on atomically thin layers has been relatively limited. Similar to Gr halides, two-dimensional metal halides have been theoretically predicted [78], but not have not been experimentally observed yet..

Besides Gr there are only very few experimentally verified 2DLMs that consist of a single element. One of them is phosphorene, which is the layered building block of black phosphorus [79]. In addition, there are a large number of materials commonly called 2D -Xenes that have been theoretically predicted for an extended period of time, but have only been synthesized recently [80, 81]. These include silicene (a silicon allotrope) [82, 83], germane (a germanium allotrope) [84], stanene (a tin allotrope) [85]. In the case of silicene, a first field effect transistor was reported recently [86]. A common character of these materials is that in contrast to Gr, the atoms are not arranged in a plane.

One reason for the difficulties encountered during the synthesis of the aforementioned materials lies in the stability of 2DLMs. In fact, for a long time atomically thin materials were thought to be generally unstable [87, 88]. Thus, it came as a surprise, when the experimental synthesis of single layer Gr was first confirmed. In general, layered bulk materials with a strong covalent in-plane bond, high thermal stability and mechanical strength are promising candidates for stable few-atomic thin layers. Also high chemical stability is an important issue. If any form of surface chemical reaction is possible in ambient environment, the material will be consumed immediately. Thus, few-atomic layers of every material that forms a self-passivating surface oxide will not be stable in ambient environment.

For any kind of application, it is of great importance to understand the stability of the material or at least to know, how to protect it from the environment. Fig. 2.1 gives an overview of 2DLMs and their respective stability. A material will be considered stable in ambient, if its structure and properties will not degrade strongly within a timescale of a few weeks. It is important to make this point clear, as even Gr, which is usually defined as a stable material, will change its properties if left in ambient over time [89, 90]. Unfortunately for many materials the exact stability is not known. Single layer phosphorene will degrade within hours [91] and silicene within only minutes in ambient environment [85], unless protective measures such as encapsulation are undertaken [92]. Unstable materials will not only make application more challenging, but also complicate any form of experimental research. If a material is prone to oxidation or sensitive to water, many standard experimental methods necessary for transfer and characterisation will become demanding, if not impossible.

2.1.2 Graphene

Gr is the basic building block of graphite, one of the many allotropes of carbon. It is made of carbon atoms bond in a hexagonal pattern as shown in Fig. 2.2 below. Since a long time it was known that graphite consists of atomically thin layers held together by vdW. forces with an interlayer distance of only 0.335 nm. Within a plane, the unit cell comprises two carbon atoms and the lattice vector has a length of 0.246 nm [93]. In fact, first calculations on the electronic band structure of graphite were made assuming non-interacting single atomic layers of carbon [94]. However, for a long time it was thought that single atomic layers are not stable on their own [88].

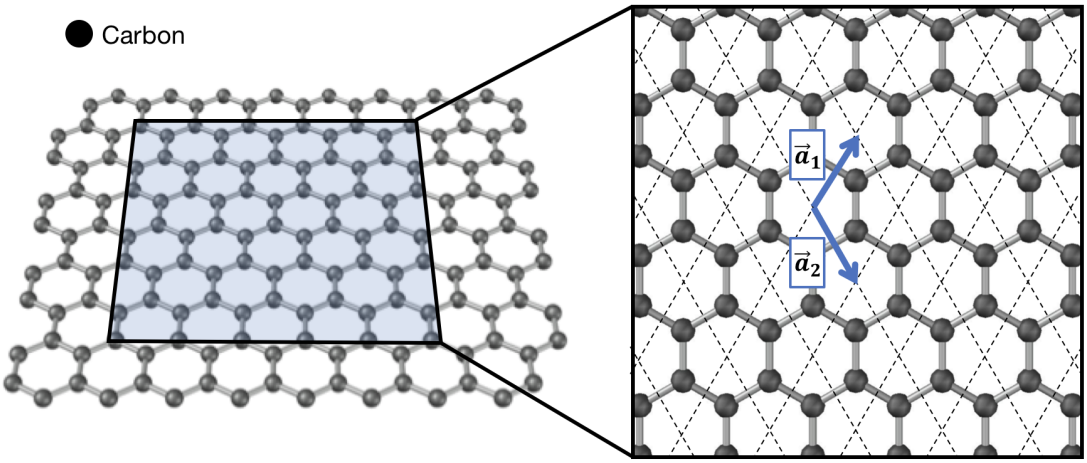

Fig. 2.2 Structure of Gr lattice. Each dot symbolizes a carbon atom. The unit cell and the lattice vectors are highlighted

The orbitals of the carbon atoms in Gr form a sp^2 hybridisation in contrast to diamond with its sp^3 hybridisation. The sigma molecular orbital, which is in-plane, is filled by three valence electrons, which results in a strong covalent bond. The one valence electron left occupies a π molecular orbital, which is perpendicular to the plane. These partially filled perpendicular orbitals overlap and form a π-bond between two adjacent carbon atoms. The delocalization of the π electrons results in the high electrical conductivity in Gr. This bonding configuration also allows for a simple analytical approach to calculate the band structure of Gr [94]. Experiments performed on freestanding Gr have yielded electron mobilities of about 200,000 $cm^2V^{-1}s^{-1}$ at room temperature [55]. For comparison, silicon has an electron mobility of 1450 $cm^2V^{-1}s^{-1}$ [95] and even GaAs, which is one of the preferred materials for High Electron Mobility Transistors (HEMTs), only has an electron mobility of 8500 $cm^2V^{-1}s^{-1}$ [95]. Besides its excellent electrical properties, Gr also has many other

extraordinary characteristics. Despite being only one single layer of atoms, it absorbs about 2.3 % of the incoming visible light regardless of the wavelength [96]. By placing the Gr on a Si wafer with SiO_2 of either 90 nm or 300 nm thickness it is possible to achieve a contrast of up 12%. This is highly relevant for experimental processes, since it means that Gr is easily visible by the naked eye.

In experimental reality the properties of Gr are strongly affected by a number of factors. Being of atomic thickness, it is always under strong influence of its environment. When in contact with a substrate, carriers might be affected by scattering through electrical fields, which are often present on surfaces. For SiO_2, the most commonly used dielectric, these can be caused by dangling bonds and impurities [3] or polar surface phonons [97]. Grain boundaries within a polycrystalline Gr sheet have similar effects [98]. Residues left over from previous processing steps, such as lithography, will result in doping and shift the Fermi energy [99, 100].

2.1.3 Hexagonal Boron Nitride

Besides Gr, the only material that is also made of a single, flat layer of atoms is h-BN. It is isostructural to Gr. Fig. 2.3 shows a model of the structure of h-BN. N and B atoms are arranged in an alternating pattern in a hexagonal lattice. Also, the interlayer distance of 0.333 nm and the in plane lattice constant of 0.25 nm are similar to Gr. Besides of the structural similarities, Gr and h-BN have very little in common. This results from the different electron configurations of its constituent atoms. N has five valence electrons and B three. In both cases sp^2 hybridisation gives rise to the formation of three σ-bonds of each atom with its closes neighbour. After forming the covalent in plane bond, N is left with a lone pair, while none are left for B, as all valence electrons are involved in the in-plane σ-bonds. It is regarded either as a dielectric or a large bandgap semiconductor with a direct bandgap of about 6 eV [101].

The structure of h-BN results in excellent chemical and thermal stability. Even for thin layers it has been shown to be stable to temperatures of 800 °C and more in an ambient environment on non-catalytic substrates [65]. Similar to Gr, it is extremely thermally conductive and mechanically strong [102]. It is even more optically transparent than Gr in the visible range, which makes it nearly invisible regardless of the substrate [103]. The most attractive application of h-BN is its use as a dielectric. It is free of dangling bonds and surface traps, in contrast to many other dielectrics. Furthermore, due to the nature of 2DLMs in general, it is atomically flat. Thus, h-BN is an ideal substrate for Gr and other 2DLMs.

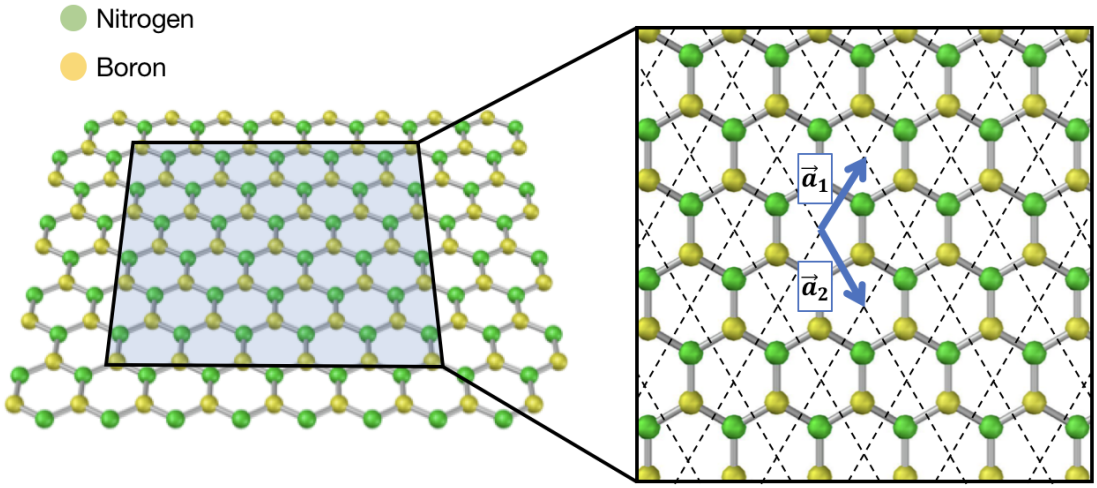

Fig. 2.3 Structure of h-BN lattice. Each dot symbolizes a carbon atom. The unit cell and the lattice vectors are highlighted

Indeed, heterostructure devices based on Gr between few layers of h-BN, as shown in Fig. 2.3, have shown electrical mobilities only matched by suspended Gr devices of up to 350,000 $cm^2V^{-1}s^{-1}$ [3, 42].

2.2 Chemical Vapour Deposition

2.2.1 Introduction to Chemical Vapour Deposition

Chemical vapour deposition (CVD) has been used in the past to produce thin layers of a variety of materials, including silicon, metals and diamond [20]. In general, deposition of a thin layer occurs through a gas phase chemical reaction of the precursor gases, which are provided directly as a gas or are obtained from the solid/liquid phase of the materials. The reaction takes place either in gas phase or on the substrate, where the latter can act as a catalyst. This sets CVD aside from PVD, where no reaction takes place. A large variety of parameters and even types of reactors need to be considered when designing a growth process for a specific material. Thus, it is necessary to take into account the general process and the available methods. These aspects are discussed in the following.

The defining characteristic of CVD is the chemical reaction taking place to break down the precursor. The energy that is needed to initiate the reaction can be provided in multiple ways. The most common type is thermal CVD. The gas phase reaction is promoted by simply

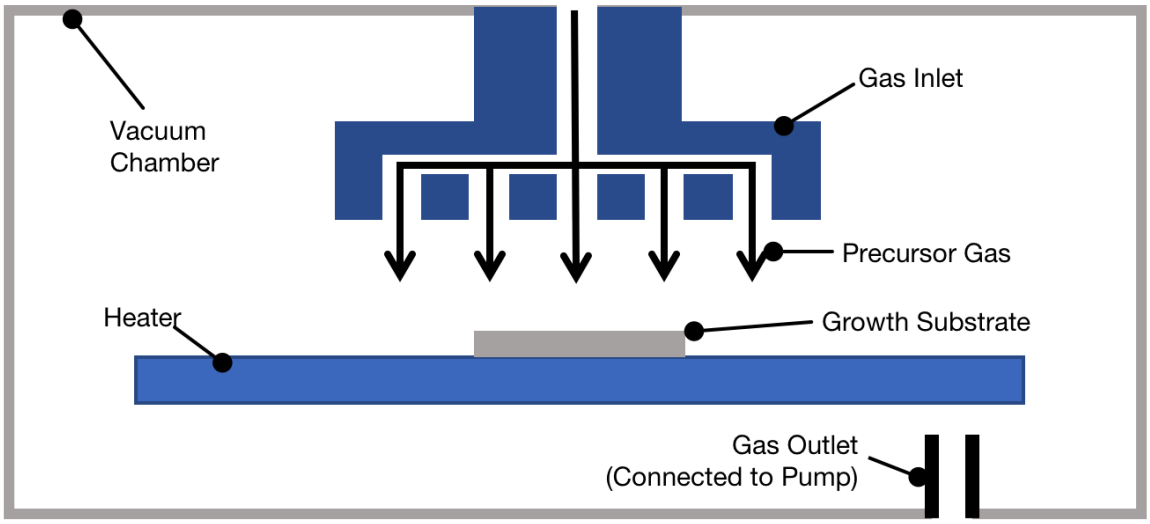

Fig. 2.4 Model of CVD Reactor

heating up the sample under specified environmental conditions. Usually reactions take place at temperatures in the range of 600 °C - 1000 °C. Plasma enhanced CVD (PECVD) makes use of a plasma instead of heat to initiate the reaction. This allows processes at low or even ambient temperatures. In a similar way, photo-assisted CVD utilizes the interaction between light and the precursor molecules to lower the reaction temperatures. There are many more specialized types of CVD. These include metal-organic CVD (MOCVD), which uses metal-organic compounds as precursors, or atomic layer deposition (ALD), where different precursors are sequentially inserted into the reaction chamber to form atomically sharp, thin oxide films.

Thermal CVD is the most popular method for the synthesis of 2DLMs. Understanding the processes and the reactions are of prime importance for the improvement and development of new methods. Usually a chamber is used, which allows precise control over temperature, pressure and gas feed. Fig. 2.4 shows a simplified model of a typical CVD chamber. In such a setup, the target substrate is placed and subjected to precursor gases under controlled conditions. The precursor contains the elemental species that are used for the film growth, but bound within more stable compounds. This prevents the reaction before actually coming into contact with the target substrate. During the deposition, a multitude of different processes take place simultaneously. Fig. 2.5 is a schematic image showing the main processes occurring in thermal CVD [20]. These are given in a rough order of occurrence:

1. The first step in deposition is the evaporation and transport of the precursor through the main gas flow. The exact flow conditions depend on the design specification of

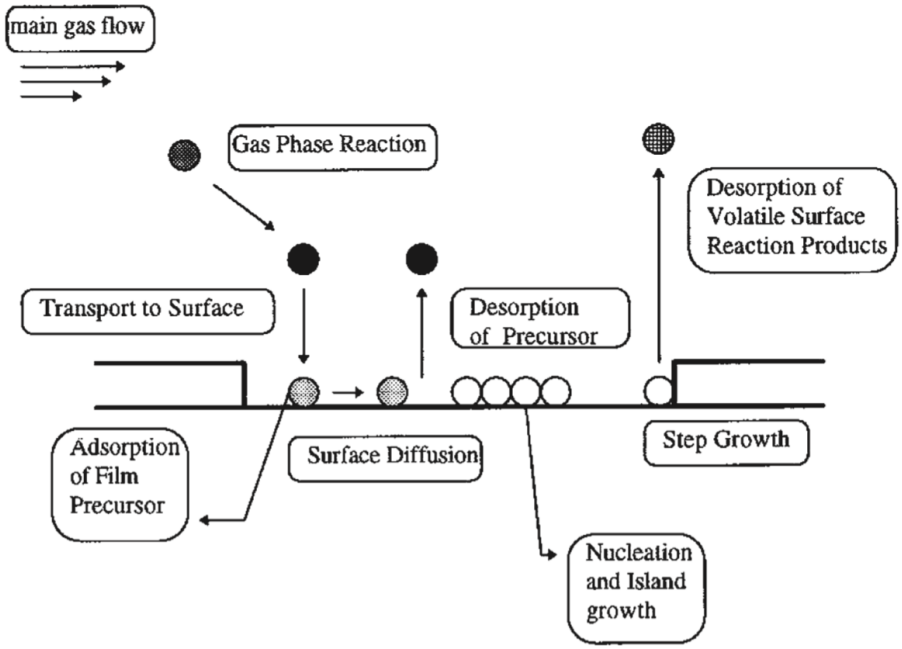

Fig. 2.5 Simplified model of chemical vapour deposition, reproduced from reference [20]

the CVD chamber. Depending on the pressure in the reaction chamber, a boundary layer forms in the vicinity of the substrate. Transport across involves either Fickian diffusion, buoyancy driven diffusion or thermally driven diffusion.

2. The precursor gas can undergo gas phase reactions in the reaction zone to produce reactive intermediates and gaseous by-products. These reactions can sometimes be benefitial for the deposition, but sometimes also hinder the actually desired process by producing a large amount of by-products.

3. After transport of the reactants to the surface, three processes occur:

   (a) Adsorption of film precursor on the substrate surface. This can occur through chemisorption, which is adsorption by forming a chemical bond where the electronic state of the reactants is changed. Another means is physisorption, which is adsorption by physical forces such as van der Waals forces. It is also possible that the precursor is absorbed into the bulk of the substrate.

   (b) Following adsorption, surface diffusion takes place. This can lead to nucleation and island growth or step growth, which is film growth starting at a step in the substrate. Upon extended reaction time this will result in film formation.

(c) Instead of diffusion, desorption of precursor can also occur. The precursors leave the substrate before the reaction can take place.

4. After the reaction has taken place, desorption of volatile reaction products removes the residual products. This is mass transport of remaining fragments of the decomposition away from the reaction zone

The choice of substrate has a great effect on the overall growth process. The simplest case is when the substrate does not impact the chemical reaction taking place for the precursor, which will be referred to as non-catalytic CVD in the following. This is for example given for the deposition of silicon nitride, where the reaction takes place between silane (SiH_3) and ammonia (NH_3). In general non-catalytic CVD requires relatively high temperatures in order to facilitate the gas phase reaction and the grown material is of poor quality. Furthermore, the thickness of the layer that is deposited depends mainly on the duration of the process [43–45, 20].

In catalytic CVD, the substrate is involved in the actual reaction. It acts as the catalyst, lowering the energetic barrier for the reaction and thus reducing the temperature requirement. This is especially important for carbon-based materials, as dissociation of most precursors without catalysis occur at more than 1500 °C [104]. Another feature of this process is that by careful tuning of the growth parameters, self-limiting growth down to a monolayer can be achieved [17]. The ideal choice of catalyst and how it affects the initial growth and later processing will be discussed in Section 2.2.4 and 2.3.

2.2.2 General CVD of 2D Layered Materials

Catalytic CVD has been the most widely used approach for 2DLMs. Fig. 2.6 is a series of images depicting an exemplary CVD process. The main steps during a deposition are nucleation, expansion of islands and eventual merging to a continuous film.

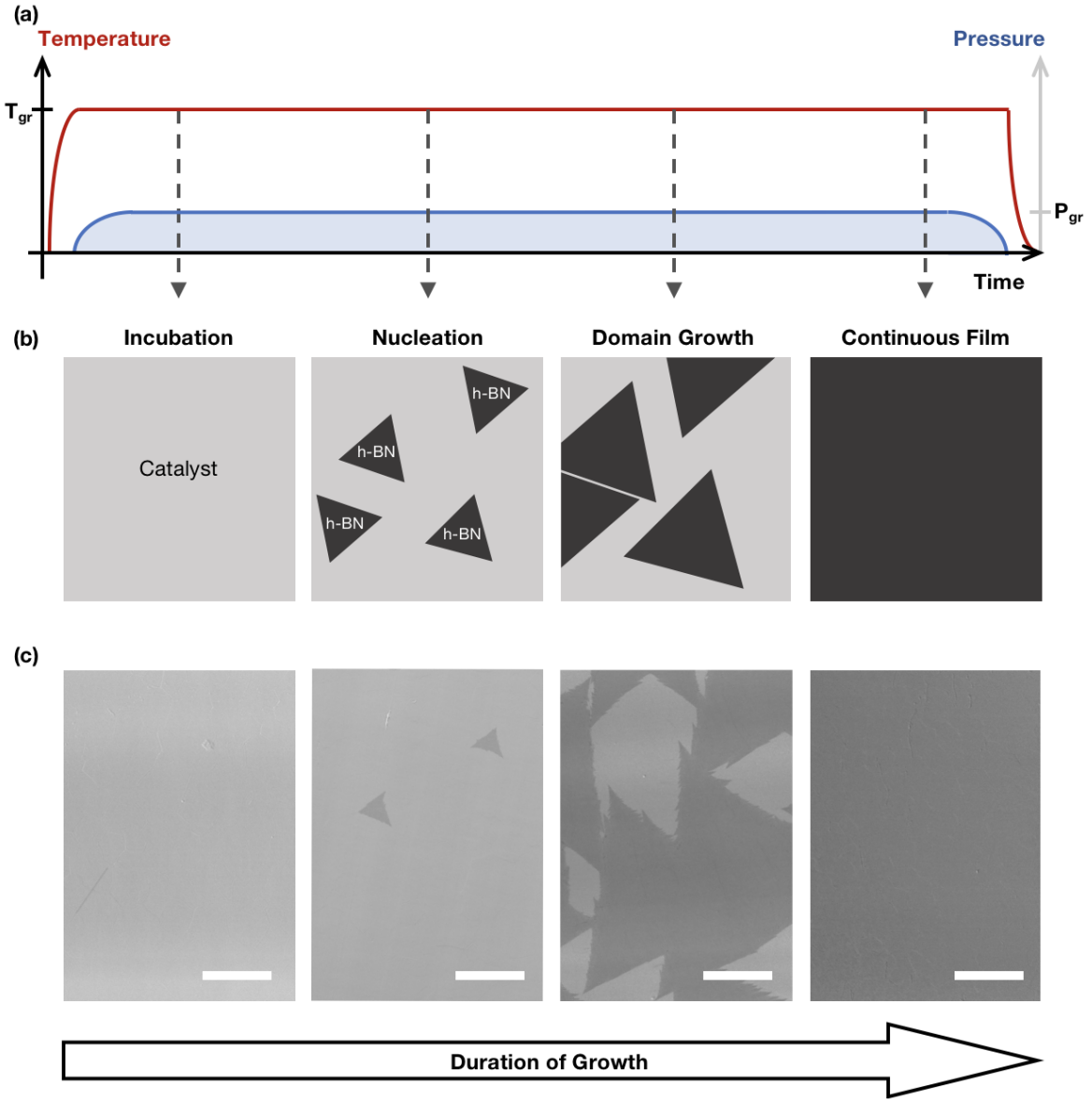

Fig. 2.6 2DLM growth process **(a)** Process diagram of standard CVD process. The sample is heated up to growth temperature T_{gr} and the precursor is injected into the chamber at pressure P_{gr}. After sufficient deposition time, the chamber is evacuated and cooled down. **(b)** Schematic images and **(c)** scanning electron microscopy (SEM) images of a sample during an exemplary h-BN deposition process. Additional details about growth of h-BN are discussed in Chapter 5.

The defining step in film formation is nucleation, i.e. the formation of individual small crystal domains. It is achieved by overcoming the solubility limit of the growth substrate. The processes leading to super-saturation and thus growth can be understood based on a model, which has been developed for Gr growth [17, 48, 105]. When the precursor first comes into contact with the catalyst, it dissociates and is absorbed into the bulk. Actual

growth can then occur through two different pathways as shown in Fig. 2.7(a). The first is precipitation on cooling. Super-saturation results from a decrease of the precursor solubility of the catalyst, which is achieved during cooling at the end of the process. The species already absorbed into the bulk will precipitate from the surface, where the film is formed. The other pathway is isothermal growth. Upon increased exposure to the precursor and absorption, super-saturation sets in. The solubility limit is reached and the precursor is not taken into the bulk any further. Thus nuclei are formed on the surface. Continuing the gas exposure will prompt these nuclei to grow in size. Eventually they will coalesce and form a continuous layer. It should be noted that the growth process is highly dynamic, depending on the concentration gradient in the catalyst.

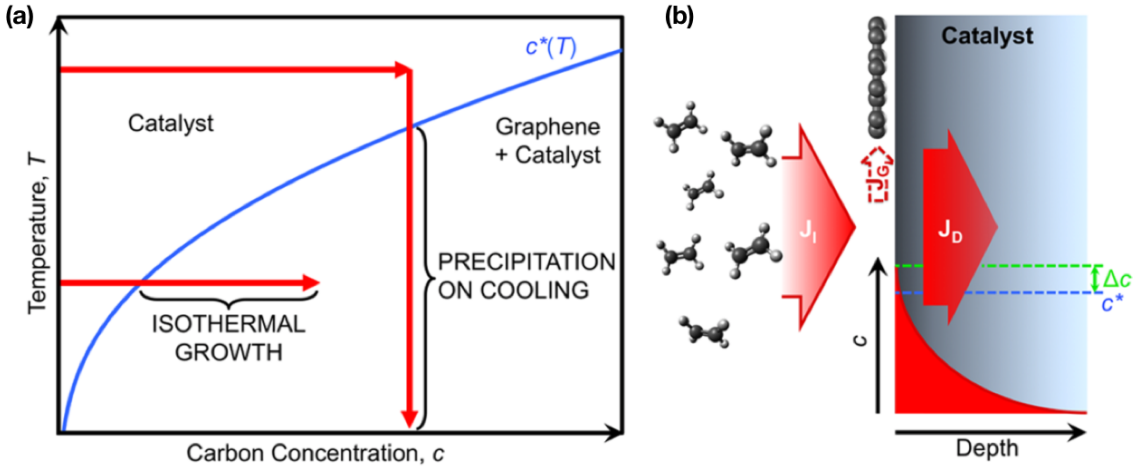

Fig. 2.7 Mechanism of CVD illustrated for the example of Gr, reproduced from reference [17]. **(a)** Schematic carbon-catalyst phase diagram. The blue line illustrates the solubility, i.e. the maximum concentration of carbon, within the catalyst. The red arrows indicate the different pathways for achieving growth of Gr. **(b)** Model showing the balance between precursor flux to the substrate (J_I) and bulk diffusion (J_D). The difference of both (J_G) contributes to the growth of Gr layer at the interface.

The choice of catalyst, which will be discussed in detail in Section 2.2.4 determines to some extent the growth mechanism and also the film properties. In the case of Gr, catalysts have been used that enable both modes of growth. Isothermal growth has been achieved with Cu due to its extremely low carbon solubility [25]. Precipitation on cooling has been demonstrated among others for nickel (Ni) [24]. It should be noted however that the mode of growth does not only depend on the chosen catalyst, but also on the kinetics of the process itself, as shown in detail in Fig. 2.7(b). Through careful process control it has also been possible to grow monolayer Gr on Ni [106].

By varying the process parameters it is possible to achieve such as multilayer formation. This effect is observed frequently for 2DLMs growth [107–109]. One reason for the formation of multilayers lies in the mixture of precipitation and isothermal growth. After isothermal formation of the first layer, it is possible for additional layers to grow through precipitation depending on the amount of dissolved precursor species and the cooling rate. This effect is more pronounced for catalysts with a high solubility [105]. It is also possible to achieve multilayer growth purely through isothermal growth. Similar to the primary layer, secondary ones also rely on the catalytic activity of the catalyst. In fact these grow underneath the first ones, by diffusion into the interface through defects [110].

During growth, the catalyst needs to be free from contaminants or surface oxides. Thus the substrate is usually annealed in a reducing gas such as hydrogen (H_2) or ammonia (NH_3) prior to the growth process. Other forms of pretreatments have been used, primarily with the target to reduce preferential nucleation sites [111]. The precursor is chosen based on many different aspects. It is obvious that it has to contain the elemental species necessary for the final film. Furthermore, it must be possible to obtain its gaseous form with reasonable efforts. Often precursors are used, which are already in gas-phase under ambient conditions.

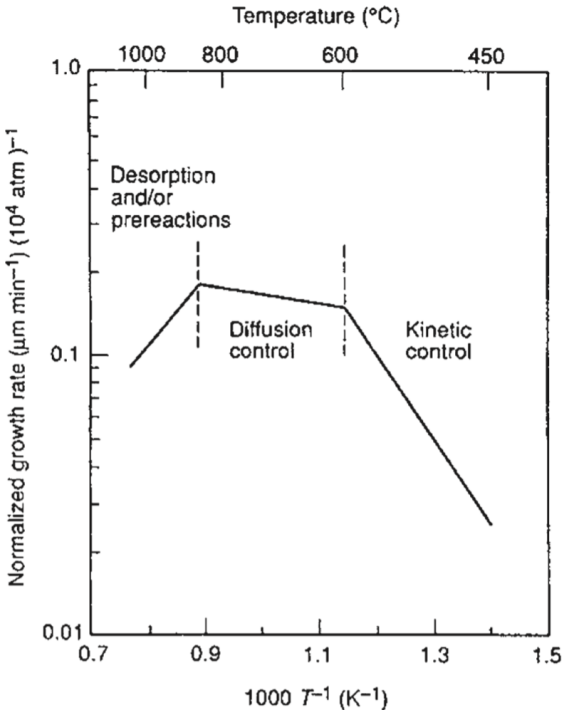

Fig. 2.8 Temperature dependence of growth rate for the example of metal organic CVD (MOCVD) of gallium arsenide (GaAs). Adapted from reference [20]

However, solids or liquids are also applicable, as long as they are sufficiently volatile. At the same time the precursor must be stable enough, so that decomposition does not already occur during evaporation or before the desired reaction conditions are reached. The complete reaction that actually leads to the dissociation can be very complicated, involving many different intermediate steps depending on the applied precursor [112].

The primary growth parameters are substrate temperature, operating pressure, composition and chemistry of the gas-phase. Depending on the operation point, many different growth domains can be achieved, which are shown schematically in Fig. 2.8. While it is difficult to predict the effect of an exact parameter value, there are general trends. At low temperatures the growth rate is con-

trolled by the chemical reaction rate, thus it is called the **kinetic control** growth domain. This means that as soon as a reactant is available, it is consumed, since the following steps in the process are much faster. In this domain the growth rate is given by [20]:

$$k_r \propto e^{-\frac{E_A}{RT}} \tag{2.1}$$

Here k_r is the reaction rate, E_A the activation energy per mole of the reaction, R the universal gas constant and T the temperature of the reaction. The reaction can be primarily tuned by changing the precursor, which affects E_a. Changing the temperature also affects the reaction rate. Small changes will simply result in an acceleration of the process, a large one alters the growth regime.

At high temperatures the reaction enters the **mass transport control** domain. Growth is not limited by the speed of the chemical reaction, but only by the mass transport of the reacting species in the boundary layer to the growth surface. It should be noted however, that whether or not a boundary layer is present again depends on the pressure regime. The precursor flux can be modelled as [20, 113]:

$$J_D = \frac{1}{RT}\frac{D}{\delta}(P_0 - P_b) \tag{2.2}$$

The flux is denoted by J_D. D is the diffusion coefficient, δ the thickness of the boundary layer, and P_b and P_0 the pressures at the surface and sufficiently far away. The individual terms D and δ themselves depend on the temperature, and the characteristics of the boundary layer such as P_b depend on the geometry and flow characteristics of the gases [114]. This stage has the highest growth speeds. When increasing the temperature even further the growth rate starts to decrease, due to an increased rate of desorption of film precursors from surface and/or depletion of reagents due to gas-phase side reactions. This is called the **desorption control** domain.

In a similar way, a general trend can also be observed for changes in pressure [20]. At high pressure, which is roughly atmospheric pressure until 1.3 kPa (13 mbar), gas phase reactions are important and a significant boundary layer is present. Kinetics and mass transport both play an important role. When pressure is lowered to less than roughly 130 Pa growth is controlled by surface reactions only. In high vacuum, which is usually regarded as less than 0.01 Pa (1 x 10^{-4} mbar), mass transport can be neglected. There is also very little gas-phase interaction. Layer growth is controlled by the choice of precursor, substrate temperature and by desorption of precursor fragments only. Growth at low pressure is a somewhat simpler

process, since the effect of gas phase reaction and mass transfer are negligible. At the same time it sets much higher requirements on the equipment.

Due to the interplay of multiple processes, it is difficult to predict the exact effect of variations of certain parameters on overall growth. However, certain rules of thumb exists. Growth at high temperature combined with extremely low pressure results in a low nucleation density. Since each nucleus represents a crystal domain in the final polycrystalline film, such conditions result in the largest crystal domains. Increasing the pressure will increase the nucleation density and also lead to faster growth. In general it is desirable for 2DLMs to achieve the largest crystal domains possible, since it reduces the number of grain boundary related defects. Thus a combination of high temperature and low pressure is the most favourable starting point for most growth studies.

2.2.3 The Parameter Space of CVD of h-BN

Before the actual interest in 2DLMs was sparked, there had already been many reports on the deposition of thin films of h-BN [115]. The fundamental difference in growth between h-BN and Gr is that h-BN requires two different elemental species. In most of these early studies combination of precursors were used, such as BCl_3/NH_3, B_2H_6/NH_3, BF_3/NH_3 [116]. This complicates the process, as the ideal ratio of both gases has to be carefully tuned. A much simpler approach is to make use of a precursor with the required stoichiometric ratio. In some studies, a solid precursor such as borazane, also known as ammonia borane, has been applied [117, 118]. It is evaporated in a pre-chamber and then directed into the reaction chamber by a flow of an inert gas. However, especially in conjunction with a hot-wall CVD reactor, it can exhibit a complicated decomposition profile with many intermediate species [112]. While it may seem an attractive precursor choice on first sight, as it is safe and inexpensive, the difficulty in maintaining a stable precursor atmosphere makes it challenging to achieve sufficient control over the deposition condition. A more easily applied precursor is borazine ($B_3N_3H_6$), which is a compound of B, N and hydrogen. At room temperature it is liquid with a high vapour pressure of 340 mbar, which facilitates the direct use of the vapour without heating [119]. In addition it automatically provides the gaseous species with the required stoichiometric ratio.

The existing literature highlights the large range of accessible pressure that can be utilized for h-BN synthesis. The arguably first study on monolayer growth of h-BN was published nearly four decades after the initial report [120] (Earlier studies have only investigated the absorption of borazine on transition metals, without realizing the possibility of it actually

being a 2DLM [121]). It was performed in an ultra-high vacuum environment with a pressure of less than $2x10^{-10}$ mbar. Other methods have emerged that have much lower requirements regarding pressure, some of them even demonstrating h-BN growth under atmospheric pressure [26]. The largest crystal domain sizes of a few hundred micrometres have been achieved using low growth pressures [47].

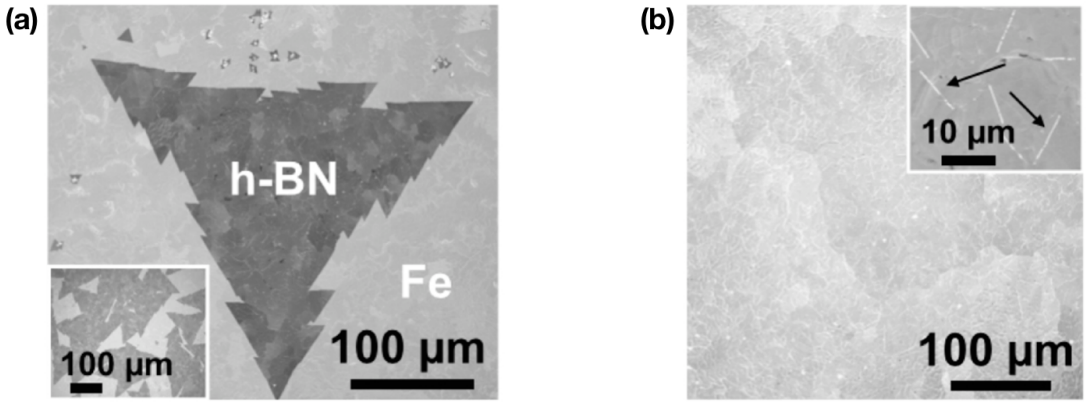

Fig. 2.9 SEM image of CVD h-BN grown on iron (Fe). **(a)** Individual h-BN island before merging. **(b)** Continuous film of h-BN. The inset (arrows) highlight domain boundaries in the film originating from imperfect merging of the h-BN nucleii. Adapted from reference [47].

Regardless of the pressure, all growth processes require high temperature of at least 800 °C, which depends strongly on the used catalyst. The growth process leads to nuclei with a distinctive shape, which can be highly useful when tuning the growth process. Fig. 2.9 shows an image of h-BN nuclei. Unlike Gr, h-BN does not form hexagonal islands during growth, but characteristic triangles. The reason is most likely that the edge energy is different depending on whether it is N or B terminated, with the first being the more stable configuration [122].

2.2.4 Choice of Catalyst for CVD of h-BN

Many different growth catalysts have been used for the synthesis of h-BN. These are primarily transition metals including copper (Cu) [120, 123, 124], nickel (Ni) [120, 26, 125], platinum (Pt) [126–131], palladium (Pd) [132], iron (Fe) [133, 134, 47], cobalt (Co) [135], ruthenium (Ru) [127, 136], rubidium (Rb) [127], rhenium (Rh)[137] and silver (Ag) [138]. The choice of catalyst is of critical importance for the CVD process. Not only does it determine the parameter space of the deposition, but also the characteristics of the as-grown h-BN.

Furthermore, it has also a significant impact on materials processing, which will be discussed in greater detail in Section 2.3.

Transition metals are commonly used in heterogeneous catalysis [139]. In general, the primary role of a catalyst is to facilitate a chemical reaction, which in the case of CVD is the precursor dissociation. However in the context of h-BN and 2DLM growth, the catalyst has additional functions. An already present layer of 2DLM will impede the adsorption of additional precursor molecules on the catalyst surface. Thereby, growth primarily takes place in regions, which are not yet covered. This feedback loop is critical to achieve monolayer deposition. It should be noted that this layer control is subject to many additional factors, such as growth mode (i.e. isothermal or precipitation), growth parameters (i.e. temperature and precursor pressure) and layer quality. For example diffusion through defects or the edge of an existing layer will result in the nucleation of an additional layer [110]. In addition, the catalyst promotes the formation of the crystal lattice so that defects are significantly reduced compared to non-catalytic growth at the same temperature [45, 43, 44].

The efficacy of a catalyst is best described with the Sabatier Principle [139, 140]. In simple words, it states that the ideal conditions for a catalytic reaction is given, if the adsorption strength of the reagent is neither too high, nor too low. Fig. 2.10 shows a schematically graph, which is often referred to as volcano plot due to its characteristic shape, highlighting the relationship between adsorption strength and reaction rate. In the context of 2DLM growth, it means that the catalyst should enable the stable adsorption of the precursor to facilitate the dissociation reaction, but at the same time the strength of adsorption has to be sufficiently weak for the reaction products to desorb. The adsorption strength, and thus the catalytic activity, is primarily determined by the electronic structure of the surface of the metal [141]. The critical parameter in this context is the state of the d-orbital of the transition metal. In general, the higher the average energy of the electrons in the d-orbital (i.e. how it is filled with electrons) is relative to the Fermi energy, the stronger the interaction with the adsorbing reagent becomes. Fig. 2.10(b) highlights this relationship for the adsorption of Oxygen. In a rather simplified manner, one could state that when moving from the left to the right in the periodic table of elements, the metals interact less strongly with adsorbates.

The catalytic activity is only one of many considerations that have to be taken into account when making a choice for the ideal catalyst. Depending on the desired characteristics of the film, for example the thickness, it is important to also consider the solubility of the precursor and potential formation of compounds. In Fig. 2.11 the situation is shown for CVD of Gr. Similar to the strength of adsorption, the carbide heat of formation and the carbon solubility depend on the state of the d-orbital. It should be noted that this is not a coincidence,

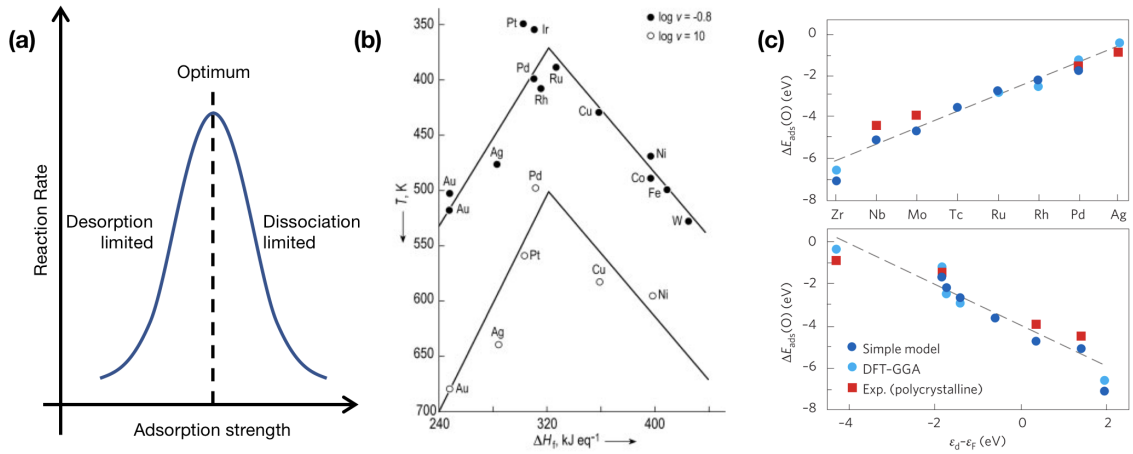

Fig. 2.10 a) Illustration of Sabatier Principle (b) Example of volcano plot for decomposition of formic acid. Adapted from reference [140] (c) Oxygen adsorption energy for various transition metal. Adapted from reference [141]

but especially the likelihood of carbide formation is intimately linked to the strength of adsorption [142]. The situation is significantly more complex in the case of h-BN CVD, as two different species have to be considered. This means that instead of one compound, there is the potential formation of borides and nitrides. Furthermore, in terms of solubility both species have to be taken into account.

The content discussed in this Chapter should be considered as general guideline, rather than a precise guide to the choice of catalyst. In addition to the aspects that have been mentioned, a variety of catalyst characteristics influence the growth process. This includes for example the texture of the catalyst surface [143, 144] or its roughness [111]. Furthermore, in contrast to carbon, for which a large body of literature exists due to its prominent role in the steel industry and wider metallurgy, much less literature is available for B and N, especially since both need to be considered in unison together with a potential catalyst. However, a general understanding of catalysts and their role in CVD is crucial when designing new growth processes. Perhaps even more important than the role of the catalyst during growth, especially when focussing on end-applications, is its interaction with the as-grown 2DLM. This interaction is much more decisive for the choice catalyst than its catalytic activity, which will be discussed in detail in the following Section.

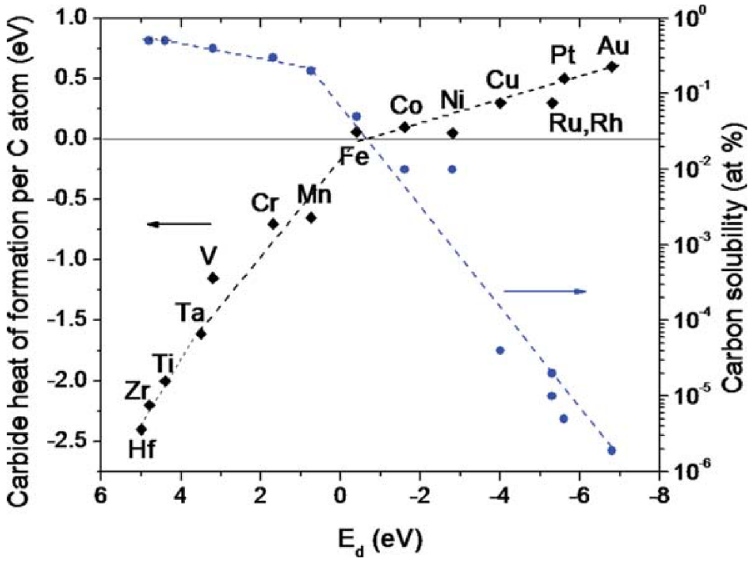

Fig. 2.11 Carbide heat of formation and carbon solubility plotted against the d-orbital energy of various metals relative to the Fermi energy of the carbide. Adapted from reference [142]

2.3 Substrate - 2DLM Interaction

2DLMs have been suggested as the ultimate passivation layer, due to their atomic thickness and the reported impermeability to gases [145, 146]. However, when immersing CVD Gr on Cu in water, it becomes obvious that in this case the 2DLM is not only unsuited for passivation, but that the corrosion of the underlying metal is even enhanced. [147, 148]. In contrast, CVD Gr on Ni [49, 149] or h-BN on Ni [150] have been proven to be excellent passivation layers. While it is true that CVD grown 2DLMs are prone to defects and imperfections, it raises the questions why the level of passivation varies so dramatically for different substrates.

In order for oxidation to take place, atmospheric species need to be able to access the substrate surface. It has been observed that when CVD Gr on Cu is stored under ambient conditions, atmospheric species diffuse into the interface within a few hours [151, 152]. Thus, oxygen is able to access the entire surface. In addition, water, either as vapour or liquid, can act as an electrolyte, which results in galvanic corrosion [147, 148]. This effect is extremely detrimental to surface passivation, but can be of use for transferring the 2DLM as will be discussed in Chapter 4. However, in the case of Ni, 2DLM can passivate the surface and maintain its pristine state even over months [153, 150]. This is not due to a significantly higher quality of the 2DLM grown on Ni, but it is caused by their strong interaction.

In general one can distinguish between two different types of substrates regarding interaction: weakly and strongly interacting ones. The difference for both types is highlighted in the schematic given in Fig. 2.12. In case of weakly interacting substrates, such as Cu or Pt, 2DLMs decouple upon air exposure, allowing atmospheric species to penetrate the interface after diffusion through defects or edges of the 2DLM layer. While the latter also occurs for strongly interacting substrates such as Ni, Co and Fe, the 2DLM remains strongly bound to the substrate, thus preventing diffusion into the interface. For metals with self-passivating oxides such as Ni or Co, the oxidation is limited to the exposed regions. However, in the case of Fe, which does not form a passivating oxide, oxidation will occur, albeit at a slower rate than for weakly interacting metals. Indeed it has experimentally observed that for Ni [49] or Co [150] 2DLM can passivate the surface for extended periods, while for Fe [154] the oxidation is slowed down significantly. For Pt [153] and Cu [147, 148] intercalation occurs rapidly, which leads to associated oxidation in the latter case.

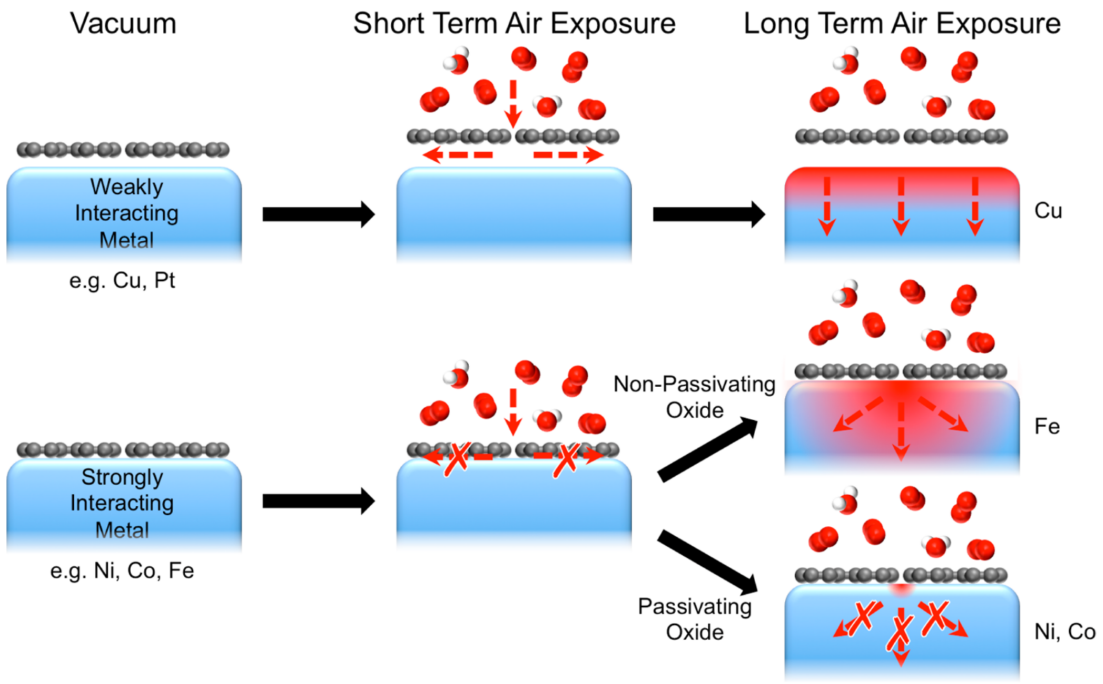

Fig. 2.12 Illustration of the passivation effect of Gr on different metals.

The reason for this widely differing interaction lies in the varying degree to which 2DLM are bound to the substrate. The strength of interaction depends on the level of hybridization between the π-orbital of the 2DLM and the d-orbital of the metal. Similar to the adsorption of precursor, which dictates the activity of the catalyst, as described in Section 2.2.4, the level of filling of the d-orbital determines the strength of interaction [153]. The difference in interaction strength is of significant importance for the application. If the goal is to use

the 2DLM as a passivation layer, deposition on a strongly interacting metal is required. However, if transfer is needed, growth ideally is performed using a weakly interacting substrate. Transfer will be discussed in detail in the following Section.

2.4 Transfer of CVD 2DLMs

2.4.1 Introduction to Transfer

Based on intuition, the most critical problem for the application of 2DLMs should be its synthesis. However, as long as CVD growth of high quality 2DLMs relies on the presence of a catalyst, which is not the device substrate, transfer will remain a necessary step for any kind of processing. While growth of high quality 2DLMs on par with material obtained from bulk exfoliation has been demonstrated [42], no standard method has been found to detach 2DLMs from their growth substrate after CVD growth and to place it onto a desired substrate.

The common goal of every transfer process is to overcome the adhesion of the 2DLM to the catalyst. Doing so requires the 2DLM to be free of the support that the catalyst provides. Despite the often cited strength [57] it is necessary to attach a support layer to the 2DLM during transfer, which is often a polymer layer. This is not required for some transfer processes, which however often lack scalability or can only be applied in very specific cases [155–158]. There are broadly speaking two groups of transfer processes. The most straightforward process, the basis of a so-called dry transfer, is to attach an adhesive layer to the 2DLM and to delaminate it by applying mechanical force [159, 160]. Direct delamination by force is also the mechanism behind electrochemical delamination although the exact source of the applied force is still the topic of debate.[52, 161, 162]. In the case of what has been referred to as clean-lifting transfer, this force is generated by electrostatic charges [163]. The other group of methods can be broadly referred to as ones that rely on the removal of the catalyst. A widely used transfer method, usually called wet transfer, makes use of the selective etching of the entire catalyst [25, 164, 24]. Other methods have emerged, for example oxidative decoupling transfer, where only the interface of the catalyst is removed [53].

Each of the methods has its advantages and disadvantages. So far no one-size fits all solution has been found. When comparing the quality of the transfer many metrics have to be considered, such as the damage, wrinkling and contamination of the layer, but also the ease of transfer. Some transfer method perform better regarding one aspect, but worse regarding

another one. Thus, currently for most application the transfer method is chosen based on the most critical requirement. However, for nearly all methods there is one common issue. During nearly all transfer processes, the 2DLMs are brought into contact with a solution on one side and a support layer on the other side. The only exception is dry transfer, where it is possible to reduce the contamination of the side facing the catalyst to a minimum, at least avoiding contamination introduced by any solution used in the other methods. The consequence is that in the case of non-ideal cleaning processes, residues will remain on the 2DLM. In the following, we will discuss the main transfer methods, especially focussing on the cleanliness and limitations.

2.4.2 Transfer Based on Catalyst Removal

Fig. 2.13(a) outlines the process flow of wet transfer. The result is shown in Fig. 2.13(b). At the beginning of the process, the 2DLM is coated with a support layer. Then the metal film is etched. If the stiffness of the support layer is sufficiently low, conformal contact will be established once the film is placed onto the target substrate. The last process step is the removal of the support layer.

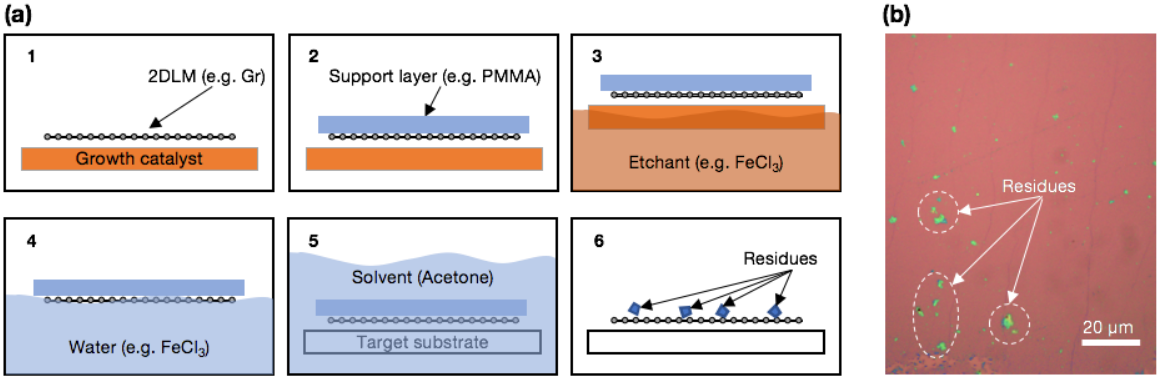

Fig. 2.13 **(a)** Illustration of the wet transfer process. **(b)** Optical image of Gr layer transferred onto 300 nm SiO_2 on Si wafer. Contrast, brightness and colour are adjusted for improved visibility. Residues from transfer are highlighted.

Since chemical inertness is one of the prerequisites for the stability of a 2DLM, this approach appears to be promising at first sight. The main problem is the large amount of residues left. Usually the material of choice for the support layer is a polymer, such as polymethyl methacrylate (PMMA), due to its stability against most acids and the ease of processing. But its removal during the final step of transfer leads to a large number of residue particles. Various other polymers including polycarbonate (PC), polyphthalamide (PPA) [51],

polystyrene (PS) [165] and polylactic acid (PLA) [166] combined with many different kinds of solvents, such as acetone, chloroform and toluene have been used. While some differences could be found, none of the methods resulted in contamination free transfer. Many studies have also sought to remove residues, instead of avoiding them. The standard method to remove organic residues in semiconductor processing is oxygen plasma. However, this is not feasible given the thinness of 2DLMs (plasma etching also involves sputtering) and the fact that for example Gr consists of carbon as well. Hydrogen annealing at temperatures between 300 °C and 400 °C [167] has been shown to reduce the amount of residues without significantly damaging the Gr layer.

It is still unclear, why polymers leave such residues after transfer. One suggestion is that since CVD Gr is permeable, the acid that is used to remove the catalyst will contact the polymer, leading to interlinking of the polymer chains and making parts highly stable to solvents [166]. In addition to polymer residues, metallic contamination and unintentional doping have been reported [168]. To avoid at least the issue of polymer contamination, other support materials have been used, such as gold [169] or pentacene [170]. Although these methods show improvements in material quality, they are still not completely free of residues, slow and involve expensive support materials that are lost at the end of the process. Another approach applies a material with low adhesion energy as support layer. The idea is that after catalyst etching and transfer to the target substrate, the 2DLM adheres more strongly to the latter, so that the support can be simply removed by delamination. Since there is no support layer that needs to be dissolved or etched, this method should result in a cleaner surface. Indeed, studies have shown that cleaner samples can be obtained [165]. The most important aspect of this method is to create a highly conformal contact between the material and the stamp and then between the stamp and the target substrate. This is not always possible, since growth substrates have a surface roughness, defined as the arithmetical mean deviation R_a of tens of nano-meters, while for a standard silicon wafer this value is less than one nanometer. Layers often contain holes or are even only partially transferred.

Wet transfer and stamp transfer rely on the detachment of the 2DLM and catalyst by etching. This means that except for costly methods of extraction, it can be considered lost. Furthermore, these transfer methods are not applicable for all kinds of substrates. Certain substrates are very hard to etch. This is the case for chemically inert growth materials, such as Pt, thin metal films on oxides, semiconductors and thick foils.

2.4.3 Electrochemical Delamination

Electrochemical transfer, also referred to as bubbling transfer, is a widely used process of direct delamination, especially since it enables the delamination of 2DLMs that cannot be easily etched. Fig. 2.14 presents the process that is involved. As a first step the 2DLM is again coated with a support layer. This stack is then used as the cathode in an electrochemical cell. An inert material such as platinum is used as the cathode and an alkaline solutions such as sodium hydroxide (NaOH) is used as the electrolyte. When a voltage is applied, the support layer detaches together with the 2DLM.

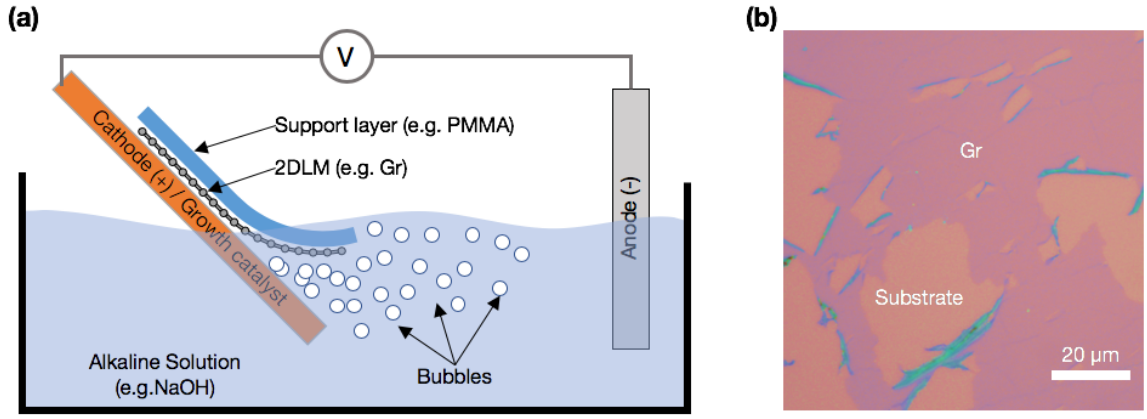

Fig. 2.14 **(a)** Illustration of the bubbling transfer process. **(b)** Optical image of Gr layer transferred onto 300 nm SiO_2 on Si wafer. Contrast, brightness and colour are adjusted for improved visibility. Gr layer is highly fractured.

This transfer has been applied for Gr and h-BN grown on different metal catalysts including ones that cannot be easily etched such as Pt [161, 171, 47]. Besides of being versatile, the catalyst is not destroyed in the process. However, the layer is often damaged. One reason that has been proposed is that mechanical forces cause holes in the film. Methods have been devised to improve the quality of the transferred layer, such as the use of a stabilizing frame [172] or very low cell voltage [173].

The process that actually leads to the delamination of the film is still unclear. The chemical reaction taking place in the electrochemical cell is given below.

$$\text{Reaction at Cathode (-):} \qquad 2H_2O + 2e^- \rightarrow H_2(g) + OH \tag{2.3}$$

$$\text{Reaction at Anode (+):} \qquad 4OH^- \rightarrow 2H_2O + O_2 + 4e^- \tag{2.4}$$

Here H denotes hydrogen, O oxygen and e^- an electron. One mechanism that has been proposed is that the hydrogen is produced at the interface of the 2DLM and the catalyst. It

then forms expanding bubbles, which exert a mechanical force [161]. However, this theory fails to explain how the solution penetrates the interface in first place and why the 2DLM would still adhere to the catalyst given the presence of a layer of liquid in between. Another explanation that has been suggested is that the support layer, 2DLM and the catalyst are effectively two capacitors in series. The delamination process is suggested to be the electric break-down of one of the capacitors [174]. In general, bubbling transfer generates cleaner samples compared to wet transfer, as shown in Fig. 2.15. Nonetheless, there are still a lot of particles present at the surface and in addition the layer is often damaged by mechanical fracture.

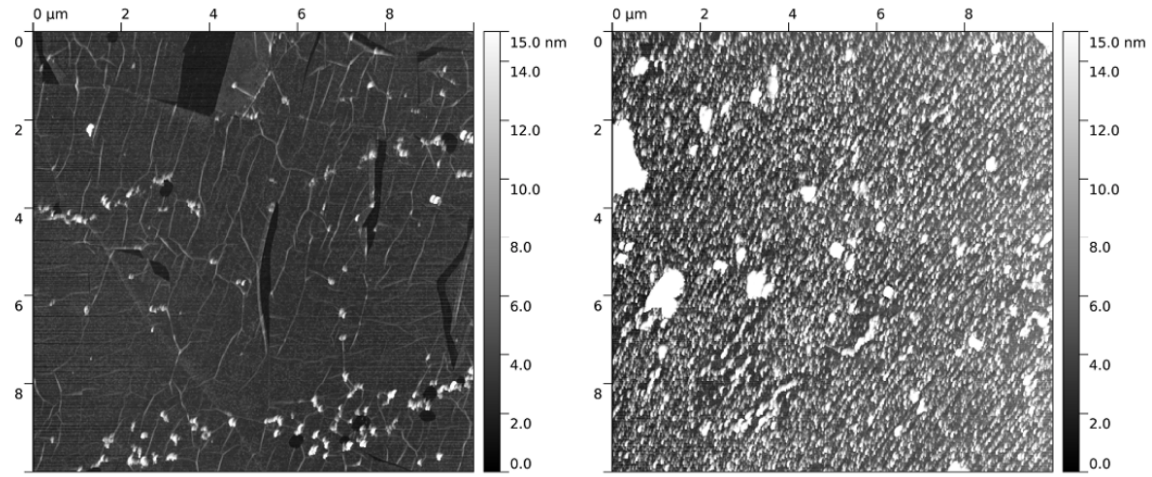

Fig. 2.15 Atomic force microscopy (AFM) images of Gr transferred by **(a)** bubbling and **(b)** wet transfer. Samples imaged directly after transfer without additional post-processing or cleaning. Experiments performed by the author.

2.4.4 Mechanical Delamination

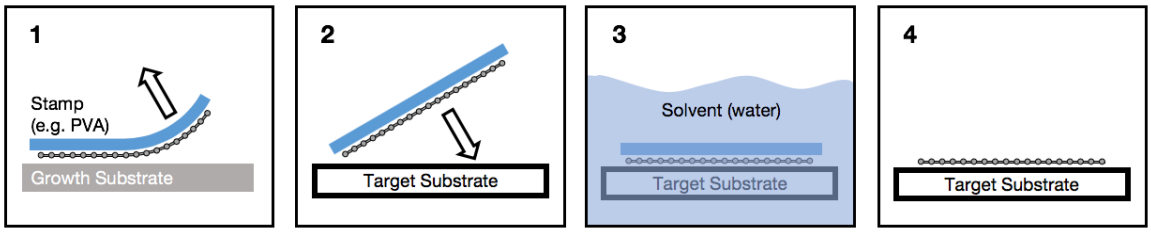

Fig. 2.16 Schematic depiction of delamination transfer process.

The most straightforward method of transfer is to directly delaminate the as-grown 2DLM from the catalyst. This method is not only the simplest method of transfer, but also

the cleanest, as the 2DLM surface in contact with the catalyst is not contaminated by any solution. It has been applied for a variety of different combinations of 2DLM and catalyst. The transfer process is schematically shown in Fig. 2.16. The first step consists of bringing a stamp into contact with the 2DLM. In case the adhesion of the 2DLM to the stamp is stronger than to the catalyst, it detaches upon mechanial delamination of the stamp. In a final step, the stack consisting of stamp and 2DLM is deposited on the target substrate and the stamp is removed.

How strongly the 2DLM adheres to both the catalyst and the stamp is critical for the success of the transfer. Most existing studies have focused on the transfer of Gr from Cu [175, 159, 176, 54]. This might be due to the popularity of Cu as catalyst for Gr CVD, but as discussed in Section 2.3 it is also coincidentally a well-suited system for delamination transfer due to the weak interaction. When oxidizing the Cu at the interface with Gr by immersion in water for extended periods, it is possible to further weaken the interaction and to achieve improved transfer with less fracture of the Gr layer, which is shown in Fig. 2.17 below.

A variety of materials have been applied for the stamp. This includes metals such as Au [175] and Ni [176], which again highlights the substrate dependent adhesion of 2DLMs. Other approaches make use of polymers [54]. Both these strategies require in the final step the removal of the stamp through dissolution using acids or solvents. The most promising method has been to directly use h-BN as the stamp to delaminate as-grown Gr from the Cu catalyst [42]. The process is shown Fig. 2.18. During the entire transfer, the Gr is only in contact with the growth catalyst and the h-BN stamp. Therefore it remains pristine and can be directly integrated into a heterostructure. Indeed the high electron mobility and low level of doping prove the cleanliness of the transfer method. The critical issue is that this method is not entirely scalable, as it relies on h-BN obtained from bulk-exfoliation. However, it is an important improvement as it demonstrates the feasibility of applying CVD grown materials for high performance devices using delamination transfer. In Chapter 5 it will be discussed how using this research as the starting point, a method for entirely scalable heterostructure fabrication is developed.

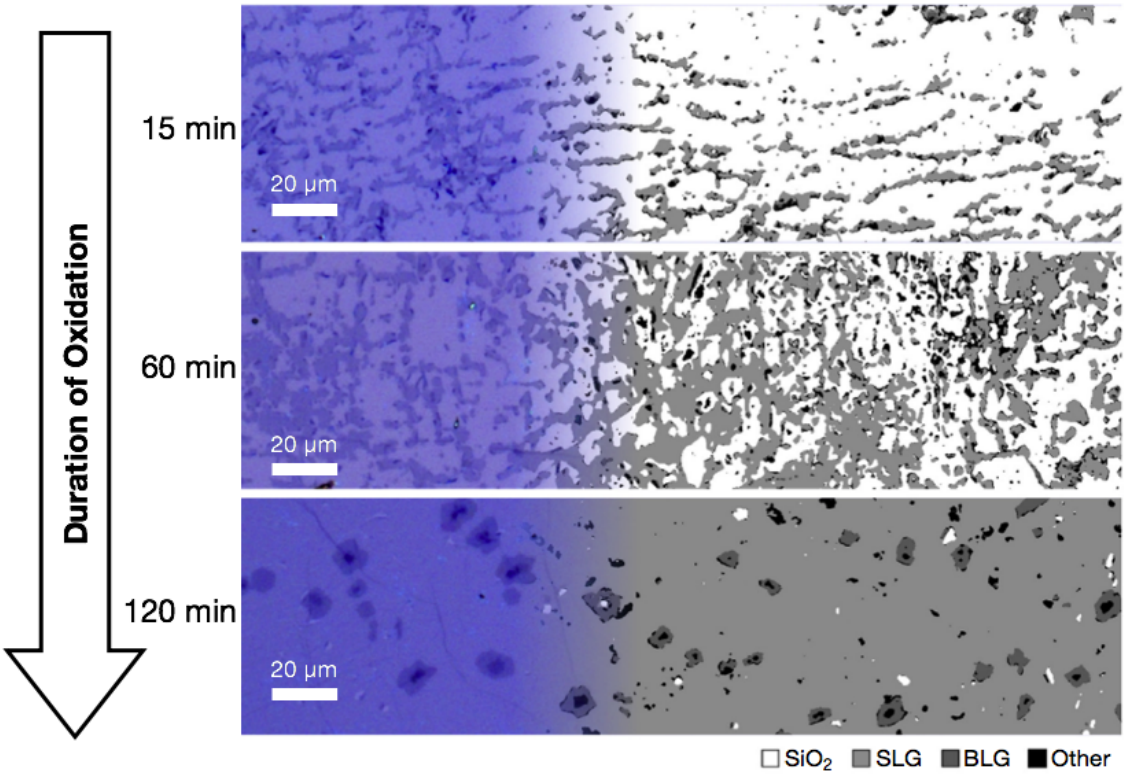

Fig. 2.17 Effect of Cu Oxidation for delamination transfer. Gr grown by CVD on Cu is immersed in water for an different time durations. Transfer is performed thereafter using the procedure outlined in Fig. 2.16. The substrate is 90 nm SiO_2 on Si. Left is the image taken using optical microscopy, right is the image processed to highlight coverage. Details on this method are given in Chapter 4. Extended oxidation significantly improves the Gr coverage.

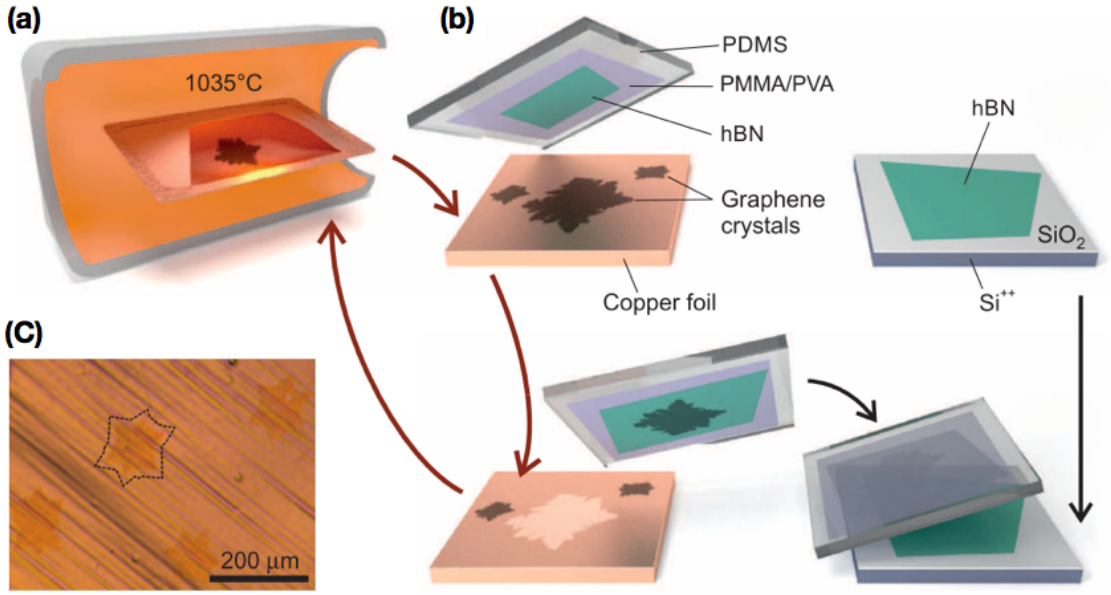

Fig. 2.18 Process for delamination transfer of CVD grown Gr using h-BN Stamp. Adapted from reference [42]. **(a)** Illustration of Gr growth in hot-wall CVD reactor. **(b)** Schematic of transfer process. A flake of h-BN obtained through mechanical exfoliation of a bulk crystal is used as the stamp to directly contact and delaminate the CVD Gr. **(c)** Optical microscopy image of as grown Gr nucleus on Cu.

z

Chapter 3

General Experimental Methods

Many different experimental methods were utilized for the work described in Chapter 4 and 5. This includes the design and installation of a new laser based CVD system and various characterization techniques. These will be discussed in detail in this Chapter with the focus on their relevance for Gr and h-BN.

3.1 Laser CVD Reactor Design

In experimental reality a major challenge for CVD is the precise control of the environment in the deposition chamber. Especially in hot-wall reactors, i.e. a reactor where the entire containment is heated, the precursor is directly injected into a heated environment. Thus, the precursor can go through a series of gas phase reactions before reaching the catalyst, thereby creating an ill-defined and uncontrolled gas environment. This is especially a problem for ammonia borane, a popular precursor for the deposition of h-BN, which has a complicated decomposition profile, with many intermediate species [112]. This problem is alleviated for cold-wall reactors, which are reactors where the thermal energy is provided to the sample through local heating using for example a resistive heater plate, but only if the the heated area is sufficiently small.

Regardless of the type of reactor, cross-contamination is a major challenge for growth, especially when a reactor is used for deposition of different materials. During deposition, the precursor will not only react with the catalyst, but is likely to react with any sufficiently heated part of the reactor. In addition, if the growth is carried out at high temperature, the sample itself might evaporate and re-deposit on other locations in the chamber. If the reactor

is used in the following without going through very time-consuming cleaning processes, the increase in temperature can result in the desorption of the aforementioned species, which adversely affects the new deposition. Due to all these reasons, usually CVD reactors are used for only one type of deposition. However, this is a major issue for example in case of CVD of heterostructures through sequential exposure with different precursors. Another drawback of dedicating a reactor to one type of deposition is the obvious impediment it poses for early stage research, where it is often necessary to trial a large set of precursors and catalyst, without having access to a large number of reactors.

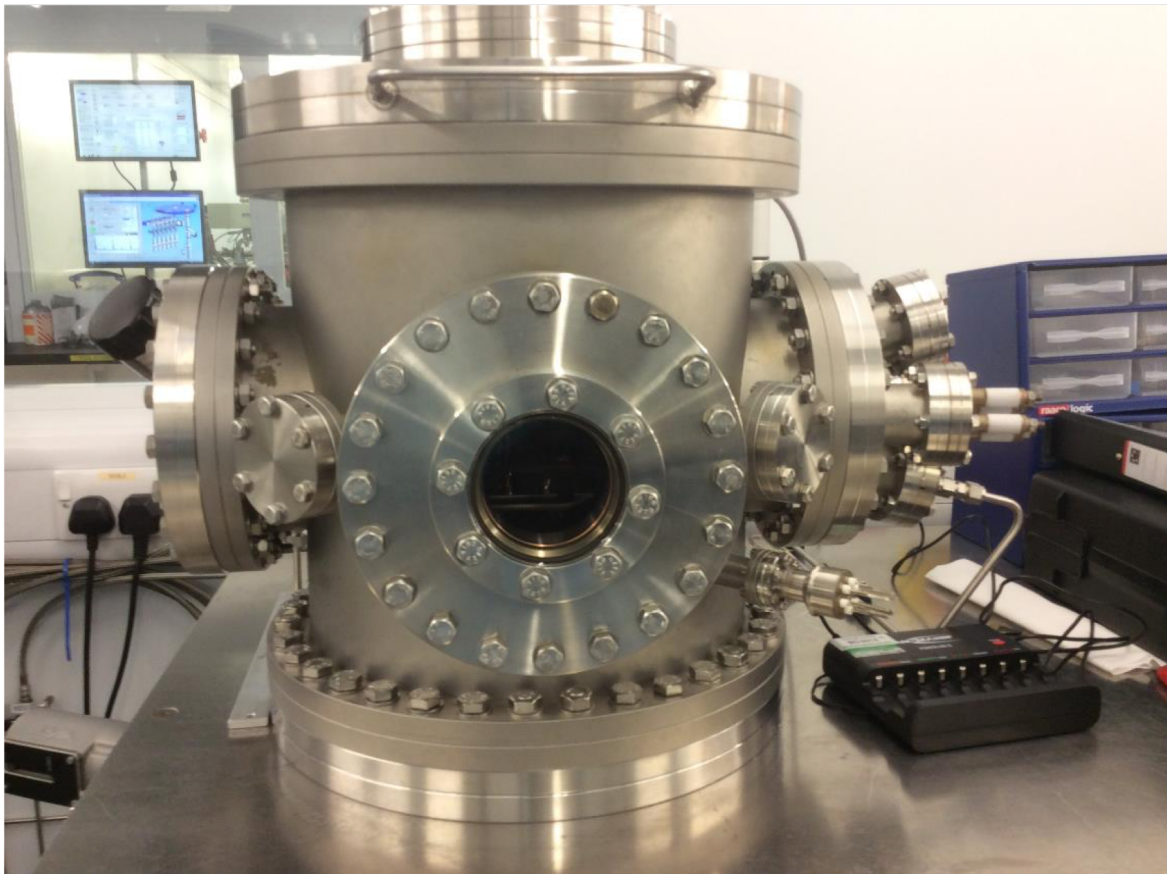

Fig. 3.1 Photo of custom built laser CVD reactor.

One approach to counteract these adverse effects is to limit the heating to the smallest possible area, thereby ideally only heating the catalyst. This excludes the use of a hot-wall reactor. But also when applying a cold-wall reactor, standard resistive heaters should be avoided, as in such a setup the heater still always remains the hottest part of the entire chamber. The only solution is to supply the thermal energy remotely. One possible approach is inductive heating, which is an established method that is often used in metallurgy. However,

the rate of heating is dependent on the conductivity of the substrate, which in case of thin metal films on insulator can result in extremely inhomogeneous temperature profiles and associated problems such as thermal stress. Another source of inspiration is physical vapour deposition (PVD), where a large array of methods are employed to heat the target material [177]. This includes heating using electron beams, plasma and lasers. Since a plasma transfers mainly kinetic energy, it is always associated with sputtering of the surface, which has to be avoided when dealing with the deposition of single atomic layers. Electron beam is only applicable in high vacuum and the required equipment can be extremely complex. Thus remote heating using a laser is the most suitable choice.

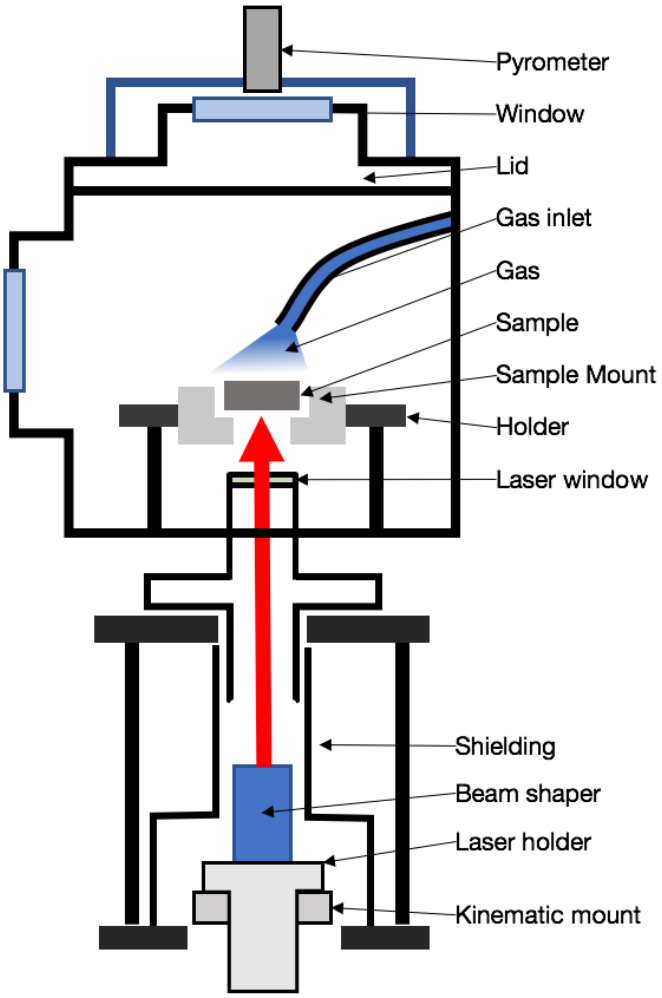

Fig. 3.2 Schematic of custom-built laser CVD reactor. All parts not labelled are part of the enclosure or connections. The pumping system, gas manifold and pressure gauge were omitted from the sketch for better visibility.

Fig. 3.1 shows the laser CVD reactor that was designed and built as part of the PhD project. A schematic of the components is given in Fig. 3.2. The key component of the reactor is a 808 nm continuous wave (cw) diode laser (LIMO GmBH LIMO-ILS60-F100-5319), which is mounted below the reaction chamber. It is coupled into the chamber through an anti-reflection coated vacuum window. By placing the laser outside of the chamber, sensitive optical components are protected from any potential source of contamination. To enable homogeneous heating, the laser is equipped with a beam shaper. At the focal point at a distance of 600 mm from the outlet, the power is evenly distributed over a square area of 5 mm x 5 mm instead of the usual Gaussian intensity profile. The laser is directly aimed at the sample or the susceptor it is placed on. Taking into account potential changes to sample

placement or misalignment of the setup, the beam shaper is inserted into the kinematic mount that allows rotation in two axes.

Deposition is performed in the low pressure regime of roughly 0.1 mbar or less. Despite higher requirements on the vacuum chamber and the associated pumping equipment, low pressure CVD has many advantages as discussed in detail in Section 2.2.2. The custom-built chamber is made of stainless steel and all parts are connected using copper gaskets. Only the lid is sealed using a standard rubber o-ring. The chamber is pumped using a two stage setup. A roughing pump is used between atmospheric pressure and 0.1 mbar, followed by an air-cooled turbo pump (Oerlikon Leybold Vacuum). The base pressure of the system is below mbox1 x 10^{-6} mbar and can be reached after about 20 min of pumping depending on the state of the reactor (e.g. how long it has been vented). The pressure in the vacuum chamber is monitored using a full range gauge (Pfeiffer Vacuum PKR 251). It consists of a combination of a Pirani and a cold cathode system, which are chosen automatically for low and high vacuum respectively. The pressure is measured in the entire range from 1000 mbar to 5 x 10^{-9} mbar.

A variety of gases are connected to the chamber in different ways. Standard processing gases, including ammonia (NH_3), nitrogen (N_2), hydrogen (H_2), argon (Ar), methane (CH_4), ethylene (C_2H_4) and acetylene (C_2H_2) are connected though mass flow controllers (MKS Instruments) to the chamber. These are run by a central control unit. Since borazine is a liquid with only limited vapour pressure, it is challenging to regulate the flow using a mass flow controller. Instead the borazine bottle (Fluorochem Ltd.) is connected to a leak valve (Agilent Variable leak valve) and the flow is regulated manually. All gases are injected into the chamber using standard vacuum tubing. Due to the small size of the samples, which is dictated by the laser spot size, a shower head is not necessary for uniform gas flow.

The way that the sample is mounted depends on the type of catalyst. In some experiments, e.g. when the catalyst is very thin or larger than the laser spot, it is necessary to place the sample onto of a susceptor, which absorbs the laser radiation and spreads the heat evenly. A variety of susceptors have been used including silicon carbide (SiC), tantalum (Ta) and tungsten (W), which are all materials chosen for their high melting temperature and chemical inertness. For example for h-BN growth on Pt, foils made of W with a thickness of 25 µm (Alfa Aesar Ltd.) were used. The exact experimental procedure is given in Chapter 5. The sample together with the susceptor is mounted in a Macor holder which differs between experiments. In general it has roughly a dimension of 50 mm x 50 mm with a cutout of 10 mm x 10 mm in the center for passing the laser beam. The sample temperature is monitored using a pyrometer (Optiris CT Laser 2MH), which is located outside of the reaction chamber,

with a spot size of 3 mm. The transmission coefficient is calibrated using the melting point of Cu, i.e. by melting Cu foil and tracking the displayed temperature, while emissivity is taken from literature. The entire setup can be controlled using a PC with a custom written Labview programme. The only exception is the injection and flow of borazine, which has to be manually operated using the leak valve.

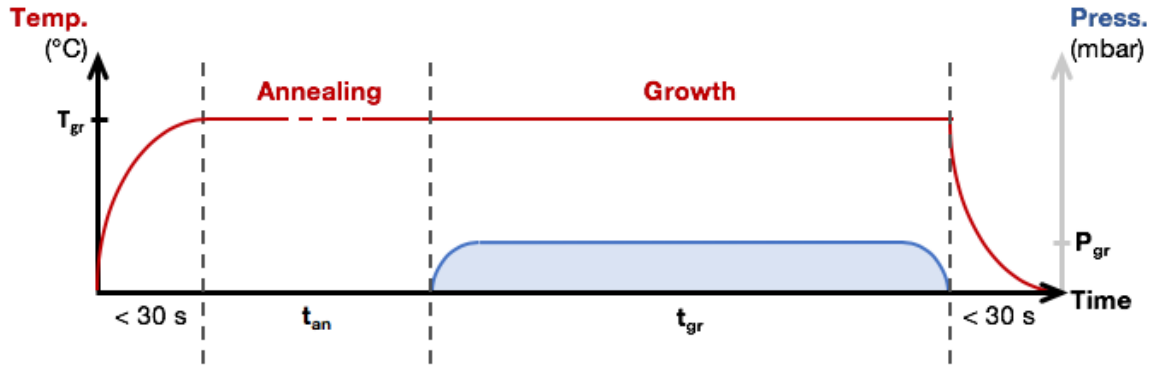

Fig. 3.3 Process schematic of exemplary growth run.

As an example, Fig. 3.3 shows the flow diagram of a simple h-BN deposition process. The exact procedure varies depending on the type of material that is grown and its desired characteristics, e.g. the nucleation density. A general description of the operation of the reactor is given below:

1. After closing the gate valve connecting the turbo pump, the chamber is vented with N.
2. The sample is fixed to the Macor mount designed for the targeted process. It is loaded into the reaction chamber.
3. First, the chamber is pumped down to below 0.1 mbar using the roughing pump. The valve connecting the roughing pump is then closed and gate valve is opened. Typically processes are started after reaching a base pressure of 5 x 10^{-6} mbar or less.
4. If necessary, an annealing gas is injected into the chamber. Often hydrogen is used to reduce any potential surface oxides. In the process shown in Fig. 3.3 none is required.
5. The laser heater is turned on and the power is ramped up until the required temperature (T_{gr} is reached). This can be done within a few seconds or depending on the exact required rate. Since even small variations in samples size or laser alignment can influence the heating, the pyrometer reading is used for temperature monitoring instead of simply focusing on the power output.

6. After a brief annealing period (t_{an}), the precursor is injected. In the example in Fig. 3.3 borazine is injected into the chamber using the leak valve. The partial pressure (P_{gr}), is monitored using the pressure gauge and the valve is adjusted accordingly.

7. At the end of the specified growth time (t_{gr}), the leak valve is closed and the laser is ramped down or turned off immediately. In the latter case, the sample temperature will sink below the lower detection limit (~500°C in case of Pt) of the pyrometer within about 5 - 10 s.

8. The chamber can be vented a few minutes after growth and another process can be performed.

3.2 Characterization Techniques

3.2.1 Scanning Electron Microscopy (SEM)

Scanning electron microscopy (SEM) is a popular method for observing features below the resolution limit of visible light. The measurement of surfaces is conducted by scanning an electron beam over the sample. Fig. 3.4(a) shows a model of a SEM. The principles of SEM are discussed in detail in standard literature [178]. The beam is produced by an electron gun and focused by a variety of lenses. The sample usually sits on a movable stage. The spatial resolution of the SEM is determined by the probe size, which is the size of the beam at the sample surface.

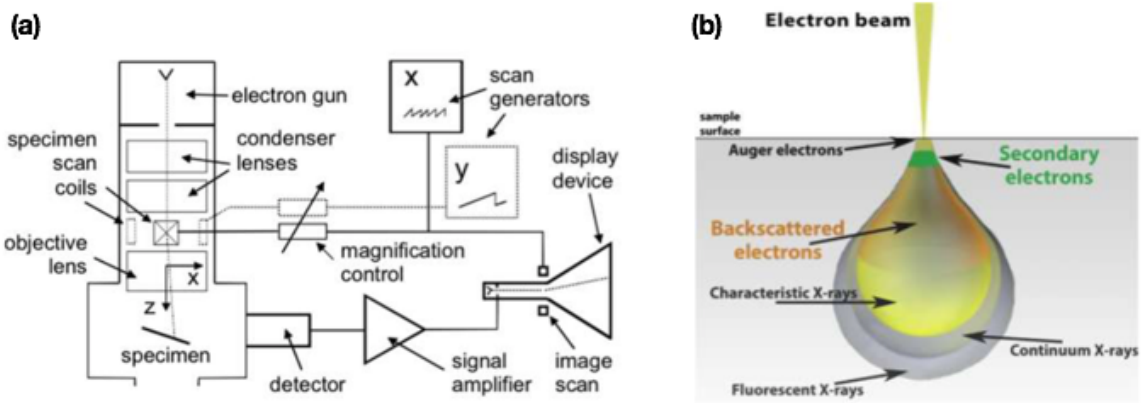

Fig. 3.4 **(a)** Simplified model of a SEM. **(b)** Interaction volume of the primary beam. Auger electrons and x-rays are not measured by standard SEM detectors. Image obtained from reference [178]

In order to discuss the mechanism of detection, it is necessary to know the interaction between the beam and the specimen. The actual interaction takes place within a finite volume, called the interaction volume. Fig. 3.4(b) shows a sketch of the interaction volume. Its size depends on the beam energy. An increase in the beam energy or a decrease of the atomic number will result in a deeper interaction volume. Two types of electrons are emitted that are relevant for SEM: backscattered and secondary electrons. These originate from different depth within the sample and thus carry different information.

Secondary electrons (SE) are the result of inelastic scattering of the beam. The electrons have only low energies of about 0-50 eV and are emitted from a maximum depth of only few nanometres (~0.5 nm for metal, ~10 nm for insulators). This allows a high resolution of the surface. Backscattered electrons (BSE) result from elastic scattering of the beam. These electrons emerge from much greater depth and thus carry less information about the immediate surface. Image contrast arises from different surface geometry and material properties.

For the analysis of 2DLMs usually SE is the preferred mode of detection, due to its surface sensitivity and speed. The contrast depends on many factors such as the type of substrate, the surface texture and the state of the interface with the 2DLM. The contrast is also known to change in case of intercalation, which has been observed for CVD grown 2DLM on weakly interacting substrates [153, 179, 152, 180]. The mechanism of contrast itself has been the topic of discussion and is still unclear. One suggestion is that for example Gr lowers the work function of the underlying substrate, thereby changing the SE yield [181]. However, this theory fails to explain why Gr typically appears to be darker than the bare underlying catalyst, despite the supposedly lower SE yield. Others have suggested that Gr itself has a very low SE yield [182]. Experiments have studied the SE yield of Gr on catalyst in detail and have found that not the total yield is changed, but the spectra of the emitted electrons [183]. It is likely however, that the actual mechanism is more complicated and is a combination of the explanations that have been put forward.

In general, as shown in Fig. 3.5, monolayers of h-BN and Gr have a darker contrast than the bare metal substrate. However, this can change over time and is subject to potential intercalation and oxidation of the underlying metal, which is discussed in greater detail in Chapter 5. Thicker layers of Gr will appear darker in SEM, while multilayer h-BN appear bright. The later agrees well with standard literature, as multilayer h-BN will behave like an insulator and thus create significant charging effects when observed in SEM.

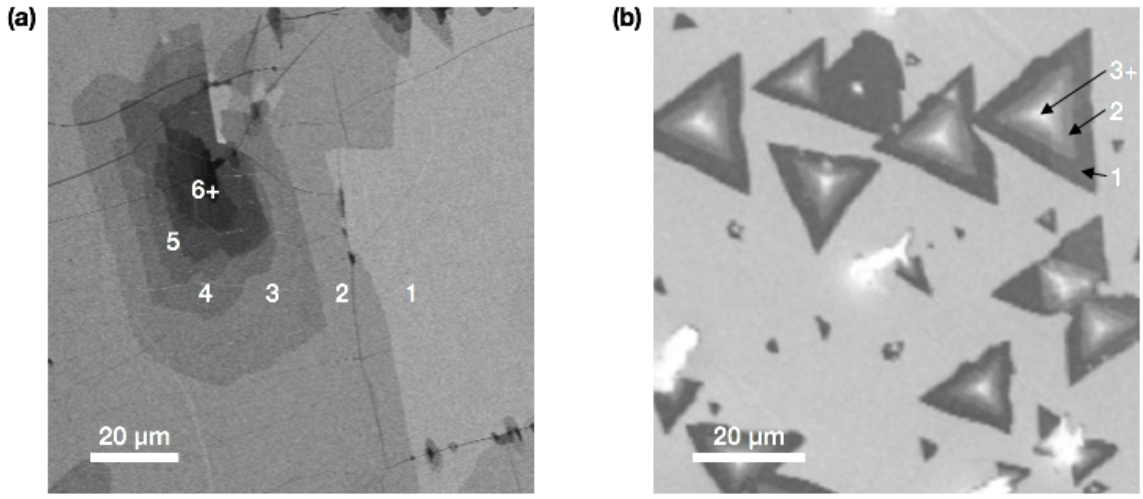

Fig. 3.5 SEM images of 2DLM. The numbers indicate the thickness of the layer (in number of atomica layers) at the respective location. **(a)** CVD Gr on Pt. **(b)** CVD h-BN on Fe adapted from reference [109].

3.2.2 Atomic Force Microscopy (AFM)

Atomic force microscopes (AFM) belong to the family of scanning probe microscopes. Detailed discussion of the principles are found in standard literature [184]. The most basic mode of operation is topography measurements of surfaces with sub-nanometre vertical (i.e. out of plane) resolution. However, it can also be used for many other types of measurements, such as hardness, friction, capacity and resistance/conductivity. Furthermore, it has already been applied for nanofabrication purposes. Fig. 3.6 shows a simplified model of an AFM. An extremely sharp tip is in contact or in close vicinity of the sample surface. The deflection of the tip is measured as it is scanned along the surface. This procedure gives information about the precise surface topography.

There are two major operation modes. As the name suggests, in contact mode the tip is in contact with the surface, or rather the liquid layer that is always present on top of surfaces in ambient environment. While scanning it along the surface, large deflections could result in damage, thus breaking the tip or the cantilever. A feedback circuit seeks to maintain constant force on the cantilever by adjusting its height. The height is adjusted for certain possible errors and output as the topography data. Errors can occur if the tip scans over suddenly changing surface features. The error or deflection signal is a measure of how well the microscope is maintaining the set point. It can be actually used to measure very small features. The disadvantage of contact mode measurement is that tips are worn quickly and prone to errors. Tapping mode makes use of a tip, which oscillates slightly below resonant

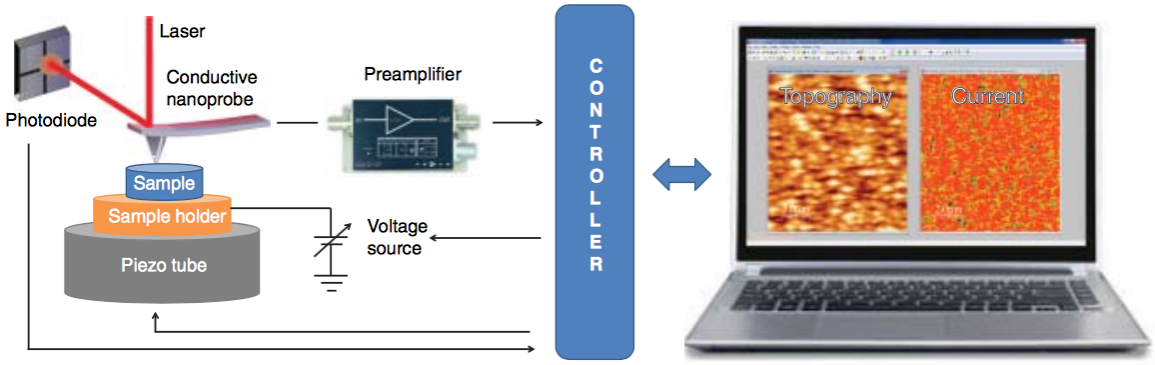

Fig. 3.6 Operating principle of AFM. Image reproduced from [**?**]

frequency in the vicinity of the surface. In the process it is "tapping" the sample. The amplitude of oscillation can be tuned around 20 nm-100 nm. The oscillation is influenced by the surface. Again the feedback circuit is used to adjust the height of the tip so that the oscillation amplitude remains constant. AFM measurements are relatively slow, as the tip has to be dragged along the surface. However, it allows quantitative measurements of the surface topology. It is often used to characterize the surface properties of 2DLMs or to measure the thickness.

3.2.3 Raman Spectroscopy

Raman spectroscopy is probably the simplest and fastest means of obtaining information about the properties of a 2DLM. Due to its high surface sensitivity, it can be used to investigate surfaces with high accuracy. Comprehensive explanations on the details can be found in literature [185]. Raman spectroscopy is based on the interaction of photons with optical phonons within a material called Raman scattering. When a sample is illuminated by monochromatic light, the energy of the photons are shifted up or down due to the absorption or the creation of a phonon. In order for Raman scattering to take place, the relation given in the equations below must hold.

$$\hbar k_0 = \hbar k \pm \hbar q - \hbar G \tag{3.1}$$

$$\hbar \omega = \hbar \omega \pm \hbar \omega_g \tag{3.2}$$

k_0 and k denote the wavevector of the incoming and outgoing phonon and ω_0 and ω their respective frequencies. q is the wavevector of the produced or absorbed phonon and

G is a lattice vector in reciprocal space. Usually lasers in the visible regime are used for experiments. Thus only optical phonons will be excited, since the energy of acoustic phonons is too low at matching wave-vectors to result in a measurable signal.

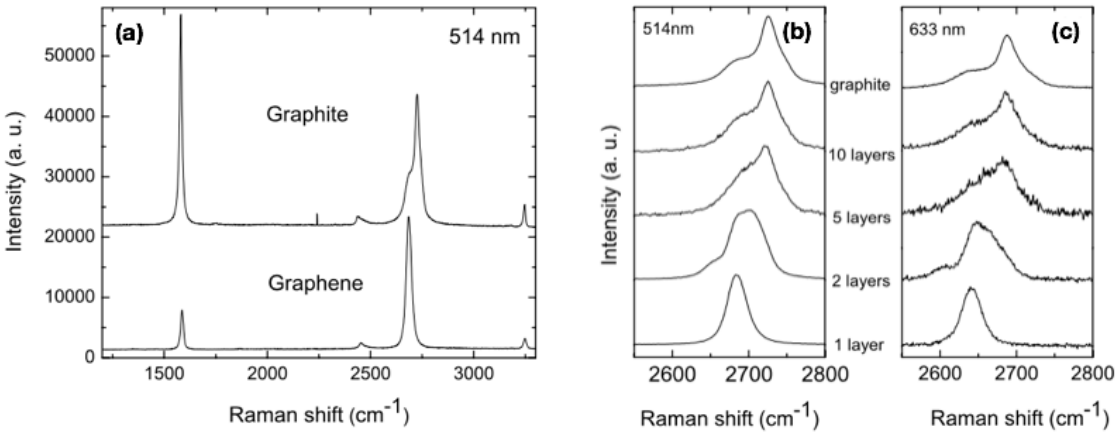

Fig. 3.7 Gr Raman spectrum reproduced from reference [186]. **(a)** Spectrum of Gr compared to graphite. The D-peak is not visible, due to high quality of sample. **(b)** and **(c)** illustrate the shift of the 2D-peak for different number of Gr sheets for different lasers

As a matter of fact, all that Raman spectroscopy provides, is a very limited insight into the dispersion relation of the material under investigation. However, this can already provide a wealth of information. The dispersion relation is specific for each material. In some cases it can even provide details about the number of layers and defects. A typical spectrum of Gr is shown in Fig. 3.7. Three characteristic peaks are visible: the 2D-peak (~2680 cm^{-1}), the G-peak (~1580cm^{-1} and the D-peak (~1350 cm^{-1}). The characteristics of the first two peaks offer information about the number of layers, while the D-peak intensity relates to the defect density [186–188]. In addition, the position of the peaks provide important information about the doping and strain of the layer. The positions of the G-peak and 2D-peak for intrinsic monolayer Gr, as measured for suspended exfoliated Gr using a 514 nm laser, are 1581.6 cm^{-1} and 2676.9 cm^{-1} respectively [189]. It should be noted that unlike the G-peak, the 2D-peak position depends on the excitation wavelength, with small wavelength resulting in a slight upshift in the position [190]. Fig. 3.8(a) displays a plot that is commonly used to assess the state of doping and strain. In general, doping will primarily affect the G-peak position, while strain leads mainly to a shift in the 2D-peak. However, both are slightly interdependent, which results in the plot below. In case of doping the peak positions will move along the doping axis, while strain leads to a displacement along the strain axis. In many cases both effects are present simultaneously.

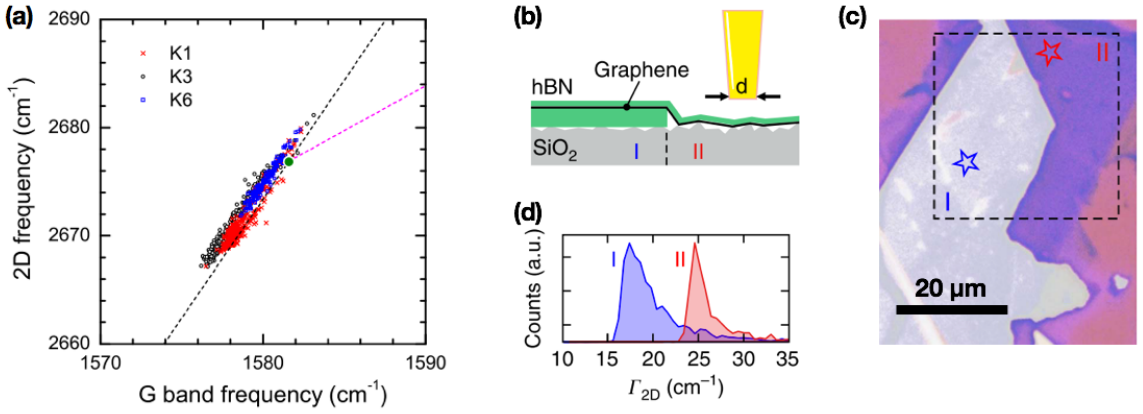

Fig. 3.8 **(a)** Fitted Raman G-peak position plotted vs 2D-peak position of three samples (K1, K3, K6). The black dotted line indicates the expected shift due to strain, the pink dotted line the shift due to doping. Adapted from reference [189] **(b)** Schematic and optical image **(c)** of sample used to investigate the effect of h-BN on the full width at half maxumum of the Gr 2D-peak. The result is shown in **(d)**. Adapted from reference [191]

.

In addition to peak positions, the full width at half maximum (FWHM) of the 2D-peak is also often used to analyse the characteristics of monolayer Gr. As shown in Fig. 3.8(b) the 2D-peak width depends strongly on the substrate the Gr is placed on. In fact, the mechanism that gives rise to this broadening is similar to the one behind the shift of the 2D-peak. Raman spectra that are recorded always give an average of the entire measured spot. It is the sum of all Raman processes that take place within the spot. As strain results in a peak shift, strain variations will lead to shifts of the Raman processes, which results in a broadened peak [192]. Overall the combination of the peak position analysis and the peak broadening offers a very detailed method to analyse the quality of monolayer Gr without actual device fabrication.

The Raman spectrum of most other materials do not allow such conclusive analysis. In the case of Gr, the relative intensities of the peaks are very useful measures. The Raman spectrum of h-BN only has a single peak, the E_{2g} peak, which offers limited information in comparison. Generally speaking the full width at half maximum (FWHM) of a peak is a good indicator for the crystallinity of a material [185]. In the case of h-BN monolayer obtained by mechanical exfoliation, which is usually considered as the highest quality material, the FWHM is between 11cm^{-1} - 14 cm^{-1} [193]. This value can be considered a baseline for CVD h-BN after transfer. Small shifts of the peak can indicate different number of layers [103]. However, also strain is known to result in shift of the peak position [193]. Another indication for the thickness of the sample is the intensity of the peak. However, such analysis requires a reference sample of known thickness. The intensity of the peak of h-BN is also very weak . It

requires long integration times to be significant compared to background noise. Furthermore, it might be covered up by larger peaks in its vicinity. This could be the case for Gr/h-BN heterostructures, since the D peak of Gr is very close to the h-BN peak.

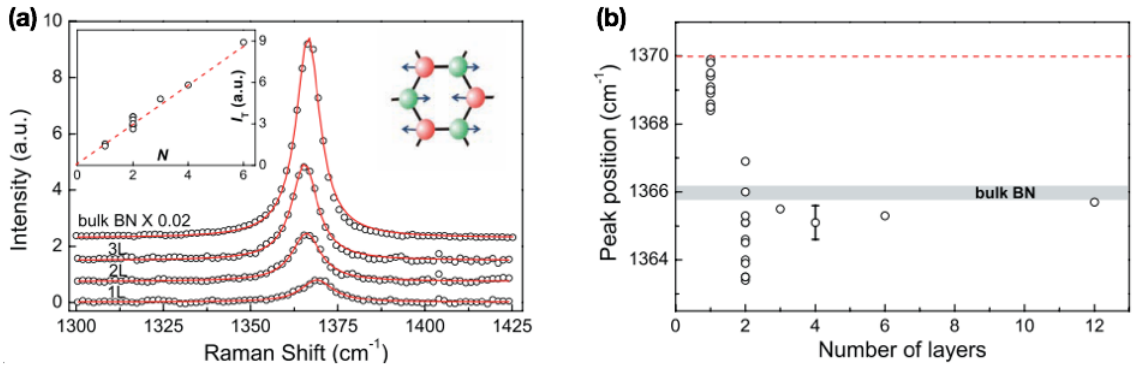

Fig. 3.9 Raman spectrum of h-BN depending on number of layers measured with 514 nm laser. **(a)** E_{2g} peak (inset shows area of peak) and **(b)** peak position of h-BN depending of number of layers. Adapted from reference [103]

Chapter 4

Improving Transfer Using Existing 2D Layered Material - Catalyst Systems

Two general approaches to improve device integration of 2DLMs have been discussed in chapter 1. The targeted design of growth processes for new 2DLM catalyst systems with the intention of enabling transfer is discussed in chapter 5. In this chapter we demonstrate how we can draft improved methods of transfer based on the understanding of the properties of the 2DLM/catalyst interface for existing systems. The goal of this study thereby is not to target record electrical mobility or other 2DLM properties. Instead we seek to understand the mechanisms involved in 2DLM transfer and to find a general approach to design and improve transfer methods in particular regarding control and reproducibility while minimising 2DLM contamination.

We focus on 2DLM grown on Cu, as this is currently the most widely used catalyst. The starting point of our rationale is the weak interaction between 2DLMs, such as graphene and h-BN, and Cu [151, 152]. Thus, gases [151] and also liquids [194, 195] can intercalate into the Cu/2D material interface. This effect is highly undesireable when it comes to surface passivation and corrosion protection [147, 153, 154]. In the context of transfer, however, it offers a new pathway towards delamination. Through intercalation, it is possible to access the 2DLM/catalyst interface, to change its chemical composition and to remove for instance interfacial oxide layers. In this way, delamination is achieved by targeted corrosion at the interface. This mechanism allows for a method of transfer, which we refer to here as Lift-Off Transfer (LOT). In general, there are two pathways for LOT, either involving both interface oxidation and selective removal in a single (LOT-I) or two different process steps (LOT-II). This approach allows us to demonstrate the transfer of Gr and h-BN single layer films from

Cu. The resulting layers are of high quality regarding surface residues, layer coherence and electronic properties. Furthermore, the catalyst is retained. We discuss our results in the context of the latest literature on CVD growth, corrosion/passivation and 2DLM transfer. We thereby foster an improved general understanding of transfer processes, which is of crucial importance to many applications.

4.1 Author Contribution

This Chapter is based on the publication [196]. All work, including the general approach, experiments and model development, have been performed by the author of the thesis. The only exceptions are the growth of the CVD samples, i.e. Gr on Cu and h-BN on Cu, and the optical mapping of the transfered 2DLM layers as given in Fig. 4.3, which was performed by co-authors of the study.

4.2 Detailed Experimental Methods

The general experimental methods have been presented in chapter 3. Here the ones that are of special relevance for this chapter and the exact parameters will be discussed in detail. This includes the preparation of the samples, i.e. growth of 2DLMs via CVD, the transfer processes and the characterization techniques that have been of applied specifically for the work given in this chapter.

Gr CVD Growth Gr growth was conducted on a 25 µm with 99.8 % purity (Alfa Aesar). All samples were grown in a commercially available Aixtron Black Magic Pro 4-inch PECVD system. The growth process begins by filling the chamber with a mixture of argon and hydrogen at a ratio of 4:1 (200 sccm : 50 sccm). The temperature is then increased at a rate of 100 °C/min. The foil is annealed at a growth temperature of 1065 °C for 30 min and for large domain Gr samples for 120 min. The precursor gas mix, which consists of 250 sccm argon, 26 sccm hydrogen and 9 sccm methane for standard and 7 sccm for large domain Gr (0.1 % diluted in argon), is then injected into the chamber. The growth time depends on the desired Gr grain size. At all stages of the process the pressure is kept at 50 mbar. Post-growth the chamber is cooled naturally to room temperature in an argon only atmosphere.

Gr grain size control is achieved by a combination of foil pre-treatment and growth time variation. For standard grain size Gr (10 µm - 25 µm) the foil is not pre-treated and

growth performed during 45 min. Large grain size Gr (200 µm - 400 µm) is obtained using electropolished Cu foils and a growth time of 4 h. The grain size is determined by stopping the respective growth process shortly before the nuclei merge completely to form a complete film and SEM/optical microscope measurement.

h-BN Growth h-BN growth was conducted using processes reported elsewhere [124]. Two different processes have been used for the samples used in the given studies. For one of these, 25 µm thick Cu foil with 99.8% purity (Alfa Aesar) was initially cleaned by sonicating in ammonium persulfate and rinsed thoroughly in de-ionized water. The foil was subsequently heated in H_2 to 1050 °C and annealed for 60 min in a hot wall furnace. Liquid borazine was used to initiate h-BN growth for 90 min and Cu foil subsequently cooled to room temperature. For the other process, 25 µm thick Cu foil with 99.8 % purity (Alfa Aesar) was directly used for growth. The samples were heated in an Aixtron Black Magic PECVD system in vacuum to 1000 °C. Liquid borazine was used to as the precursor and growth took place during 5 min, after which the samples were cooled down to room temperature.

LOT-I Gr or h-BN on Cu is spin-coated with poly(methylmethacrylate) (MicroChem PMMA 950K A4) at 3000 rpm for 40 s resulting in layer of 250 nm thickness, which is then baked for 90 s at 180 °C. The sample is then floated on a 1 M solution of NaOH (Sigma Aldrich, product number 306576, 99.99 % purity) dissolved in de-ionized water. At room temperature, the PMMA/2D material stack detaches after about 12 h for a sample size of 1 cm x 1 cm, at 60 °C after only 2-3 h. The sample is then rinsed repeatedly with de-ionized water, transferred onto the target substrate and dried at 50 °C for 1 h. In the last step the polymer is removed by rinsing in acetone and IPA.

LOT-II Gr on Cu is immersed in de-ionized water and kept at a temperature of 50 °C for 12 h. The sample is then coated identically to LOT-I and floated on hydrochloric acid (Fisher Scientific, product code 10251183, 37 %) for 5 min, upon which the sample will detach. After rinsing in water, the sample is transferred onto the target substrate and dried at 50 °C for 1 h before removing the polymer by acetone and IPA.

Wet Transfer The samples are spin-coated identically to LOT. The backside Gr is removed with oxygen plasma (oxygen partial pressure of 50 mbar, plasma power of 50 W, duration 10 s) and Cu is etched using 0.5 M iron chloride during about 2 h. The remaining transfer process is identical to LOT.

Bubbling Transfer The samples are spin-coated identically to LOT. The PMMA/2D material/Cu stack dipped into a 1M solution of NaOH and used as the cathode of an electrochemical cell with a Pt wire as the anode. Transfer was achieved by applying a voltage of 2.3 V to the cell. The remaining transfer process is identical to LOT.

Optical Characterization Optical maps were made by capturing and stitching images of the entire sample area at a resolution of 0.5 µm/pixel. A combination of normalizing all images for intensity variations and using a high-performance motorized XYZ stage allows us to generate arbitrarily large and high-resolution optical maps.

To calculate the coverage of Gr and the amount of residues, we start by calculating the wavelength-dependent contrast of Gr.55 Using the red, green and blue (RGB) spectral response functions of the CCD sensor, we can obtain the numerical values for pixels of silicon oxide, single layer Gr as well as bilayer Gr.23 Pixels that do not fall into any of these three categories are labelled as residues, and the coverage values presented in this paper thus represent a lower bound, as pixels containing both Gr and residues will only count towards the coverage of residues.

Raman Spectroscopy All measurements were performed with a commercially available Renishaw Raman system. A 532 nm laser at a power of below 1 mW was used to avoid Gr damage. Spectra were taken with a 50x objective lens.

Device Fabrication and Characterization FETs were fabricated in a two-step photolithography process. The contacts are deposited by sputtering 70 nm of nickel and subsequent photoresist lift-off. All samples were measured in air directly after processing without additional annealing. The drain current I_D is measured while applying a drain-source voltage V_{DS} of 10 mV and sweeping the backgate voltage V_{GS} from 0 V - 60 V. The maximum transconductance g_m is obtained by fitting the transfer curve. The mobility is calculated using the expression:

$$\mu_{FET} = \frac{L}{W}\frac{g_m}{C_g V_{SD}} \tag{4.1}$$

W and L represent the width and length of the channel respectively. C_g is the gate capacitance per area, which is 11.6 x 10-9 Fcm^{-2} for 300 nm SiO_2.

4.3 One Step Lift-Off Transfer

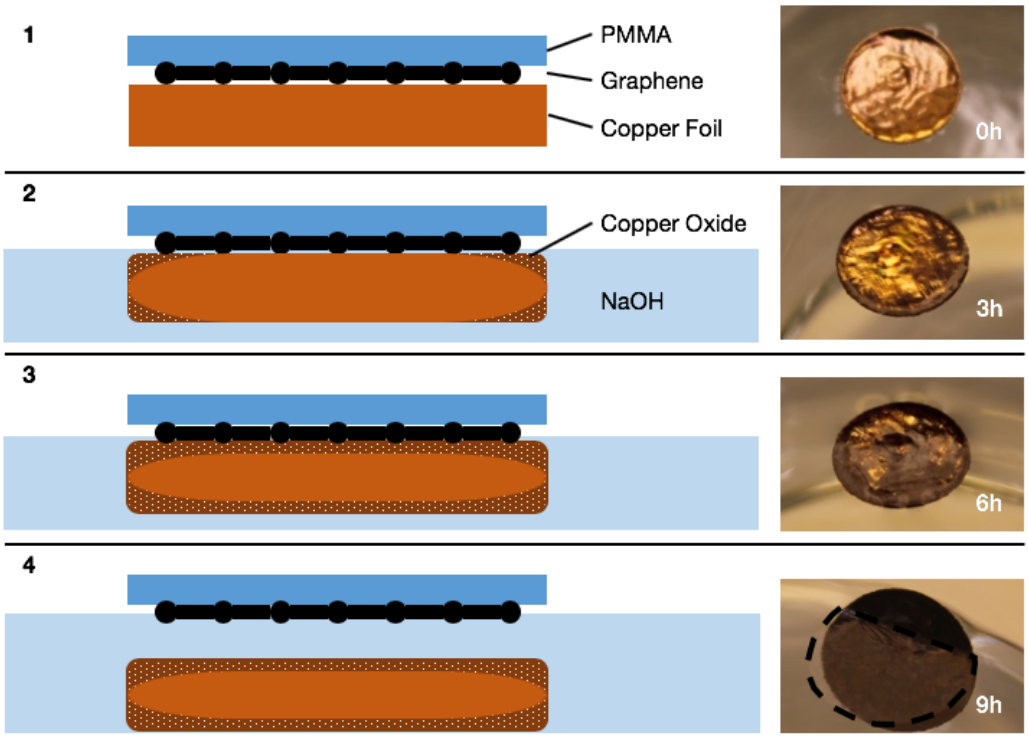

Fig. 4.1 Schematic representation of LOT-I (left) and photographs of a sample of 1 cm diameter floating on sodium hydroxide (NaOH) taken during the transfer process (right). Gr as grown on Cu is covered with a support layer (1). The sample is floated on NaOH, upon which oxidation of the interfacial Cu and the subsequent dissolution sets in (2-3). After an extended period, the whole interface layer is removed, and the Gr/PMMA stack will float freely on the liquid. For clarity, the edge of the detached film is indicated in (4).

Fig. 4.1 outlines the LOT-I transfer process, both schematically and by corresponding optical photographs of a Gr/Cu sample throughout transfer. As model system we use a simple Cu catalysed CVD process that gives a continuous single layer Gr film with an average Gr domain size in the order of 10 - 20 µm [124, 197]. After the growth process the samples are stored under atmospheric conditions. After the growth process the samples are stored under atmospheric conditions. All experiments are conducted with samples that have been exposed to ambient environment less than one month. The transfer process starts by coating the samples with a polymer support layer [in the given case poly(methylmethacrylate) (PMMA)] and then floating it on top of a 1 M solution of sodium hydroxide (NaOH). It is important to note that removal of backside Gr is not necessary for the given process. As shown in the photographs in Fig. 4.1, the Cu foil changes its colour at the edge of the sample after a short time on NaOH, which we relate to Cu oxidation [198]. Upon extended exposure, the

oxidation front moves inward towards the centre of the sample. At room temperature (RT), a Gr film of 1 cm x 1 cm will detach completely from the Cu growth substrate after roughly 12 h. When the temperature is raised to 60 °C, delamination occurs after only 2 - 3 h. We relate the decrease in process time to an acceleration of the same underlying mechanism as the progression of the oxidation front and overall appearance of the foil remain the same. After rinsing in water, the layer is transferred onto the destination substrate, dried and then dipped into acetone and isopropanol (IPA) for polymer removal.

LOT-I is based on two main processes. The first is the intercalation of the base into the interface between the 2DLM and Cu, which leads to local Cu oxidization. The following selective dissolution of the copper oxide gently releases the 2DLM film, which remains floating on the surface of the liquid. The proposed mechanism of LOT-I will be presented in greater detail in section 4.5. It is important to note that this reaction is not just limited to NaOH. In order to verify this claim, LOT-I was performed using identical processes and samples as described above, but with a 50 % weight to volume potassium hydroxide (KOH) solution. Similar to the standard process using NaOH, the Gr/polymer film detached after 12 h at room temperature. However, the samples showed a higher degree of contamination post-transfer, most likely as KOH is known to attack PMMA [200].

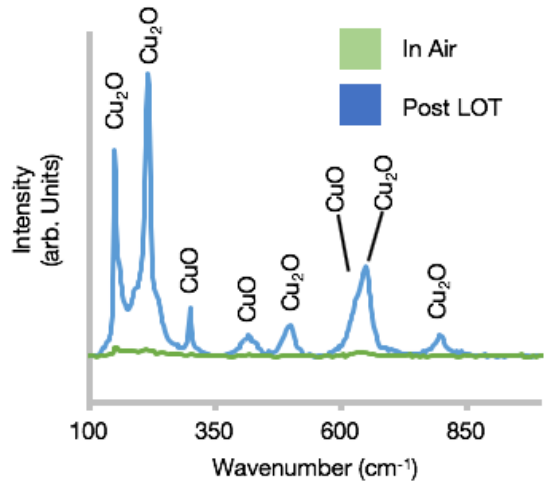

Fig. 4.2 Raman spectra of the Cu foil after LOT-I taken with a 488 nm laser. The peaks related to Cu_2O (154 cm^{-1}, 220 cm^{-1}, 492 cm^{-1}, 633 cm^{-1}, 786 cm^{-1}) and CuO (300 cm^{-1}, 340 cm^{-1}, 635 cm^{-1})[199] are indicated.

To support our model that the radial inward colour change shown in 4.1 corresponds to Cu oxidation, the surface composition of the Cu foil post-transfer was investigated using Raman spectroscopy. For reference, measurements were undertaken on an identical sample, which was grown at the same time and stored under identical conditions, but not floated on NaOH. The reference sample is thus still covered by Gr. However, any potential presence of Cu would still be visible using Raman spectroscopy, as Gr has a very low absorption throughout the whole visible range and as there are no peaks in this spectral region assigned to Gr [96]. The results of the measurement are given in Fig. 4.2. The post LOT-I Cu foil displays a set of peaks that can be assigned to Cu_2O (154 cm^{-1}, 220 cm^{-1}, 492 cm^{-1}, 633 cm^{-1}, 786 cm^{-1}) and CuO (300 cm^{-1}, 340 cm^{-1}, 635 cm^{-1}) respectively [198, 199]. These peaks are absent or very weak in the reference samples that has been

exposed to air for a limited amount of time. The result confirms the increased oxidation due to exposure to a base. Furthermore, it shows that while copper oxide is dissolved during transfer, the rate of oxidation is much higher than its dissolution and copper oxide hence remains on the foil post-transfer.

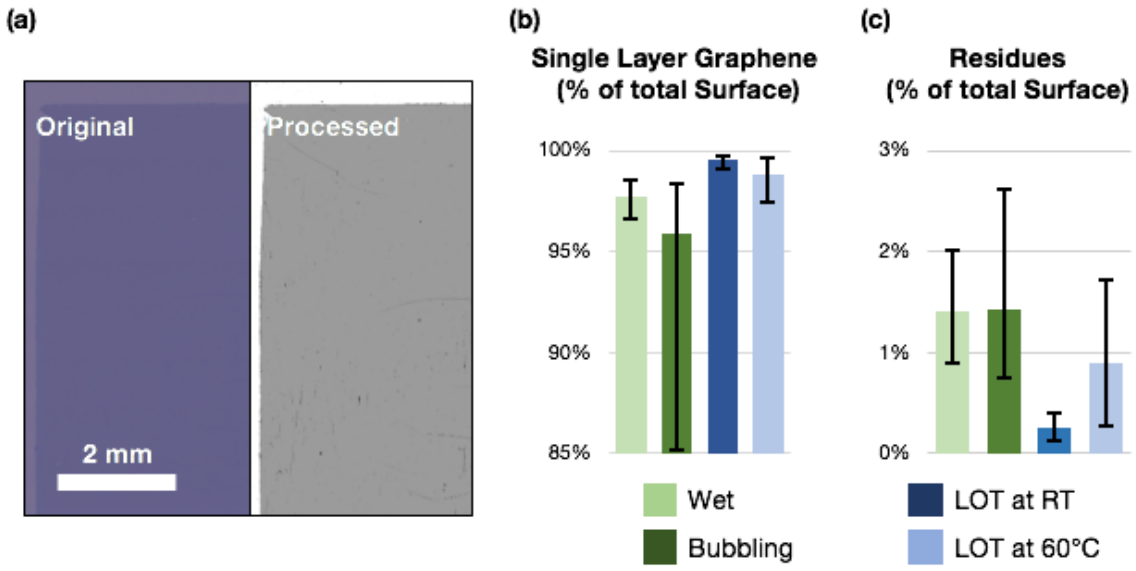

Fig. 4.3 **(a)** Left frame, Gr on a 90 nm SiO_2/Si wafer after LOT-I transfer at RT. Right frame, the same image as on the left after automated software analysis. Residue spots are more easily visible (dark dots). **(b)** & **(c)** Quantitative analysis of the surface composition as derived from the automated detection system. A large number of images from different samples were analysed regarding its composition. Plot b shows the coverage of single layer Gr; plot (c) presents the surface area covered by residues. The bar represents the median, the error bars the first and third quartile.

In order to quantify the cleanliness and coverage of the Gr layer after transfer, software-aided optical and Raman analysis was performed. The results are given in Fig. 4.3 and Fig. 4.4 . In short, during optical analysis a number of images covering the complete Gr layer are taken. A custom-made software, which is pre-calibrated for Gr transferred onto 90 nm SiO_2 due to optimal interference contrast, analyses every pixel of each image. Based on the contrast it discerns whether a pixel represents Gr, SiO_2 or other particles, which are then categorized as residues. This provides a platform to quantify the coverage and cleanliness of Gr after transfer. Fig. 4.3(a) shows an image consisting of multiple smaller pictures. It was taken by the optical microscope and stitched together during post processing. For the sake of comparison, the image after software analysis is also shown. We analysed three samples of each of the following methods to transfer continuously grown layers of Gr: LOT-I at RT, LOT-I at 60 °C, wet transfer and bubbling transfer (see methods section for details). The latter two are widely used standard techniques and serve as references. Fig. 4.3(b) and Fig.

4.3(c) show the quantitative results based on the analysis of around 50 - 100 images across the whole area of about 1 cm^2 of each respective transferred layer. The fraction of surface covered by pristine single layer Gr after LOT-I at RT is about 99 %. Residues are found on less than 0.5% of the surface. The Gr cleanliness and coherence slightly deteriorates when the temperature of the transfer is increased. Nonetheless, 97 % of the surface area consists of single layer Gr (SLG) and only 1 % is composed of other residues. We suggest the Gr quality decrease for LOT-I at elevated temperature is due to the impact of a hot alkaline solution on the polymer support layer. Based on a similar argument we point out that reducing the reactivity of the etchant and, as proposed previously, suppressing the onset of violent bubble formation could lead to improved, though slower, transfer for wet transfer and bubbling, respectively.

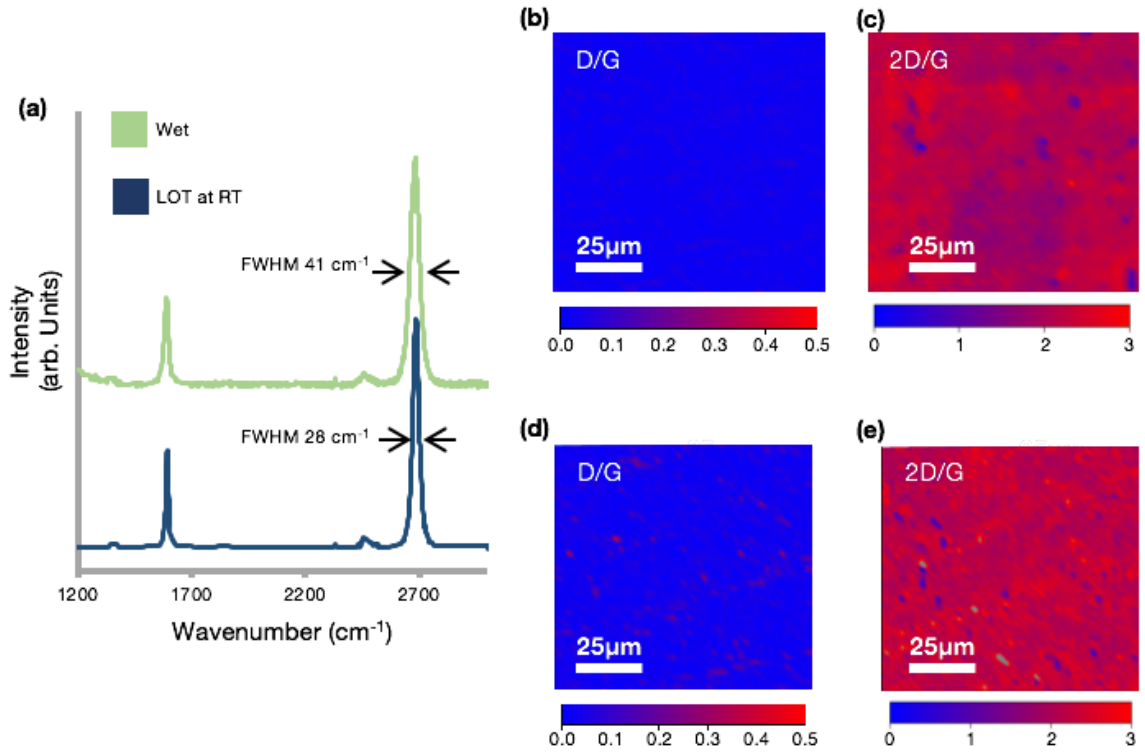

Fig. 4.4 **(a)** Raman spectrum of Gr obtained through wet transfer and LOT-I at RT. **(b)** & **(c)** Raman maps of Gr after LOT-I transfer. Map e presents the D/G ratio (average <0.03 with a standard deviation <0.01) and map f, the 2D/G ratio (average 2.25 with a standard deviation of 0.26). textbf(d) & **(e)** Raman maps of Gr after wet transfer. Map (d) presents the D/G ratio (average 0.04 with a standard deviation of 0.03), map (e) the 2D/G ratio (average 2.22 with a standard deviation of 0.27). Grey areas indicate values outside of scale. All measurements are taken with a 532 nm laser.

Nonetheless, LOT outperforms wet transfer (97 % SLG and 2 % other residues) and bubbling (88 % SLG and 2% residues). The spread of residues is also of noticeable difference

for the latter two methods. Bubbling results in large local variations of residues, i.e. regions without vs. regions with accumulation of residues, as evidenced by the large standard deviation. We suggest that this is linked to the local damage that the film sustains during the violent transfer process [173], which also results in a lower SLG coverage due to holes.

Recent literature highlights that the full width at half maximum (FWHM) of the 2D peak is an indicator for nm-scale strain variations, which negatively impact the electronic properties of Gr [192]. Fig. 4.4(a) shows a comparative Raman analysis of the Gr transferred by LOT-I at RT and by standard wet transfer. Notably for the LOT-I process the FWHM of the 2D peak is only 28 cm^{-1}. This is well below the average FWHM of samples obtained through wet transfer in our own experiments (41 cm^{-1}) as well as compared to previous studies, which report a value of around 35 cm^{-1} [42]. In fact, only dry transfer by directly picking up the Gr flake with a layer of h-BN and placing this hetero-structure onto SiO_2 leads to a similar FWHM of about 25 cm^{-1} [192]. In order to assess the Gr quality over a larger area, Raman maps of Gr transferred by LOT-I, including the D/G and 2D/G ratios, are presented in Fig. 4.4(b) and (c). For reference, the same measurements were performed on samples obtained through wet transfer. The resulting maps are given in Fig. 4.4(d) and (e). The average D/G peak intensity ratio for LOT-I transfer is below 0.03 (standard deviation < 0.01) and the 2D peak is well fitted with a single Lorentzian. The measurement yields an average 2D/G ratio of 2.25, which confirms uniform monolayer Gr across the whole measured area.

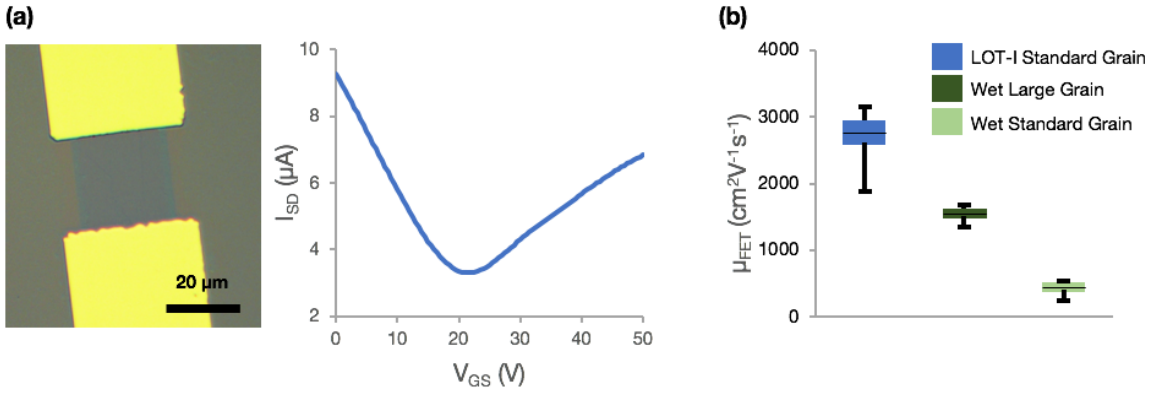

Fig. 4.5 **(a)** Optical image of FET with channel dimensions of 25 µm x 25 µm and 300 nm SiO_2 backgate oxide and transfer curve. The backgate voltage is swept from V_{GS} = 0 V - 60 V, while applying a drain-source voltage V_{DS} of 10 mV and measuring the drain current I_D. The hole mobility calculated using the maximum transconductance and a gate capacitance of 11.6 x 10^{-9} Fcm^{-2} is 3046 $cm^2V^{-1}s^{-1}$. The measurement was taken in the atmosphere after device fabrication without an additional annealing step. **(b)** FET mobility μ_{FET} of identically fabricated devices except of the transfer method. The error bars denote the maximum and minimum values; the box represents the first and third quartile.

Fig. 4.5(a) shows an exemplary individual device transfer curve and Fig. 4.5(b) compares the influence of different transfer methods on the electrical properties of Gr. A large number of two-terminal Gr devices with different dimensions were fabricated on 300 nm SiO_2/Si support for field-effect transistor (FET) measurements. A total of 15 devices fabricated with LOT-I were characterized. As a comparison, identical devices using traditional transfer methods were made. However, as bubbling transfer leads to a significant amount of holes, which is highly challenging for patterning with photolithography, we focused on wet transfer of standard (10 µm - 25 µm) and large grain size (200 µm - 400 µm) only. The results of figure 4.5 highlight that the most significant impact on electrical transport arises from non-ideal transfer methods and not from the inherent quality of Gr. LOT-I transferred Gr yields a median hole mobility of 2770 $cm^2V^{-1}s^{-1}$. This result is significantly higher than for the wet-transferred samples, which only show 1570 $cmV^{-1}s^{-1}$ for large grain size and 461 $cm^2V^{-1}s^{-1}$ for standard grain size Gr. Some variation is given, as indicated by the error bars shown in Fig. 4.5. However, we find that all devices made using LOT-I outperform ones fabricated using wet transfer.

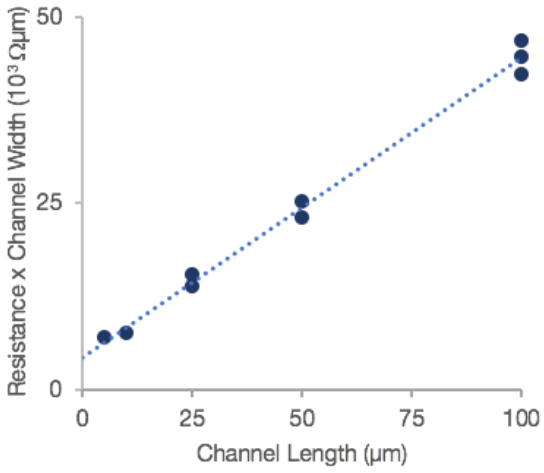

Fig. 4.6 Channel-length dependent resistance measurements of 9 devices at 0 V backgate voltage. The estimated sheet resistance is about 400 Ω/sqr and the contact resistance is 4400 Ωµm, which is at the minimum of what has been reported for optical lithography [201].

In the case of wet transfer, we suggest that acid induced polymer cross-linking [99, 165] and preferential residue accumulation along the grain boundaries are the main contributors to the diminished performance [202–204]. In particular the case of cross-linking is avoided in the LOT-I process, as the samples are only in contact with a NaOH solution. In addition to the FET measurement, it is possible to derive the contact resistance by comparing devices with different channel length due to the high uniformity of devices. In Fig. 4.6 the channel resistance at 0 V gate voltage is plotted against the channel length. We find a contact resistance of 4400 Ωµm, which corresponds to the reported minimum for optical lithography [201].

LOT-I, just as LOT transfer processes in general, can also be applied to other 2DLMs including h-BN. This allows us to establish that, despite different 2DLM properties, the main mechanisms of the LOT transfer are in fact quite similar. Here, we focus on continuous

h-BN films with grain sizes of 1-5 µm, which are catalytically grown by CVD directly on Cu.[124] Following again the LOT-I process outlined in Fig. 4.1, the h-BN single layer on Cu is spin coated with PMMA, floated on 1M NaOH, rinsed and then transferred to the desired substrate. Fig. 4.7(a) shows optical images of LOT-I and wet transfer samples for comparison. Similar to Gr transfer, LOT-I results in a clean interface with no large visible particles. Fig. 4.7(b) presents Raman spectra of as-transferred h-BN sample on SiO_2 by LOT-I and wet transfer. In both cases the Raman peak position at 1371 cm^{-1} indicates that the h-BN is single-layered [103, 193]. Raman spectroscopy can be used to assess the contamination by organic residues of an h-BN film. Previous studies have shown that organic contaminants can lead to a significant broad luminescent background [205]. In the spectra given in Fig. 4.7(b) it is apparent that wet transfer leads to an increased background in the region between about 2000 cm^{-1} and 3500 cm^{-1}, which can be related to residues. This result strongly suggests that LOT-I produces samples of improved cleanliness.

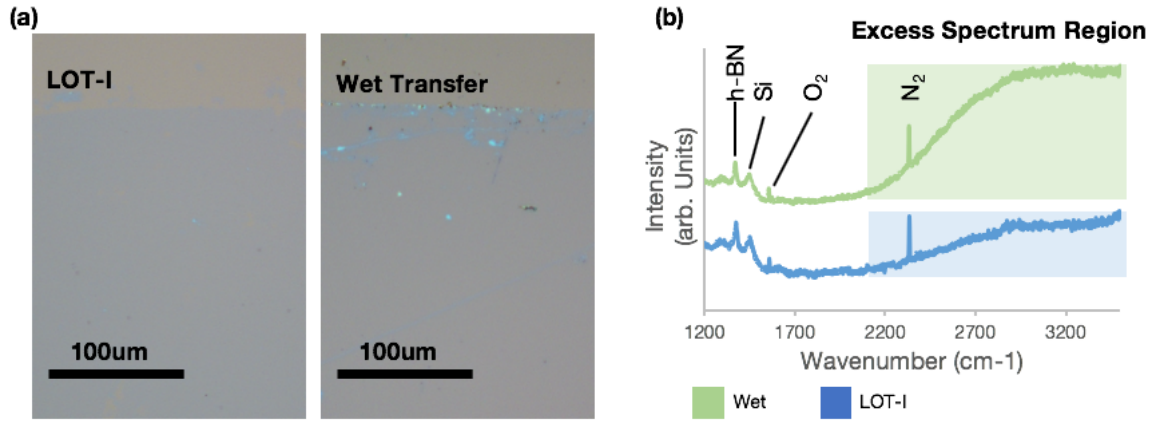

Fig. 4.7 **(a)** Representative optical images of h-BN transferred by LOT-I and wet transfer for reference onto 90 nm SiO2/Si. **(b)** Raman spectra of h-BN after LOT-I and wet transfer onto 90 nm SiO2/Si taken with a 532 nm laser. The peaks ofh-BN (1371 cm^{-1}), silicon third order (1449 cm^{-1}), oxygen (1556 cm^{-1}), and nitrogen (2331 cm^{-1}) [103, 206] are indicated in the plot. The shaded area "Excess Spectrum Region") marks the region where a bulge in spectrum due to photoluminescence is to be expected in the case of increased organic contamination [64].

4.4 Two Step Lift-Off Transfer

Thus far, our study has focussed on the LOT-I process. As mentioned earlier, based on the rationale of transforming the catalyst interface composition and selectively removing an as-formed interface layer, another approach is possible. The method which we refer to here as LOT-II is depicted schematically in Fig. 4.8(a). LOT-II essentially splits the interface

oxidation of the catalyst and the dissolution of the oxide layer into two separate processes. There are many ways to oxidize Cu at the interface. As oxygen can easily intercalate into the interface between Cu and Gr [152], a simple method is to leave the sample in ambient conditions for an extended period [42, 147]. However, in order to speed up the process, we generate Cu oxide by immersing samples in water at 50 °C for 12 h [194, 54]. The samples are then spin-coated with PMMA and floated on hydrochloric acid (HCl), which was chosen because it attacks solely the Cu oxide but not Cu itself. Within a few minutes, the Gr/PMMA stack detaches itself from the Cu foil, which then sinks to the bottom of the beaker. The film can then be processed identically to LOT-I, i.e. transferring to destination substrate, drying and removing the support layer.

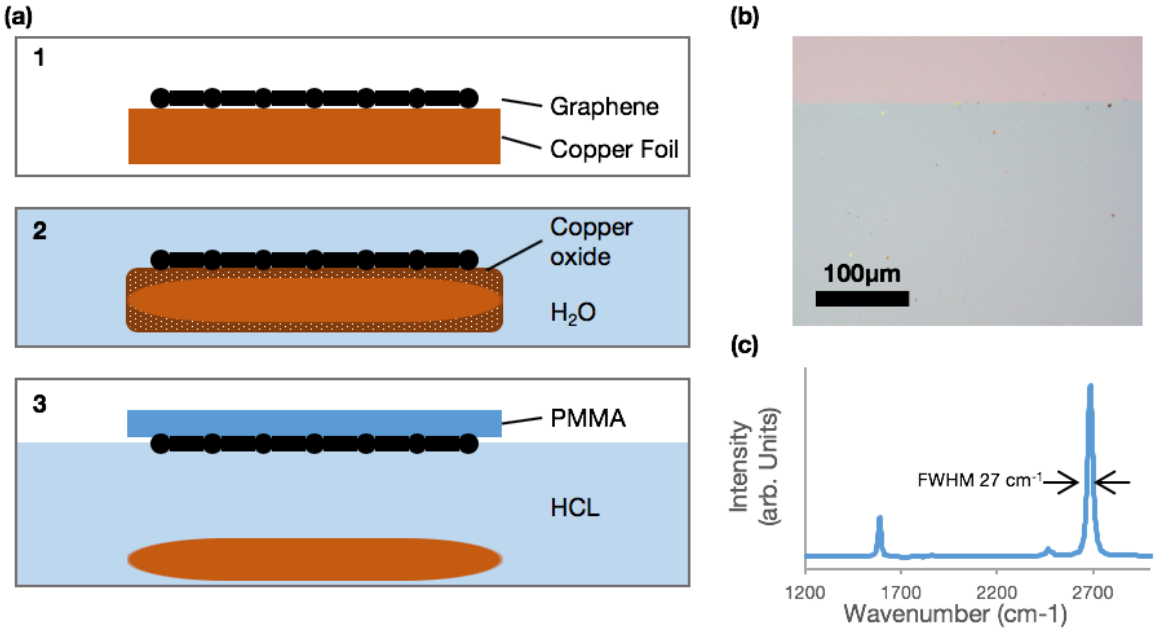

Fig. 4.8 **(a)** Process schematic of the LOT-II transfer. Gr as grown on Cu is immersed in water at 50 °C, which leads to the formation of Cu oxide (frame 1-2). The sample is then floated on HCl, which dissolves the Cu oxide and releases the Gr/PMMA layer. **(b)** Optical image of Gr transferred by LOT-II onto 300 nm SiO2/Si. **(c)** Raman spectrum of two-step LOT Gr taken with a 532 nm laser.

Fig. 4.8(b) shows an optical image of the Gr sample after transfer on SiO2. Our preliminary results indicate that LOT-II results in a higher degree of surface contamination, as shown by large particles on the sample that are completely absent for LOT-I. We relate this result to the impact of acids on polymers, which is known to be one of the main contributors to contamination in wet transfer [99, 165]. Nonetheless, the Gr is still of good quality as shown by the absence of a significant D peak in the Raman spectrum given in Fig. 4.8(b). The 2D peak is well fitted by a single Lorentzian with a FWHM of only 27 cm^{-1} , which is similar to samples transferred by LOT-I. We propose that the generation of a sufficiently thick

interfacial Cu oxide, as given for LOT-I and LOT-II, decreases the nm-scale strain variations in the Gr layer on the substrate, which is a state that is retained after transfer. This finding suggests that pre-oxidizing the Cu interface prior to wet transfer could potentially also lead to a reduction of nm-scale variation post-transfer and thus improve the overall quality of the 2DLMs.

4.5 Mechanism of Transfer

Based on the observations presented in sections 4.3 and 4.4, the following section provides a detailed discussion on the proposed mechanisms of LOT-I and -II. The general LOT transfer process consists of two distinct steps. The first is the intercalation of the solution into the interface and its oxidation. We mentioned previously that during LOT-I the PMMA/2D material/Cu stack is floated on an alkaline solution instead of being immersed. Thus, we assume intercalation only occurs from the edge of the sample. The second step is the dissolution of the interfacial oxide. Due to the presence of Cu oxide after transfer, we suggest that the rate of dissolution is smaller than the rate of oxidation.

The interface oxidation during LOT-I depends critically on how easily atmospheric oxygen can access the 2DLM/Cu interface. It has been shown that in the case of 2DLMs on Cu, gases and liquids will permeate into the interface [147, 152]. However, this is less due to direct permeation through the 2DLM, but rather a result of intercalation through defects or the edges of the sample [194, 195]. Thus we suggest that while not being perfect, 2DLMs act as a permeation barrier for atmospheric oxygen. In contrast, PMMA does not contribute significantly to the barrier function as it is highly permeable to oxygen [207].

Whether or not the 2DLM film is continuous has an important impact on the overall process. We will first discuss the case in which a continuous 2DLM film acts as a permeation barrier for atmospheric oxygen, which we refer to here as reaction path A. Assuming complete dissociation of NaOH, a 1M solution has a pH of 14. The on-going chemical reaction can be predicted using the Pourbaix diagram for Cu [208]. Oxidation occurs through the half-reactions given below

The process that actually leads to the delamination of the film is still unclear. The chemical reaction taking place is given below.

$$\text{Anodic reaction:} \qquad 2Cu + 2OH^- \rightarrow Cu_2O + H_2O + 2e^- \tag{4.2}$$

$$\text{Cathodic reaction:} \qquad O_2 + 2H_2O + 4e^- \rightarrow 4OH^- \tag{4.3}$$

Here H denotes hydrogen, O oxygen and e^- an electron. In highly alkaline solutions, cuprous oxide (Cu_2O) is not stable. It will corrode by dissolution as cuprite ions (CuO_2^{2-}) via the following half-reactions:

$$\text{Anodic reaction:} \quad Cu_2O + 6OH^- \rightarrow CuO_2^{2-} + 3H_2O + 2e^- \tag{4.4}$$

$$\text{Cathodic reaction:} \quad O_2 + 2H_2O + 4e^- \rightarrow 4OH^- \tag{4.5}$$

As mentioned in the results section, when the process temperature is raised to 60 °C, delamination of a 1 cm x 1 cm sample will result after only 2-3 h as opposed to more than 12 h for the same process at room temperature. We suggest that the reaction path remains identical, but that the process time decreases purely due to thermally increased chemical reaction rates. The process of LOT-I is driven by intercalation, oxidation and Cu oxide dissolution. An increase of temperature accelerates the rate limiting step and thus leads to the improved process speed.

A detailed schematic of the 2DLM/Cu interface is presented in Fig. 4.9(a). When the sample is first placed onto the NaOH solution, the solution will start to intercalate into the interface. It is important to emphasize that intercalation is crucial to the transfer process. If LOT were based on oxidation and dissolution of the oxide only, the result would be equivalent to wet transfer, i.e. the Cu foil would be completely dissolved. Once the liquid has penetrated the interface, Cu is oxidized to form cuprous ions (Cu^+), which then react with oxygen to form Cu_2O. For reaction path A, i.e. atmospheric oxygen is not present, the oxidation will occur uniformly from the edge of the sample towards the centre. Previous studies on the oxidation of Gr-covered Cu have claimed that Gr serves as the cathode for the half-reaction leading to oxidation in aqueous media [194]. In our experiments we have shown that LOT-I leads to identical results for h-BN or Gr. This demonstrates that the presence of Gr is not imperative for the cathodic half-reaction, i.e. the corrosion reaction can take place without a conductive 2DLM. Instead, we suggest that just as for bare metal surface corrosion in aqueous media, certain regions on the surface act as local anodes and certain others as local cathodes, thus forming local-cells for the overall reaction [209]. However the presence of Gr can change the spatial distribution of local cells due to its function as a permeation barrier, as will be discussed below.

The quantity and location of Cu_2O that is formed depends critically on the permeability of the PMMA/2D material stack since PMMA is permeable to oxygen [210]. In reaction path A, the continuous 2DLM film acts as a permeation barrier. When the 2DLM film is not continuous, atmospheric oxygen can access those regions that are not covered by

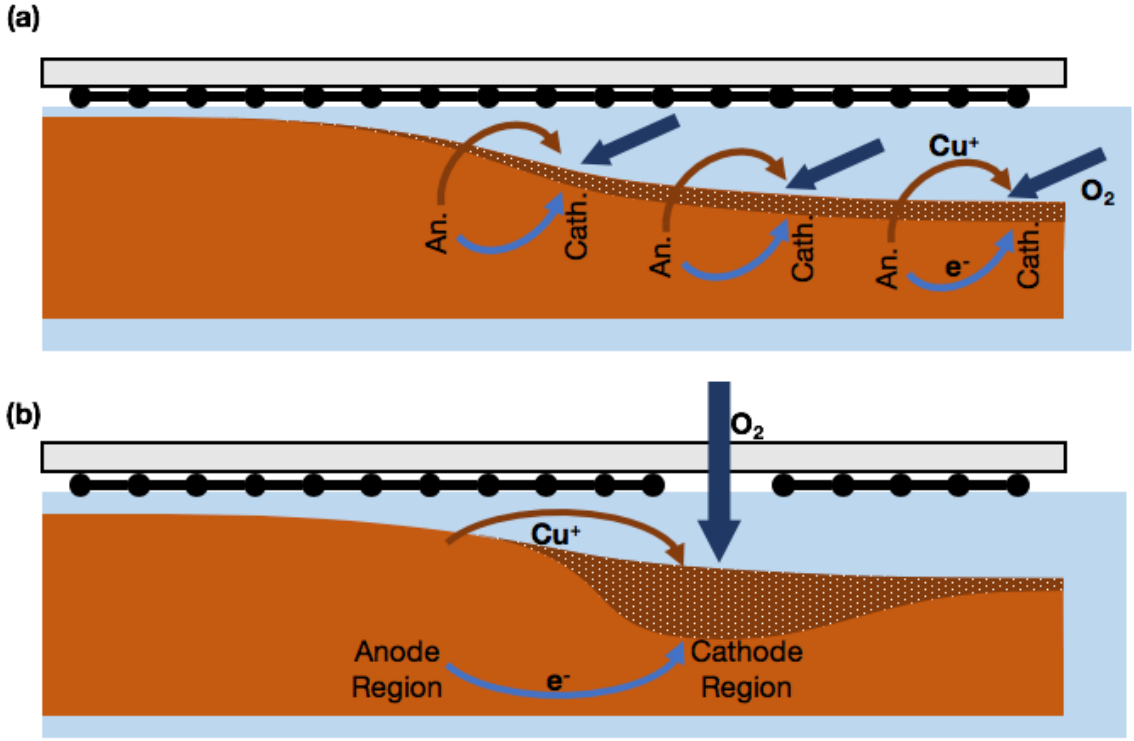

Fig. 4.9 **(a)** Schematic close-up of the 2DLM/Cu interface floating on NaOH during LOT-I transfer. The Gr layer is continuous and acts as a permeation barrier to atmospheric oxygen; i.e., only dissolved oxygen is available as a reactant. Local half cells, i.e., anode regions (An.) and cathode regions (Cath.), are formed over the surface, which results in oxidation progressing uniformly toward the center of the sample. **(b)** In this case, the Gr layer is not continuous. The gap allows for the passage of atmospheric oxygen to the catalyst surface. The abundance of oxygen establishes the cathode and anode regions. Oxide is preferentially formed at the cathode region. sample

the 2DLM. The reaction changes to what will be called reaction path B. The process in place is schematically depicted in Fig. 4.9(b). The given situation is similar to oxygen mediated localized oxide formation in the case of metal corrosion in aqueous media [209]. A well-known example is the iron oxide formation at the edge of a water droplet on an iron surface [211]. In our case, the Cu region without Gr coverage becomes the cathode of the half-reaction due to the local abundance of oxygen. Cu oxide is now primarily formed at these locations, whereas very little is formed underneath the Gr layer. Indeed, we observe that, during LOT-I transfer, discontinuous Gr layers do not delaminate - not even after several days. However, when discontinuous samples are immersed completely in NaOH instead of floating at the surface (like LOT-I), the duration of transfer is identical to that of continuous layers in LOT-I. We relate this to the fact that the influence of atmospheric oxygen is alleviated when the sample is completely immersed. In order to achieve an even better understanding of the

influence of oxygen, future studies could involve LOT-I using degassed electrolytes in an oxygen-free environment or less permeable polymers.

Previous studies have shown that while water-assisted oxidation does facilitate transfer [212, 194, 54] ultimately delamination does not occur. Therefore, both oxidation and dissolution are of critical importance for LOT-I transfers. In fact, dissolution can be indirectly observed during LOT-I. When a large piece of Gr on Cu is floated on a small quantity of 1M NaOH (e.g. 4 pieces of 1 cm x 1 cm in 100 mL 1M NaOH solution), one can observe that the solution will turn blue after an extended period (about 48 h). This can be related to the presence of CuO_2^{2-}, which has a blue colour [208]. The solubility of CuO_2^{2-} is only 10^{-6} - 10^{-4} M between pH 13 - 14 at room temperature [208]. We observed that if the quantity of NaOH solution is not sufficient, as in the example given above, delamination of the 2DLM does not occur, despite oxidation of the Cu foil.

Besides temperature, the concentration of the solution and thus the pH also have a major impact on the transfer characteristics and mechanism. The maximum pH of 15.4 as dictated by the solubility of NaOH, which is 25M, gives an upper limit to the parameter space. In order to find the dependency of LOT-I on the concentration of the solution, experiments were performed at pH 15, i.e. using a 10M solution. The first consequence of raising the pH of the solution is the increase in solubility of CuO_2^{2-}. However, at extremely high pH, e.g. pH 15, the reaction mechanism itself changes. Cu will directly dissolve, without the intermediate step of oxidation. The reaction then follows [208]

$$\text{Anodic reaction:} \qquad Cu + 4OH^- \rightarrow {CuO_2}^{2-} + 2H_2O + 2e^- \tag{4.6}$$

$$\text{Cathodic reaction:} \qquad O_2 + 2H_2O + 4e^- \rightarrow 4OH^- \tag{4.7}$$

Using 10M NaOH, we successfully transferred discontinuous Gr layers. We suggest that since dissolution can take place without prior oxidation, localized oxidation plays a smaller role in the overall process.

Compared to LOT-I, the mechanism behind LOT-II is much simpler. It is known that Cu oxidation under a 2DLM can be achieved by leaving samples under ambient condition for extended periods of time [42, 147]. However, in order to achieve sufficient oxidation in a well-controlled and fast way, we chose to oxidize the Cu foil in our experiments by immersing the sample in water at 50 °C. The oxidation reaction is the same as for LOT-I without atmospheric oxygen. When the sample is then floated on HCl, the oxide is etched

according to the reaction

$$Cu_2O + 2H^+ \rightarrow 2Cu^+ + H_2O \tag{4.8}$$

As Cu is stable to hydrochloric acid, the surface oxide is selectively etched. This results in the release of the 2DLM from the surface.

4.6 Conclusion

The interaction between a 2DLM and its growth catalyst is of crucial importance for all transfer methods that seek to overcome the interfacial adhesion. Weak interaction and weak mechanical adhesion allow for the intercalation of reactive species into the 2DLM/catalyst interface. Based on this understanding we have demonstrated that the interplay between the 2DLM and the catalyst is not only important for growth, but also decisive for transfer processes.

We demonstrated lift-off transfer of 2DLM via LOT-I and LOT-II, which both make use of the same underlying principle of local interfacial oxidation and oxide dissolution. The focus of our discussion has thereby been on the chemical processes at the interface. However, we emphasize that the chemicals used in the transfer process must also be compatible with both the 2DLM and the polymer. Previous literature highlights that for wet-transfer, the PMMA contamination can potentially be related to acid (such as iron chloride) induced cross-linking [99, 165, 166].With HCl acid used in combination with PMMA here, the LOT-II process showed a higher degree of surface contamination, despite similar underlying mechanisms. Analogous to prior reports, we suggest that the added residues are potentially a consequence of acid induced cross-linking. NaOH, as used in LOT-I, avoids these acid related detrimental effects on the PMMA, while at the same time enabling the interfacial oxidation. Compatibility with the 2DLM and support layer is an important selection criterion for the process chemicals.

The considerations in this study highlight the applicability but also the limitations of LOT, such as the requirement of intercalation of oxidizing species into the 2DLM/catalyst interface. Systems, where the 2DLM and the catalyst interact strongly, such as 2DLM/Ni or 2DLM/Fe, are known to prevent intercalation of species into the interface [153, 154], which makes LOT unlikely to succeed. LOT-I was attempted for h-BN/Ni and h-BN/Fe using a 1M NaOH solution at 60 °C . Even after a long period (> 48 h) no effect was observed. However, transfer should be possible for weakly interacting systems such as 2DLM on Pt. In

fact, a prior study has demonstrated that when Gr/Pt is floated on high pH solutions at high temperature, delamination will occur [213]. We suggest that the main underlying mechanism is similar to the one in LOT-I, i.e. corrosion at the 2DLM/metal interface.

Overall we have demonstrated the feasibility of LOT for both Gr and h-BN. The Gr samples that were obtained, were characterized by multiple methods, revealing their high quality over a large area. Using FETs made by LOT, we point out the importance of clean processing, as these clearly outperform devices made using larger grain size Gr, but non-ideal transfer methods. We also show that h-BN can be easily transferred and demonstrate the cleanliness of the layer. Further experiments based on our rationale, such as LOT-II, highlight the value and usefulness of the understanding of the interfacial processes. It is shown thereby that LOT can serve as a general process approach for improving and ultimately scaling up 2DLM transfer.

The general goal has been to develop a method that enables the fabrication and device integration of heterostructures. As discussed in this chapter, LOT is a significant improvement over existing methods such as wet transfer or bubbling transfer. Nonetheless, the methods still relies on a chemical solution, which is likely to result in contamination of the film. Furthermore, as shown for example in Fig. 4.7, the 2DLM film is still contaminated, albeit to a lesser degree than using existing methods. In order to achieve further improvement, it is necessary to take the approach or designing new growth and transfer methods with the intention of heterostructure fabrication from the start. The results of this approach is discussed in chapter 5.

Chapter 5

Optimizing CVD with Intention of Improving Transfer

Chapter 4 focused on the development of a general purpose transfer process for a given combination of catalyst and 2DLM. However, as described in Chapter 1 this is only one of two ways to approach the overall problem of device integration of 2DLMs. Instead of focusing on finding improved transfer methods for the catalyst that is ideal for growth, the strategy can also be to identify the most promising integration pathway and to tune design growth to enable the necessary processes. This approach is discussed in this Chapter.

Undoubtedly the most sutied method of integration, when only focussing on the device performance itself, is mechanical exfoliation. As mechanical exfoliation is an inherently non-scalable approach to fabrication, significant efforts have been made to replace each of the constituent layers using CVD 2DLMs in a step-wise manner [42, 56]. The approach for high mobility Gr channels has been to use h-BN flakes exfoliated from bulk crystallites to directly delaminate CVD Gr from a weakly interacting growth substrate, thus minimising transfer related defects and interface contamination. The procedure is shown in Chapter 2 in Fig. 2.18. Using dry transfer, CVD Gr has been shown to exhibit electron and hole mobilities well above 50,000 $cm^2V^{-1}s^{-1}$ at room temperature [42] and ballistic transport lengths of 28 µm have been demonstrated at temperatures below 2 K, limited solely by device dimensions, i.e. the size of exfoliated h-BN flakes [56] .

While highlighting the potential for applications particularly in optoelectronics and sensing, these examples still rely on mechanical exfoliation from bulk h-BN crystallites, giving limited, random flake size and varying thickness. Such dependence on flake exfoliation is a major bottleneck for further advances toward scalable device integration. Thus the

next logical step is to replace the h-BN obtained through mechanical exfoliation, with h-BN produced using a scalable method such as CVD. This demands new holistic process development, not only growth of large h-BN mono-layer crystals, but also their viable, clean transfer and device interfacing.

Here, h-BN growth and transfer are investigated in unison, in particular in the context of the choice of growth catalyst since both processes critically rely on h-BN interactions with the catalyst. Strong metal/h-BN interactions are preferable for applications where the h-BN remains on the metal, such as for magnetic tunnel junctions[153, 214]. To enable effective transfer, however, only weak adhesion to the growth substrate is desired. Cu, which is widely employed as a catalyst for CVD Gr and h-BN [25, 124] exhibits a weak interaction with both materials [120, 151]. The high vapour pressure of Cu at typical growth temperatures [215] leads to concerns not only about reactor contamination and a restricted high temperature parameter space, but also contamination of the 2DLM by trace Cu, which is a constraint for CMOS integration [168]. We therefore focus on Pt, which is also a weakly interacting catalyst [153] but with a lower vapour pressure and higher melting point [216]. h-BN interaction with Pt has been studied in detail for the Pt (111) surface [121, 127] Reported CVD h-BN domain sizes on Pt to date are typically only a few μm [118, 130]. Much larger domain sizes have been reported for Gr CVD on Pt [131], but in all cases 2DLM transfer relied on conventional electrochemical delamination.

Based on a in-depth understanding of the growth process, a CVD process is developed to achieve large monolayer h-BN domains with lateral sizes exceeding 0.5 mm. An overview of the growth process is given in Section 5.3. This growth process is the result of a detailed investigation of the growth mechanism using in-situ XPS and a study of the parameter space, which are given in Sections 5.4 and 5.5 respectively. Most importantly it is shown that as-grown h-BN mono-layers can be easily and cleanly transferred using an entirely delamination-based approach, which also enables the reuse of the substrate. The results are discussed in Section 5.6. These films can be used for sequential pick-up to create h-BN films of controlled layer thickness, as presented in Section 5.7. Using the same process it is possible to create Gr/h-BN heterostructures, while minimizing interfacial contamination, and to fabricate high device performance, which is discussed in Section 5.8.

5.1 Author Contribution

This Chapter is based on the publication [217]. All work, including the general approach, experiments and model development, have been performed by the author of the thesis. For

parts of the work, he was supported by co-authors of the study. This includes the data obtained from measurements by XPS (Fig. 5.2), XRD (Fig. 5.7) and TEM (Fig. 5.13). He also received support for the device fabrication and their characterization (Fig. 5.20)

5.2 Detailed Experimental Methods

In the following the experimental methods that have been of special importance for this Chapter will be discussed in detail. This includes the growth procedures used, details about the sample characterization methods and the transfer process. More general descriptions of experimental methods are given in Chapter 3.

hBN Growth All samples are grown in a custom-built Laser CVD reactor, which is discussed in detail in Chapter 3.1. Due to the beam shaper, the focal spot is limited to a size of 5 mm x 5 mm. If not specified otherwise, the Pt foil (25 µm, 99.99%, Alfa Aesar) is mounted on a tantalum (Ta) foil (25 µm, 99.9%, Goodfellow), which acts as the susceptor, enabling homogenous heating across a larger area than the size of the beam at the focal point. The Ta susceptor is clamped using sapphire in a custom-made mounting stage, and the Pt foil does not come into contact with anything but the susceptor, thus avoiding contamination and thermal dissipation. After loading the sample into the chamber, it is pumped down to a base pressure of less than 2 x 10^{-6} mbar before starting growth. The pressure is measured using a full range pressure gauge consisting of Pirani and cold cathode gauges for different pressure regimes. All gases except borazine are injected into the chamber using mass flow controllers. The flow of borazine is controlled using a manual leak valve. The precursor is sourced from Fluorochem Ltd. and is specified to have a purity of larger than 97%. It is likely that the contamination originates from the by-products of the borazine synthesis process, which is however unspecified by the manufacturer. Most likely the contamination consists of N_xB_y containing species, which given their small quantity have potentially little effect on the overall growth process [112].

Delamination Transfer As the carrier layer for delaminating the h-BN post-growth, a solution of 5g PVA (Mw 9000-10000, 80% hydrolized, Sigma Aldrich) and 1g glycerol as a softener (>99%, Sigmal Aldrich) in 100ml of de-ionized (DI) water is used. In the first step, the solution is drop-casted on the sample and dried at 80°C for 20 min. Then, the stamp/h-BN film is peeled off using tweezers, stamped onto the target substrate at 125°C, and annealed for 5 min. In the case of multilayer h-BN or h-BN/Gr heterostructures, the target substrate is

another CVD grown 2DLM sample and the peeling process is repeated. In the final step, the stamp with the 2DLM layer is put down onto the substrate of choice and the carrier layer is dissolved in DI water at 50°C for at least 3h.

Bubbling Transfer Raman measurements were performed with a Renishaw inVia confocal Raman Microscope. 514 nm or 532 nm lasers were used depending on equipment availability. Spectra were taken with a 50x objective lens. A step size of 2 µm was used for all maps. The SEM images were taken in the FEI Magellan SEM using an acceleration voltage of 1 kV. The TEM images (FEI Osiris TEM) were taken with an acceleration voltage of 40 kV. The knock-on damage of h-BN is minimized under such a low acceleration voltage. The samples are transferred using bubbling transfer in this case, as direct peeling requires PVA dissolution in DI water to release the h-BN film and the high surface tension of water is likely to damage the suspended h-BN. For the bubbling transfer only low surface tension solvents are used to release the h-BN.

In-situ XPS measurements were performed at the BESSY II synchrotron at the ISISS end station of the FHI-MPG. The setup consists of a reaction cell (base pressure 10^{-8} mbar) attached to an analyzer with a differentially pumped electrostatic lens system (Phoibos 150 NAP, SPECS GmbH) [218]. XP core level spectra were collected in normal emission geometry using a x-ray beam with a spot size of ~80 µm x 150 µm. All spectra are background-corrected (linear) and their binding energies are referenced to the contemporaneously measured Fermi edges. The temperature is measured using a dual-wavelength pyrometer.

AFM was measured in peak force tapping mode using a Bruker Dimension Icon AFM. In this mode, the feedback loop keeps the peak force of tip-sample interaction constant. XRD was carried out on a Philips Xpert MRD diffractometer with a Cu $K_{\alpha 1}$ X-ray source (λ= 1.5405974 Å) and a 4-bounce Ge(220) asymmetric monochromator. The spot size is 5 mm x 15 mm.

Heterostructure Assembly, Device Fabrication & Measurement Continuous monolayer CVD h-BN on Pt was picked up/delaminated from Pt using the delamination transfer described above. The sample is then used to pick up Gr, which was prepared in advance by mechanical exfoliation from a bulk crystal onto a SiO_2/Si wafer. For heterostructure assembly, the PVA/h-BN layer is pressed onto the wafer with Gr at 30 °C and then peeled off. This stack is then stamped onto another wafer at a temperature of 130 °C. The sample is heated at 130 °C for 5 min, before dissolving the PVA film in DI water. In order to

probe the electronic transport properties of the heterostructure we fabricate four-terminal transport geometries following an established method [219, 220]. We begin by deposition of an aluminium (Al) etch mask fabricated by electron-beam (e-beam) lithography, followed by thermal evaporation of 30 nm of Al, and lift-off. Following this, the exposed regions of Gr/h-BN are etched with a reactive ion etcher (RIE) using CF_4 gas under a forward RF power of 20 W. The Al mask is then removed by wet etching. Finally, metal contact leads are deposited by patterning with e-beam lithography followed by DC sputtering of 5/70 nm of Cr/Cu and lift-off. Four-terminal transport measurements are performed in a Lakeshore Cryogenic probe station at a pressure of ~$4x10^{-8}$ Torr and a temperature T = 290 K. The resistance is measured using a dual lock-in amplifier set-up at a frequency of ~13 Hz and bias current ~100 nA. The gate voltage is swept using an SMU.

5.3 Overview of growth process

Fig. 5.1 gives an overview of our CVD process and how h-BN growth proceeds. In its basic form, the process, which is refered to as a sequential step growth (SSG), consists of two coupled borazine exposures at different pressures (Fig. 5.1(a). In contrast, widely used single exposure at fixed temperature and pressure is referred to as "standard" growth (SG). Borazine (B3H6N3) as a combined boron (B) and nitrogen (N) precursor is used. It is isostructural to benzene and has a high vapour pressure of 340 mbar at room temperature [119]. In conjunction with the cold-wall laser CVD reactor system a well-controlled precursor atmosphere can be maintained. This is in contrast to using ammonia borane, which can exhibit a complex and evolving decomposition profile especially for hot-wall CVD reactor conditions [112]. The main findings relate to fundamental interactions with the catalytic growth substrate and hence are transferable to other B and N precursors. In particular, we note that while borazine represents a precursor with pre-defined stoichiometry (B:N = 1), it dissociates on the Pt surface. This means that the interaction of the constituent elements with the catalyst will dictate the actual supply of the elements during CVD [124]. Commercially available polycrystalline Pt foils (25 μm, 99.99%, Alfa Aesar) are used as growth substrates, which are mounted on a Ta foil (25 μm, 99.99%, Alfa Aesar) that acts as the absorber for the laser heating. The low thermal mass allows fast ramping to and from growth temperatures (T_{gr}) of up to 1300 °C. If not stated otherwise, all SEM images shown in this Chapter are taken immediately after growth with around 30 min or less atmospheric exposure for transfer. This is important as the secondary electron (SE) contrast for h-BN mono-layers can change on Pt, as we will discuss below.

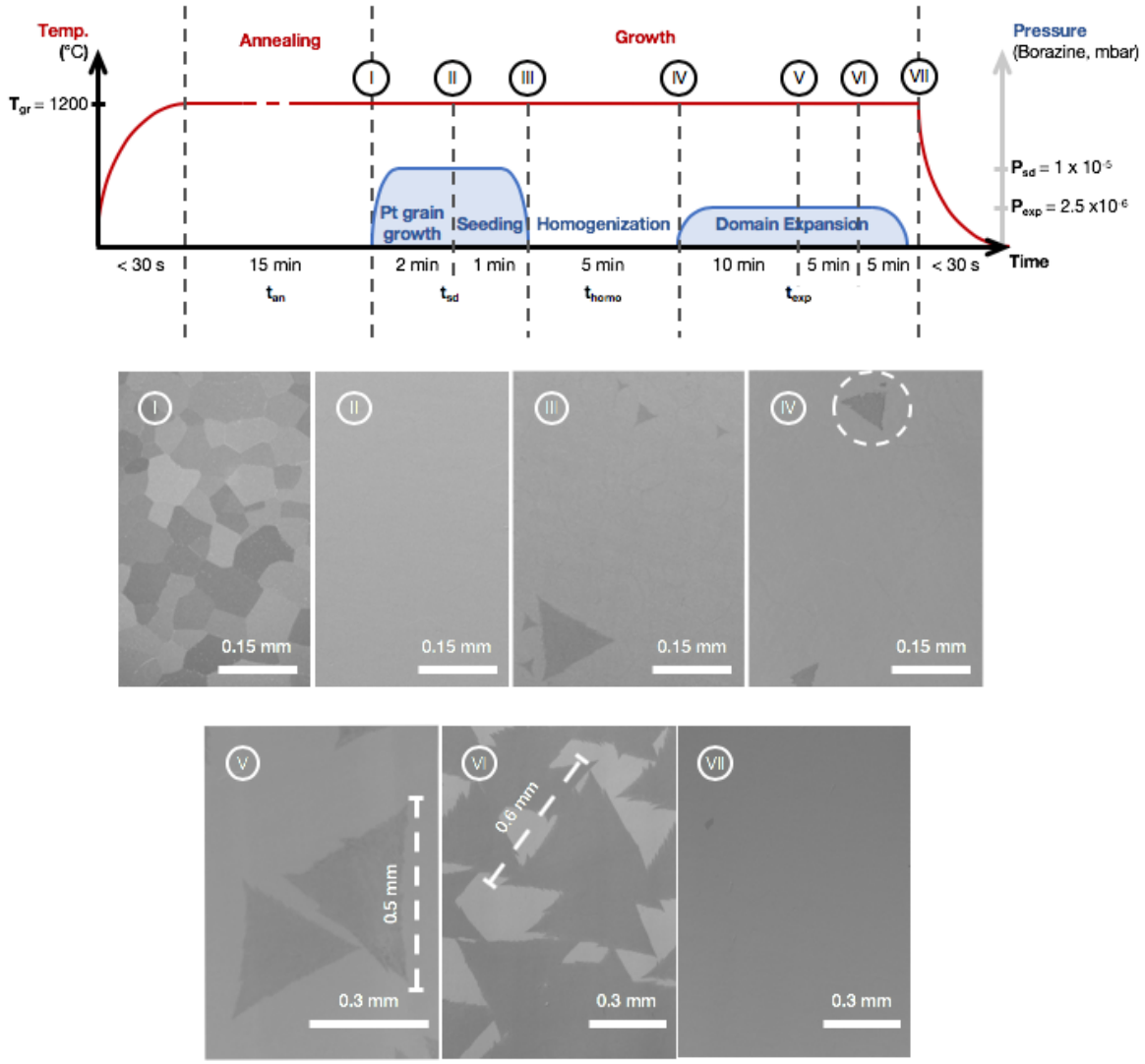

Fig. 5.1 **(a)** Process flow diagram of SSG. The growth temperature is Tgr=1200 °C. Precursor pressure during seeding is P_{sd} =1x10^{-5} mbar and P_{exp} =2.5x10^{-6} mbar during domain expansio.n **(b)** SEM images of h-BN on Pt at different stages of growth. Growth was stopped at the respective stages, by removing the precursor and turning off the laser heating. In image IV, after annealing of nuclei, damage to existing domains is clearly visible (dotted outline).

The first exposure in SSG (Fig. 5.1(a)), at relatively high borazine pressure (P_{sd}), promotes recrystallization and grain growth of the Pt foil which is initially highly polycrystalline (Fig. 5.1(b)). The mechanism and detailed investigations are discussed in Section 5.5 and Fig. 5.7. The h-BN nucleation density and homogeneity are then controlled by briefly removing the precursor during the homogenization stage (t_{homo}; see Fig. 5.1(a)), which leads to the dissolution and removal of excess h-BN. In the second exposure phase (t_{exp}) the nuclei

are then laterally expanded into large mono-layer h-BN crystals via exposure at low borazine pressure (P_{exp}). Upon further exposure, these merge into a continuous h-BN mono-layer film. The h-BN mono-layers thus grown can then be delaminated directly from the Pt, which can be reused for further growth.

5.4 Investigation of growth mechanism using in-situ XPS

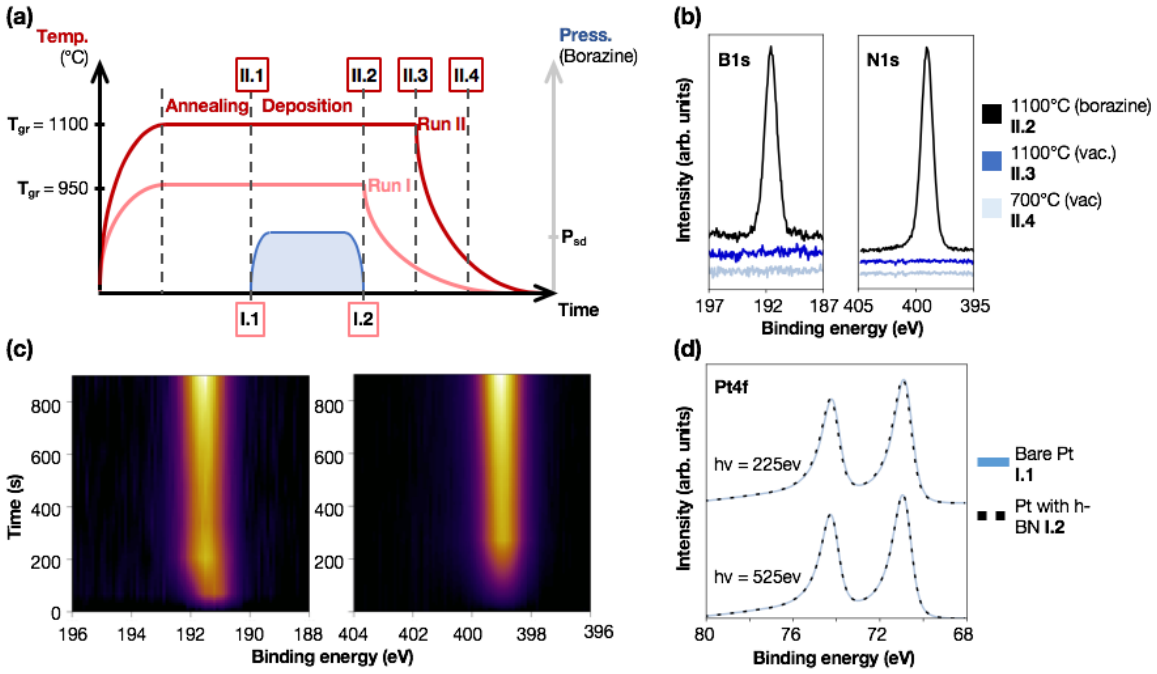

Fig. 5.2 In-situ XPS measurements during h-BN growth on Pt foil. Details on the conditions are given in the experimental Section. **(a)** Schematic process flow diagram highlighting at which point of the process the spectra shown in (c), (d), and (e) were taken. **(b)** Evolution of the B 1s and N 1s XP core level with borazine (3 x 10^{-4} mbar) exposure time (spectra taken between II.1-II.2) for a Pt foil at 1100 °C **(c)** B 1s and N 1s XP spectra taken at an excitation energy of hν= 620 eV for T_{gr} = 1100 °C with precursor present, T_{gr} = 1100°C in vacuum and RT in vacuum. The peak positions of B1s/N1s are 191.6eV/399.0eV. Shortly after removing borazine, the B/N peaks disappear and do not reappear during cooling. **(d)** Depth resolved Pt 4f XP spectra taken for Pt covered with h-BN and bare Pt at T_{gr} = 950°C. No difference in peak positions and/or additional peaks are visible, confirming the absence of potential Pt compounds.

Based on previous literature on Pt catalysed h-BN CVD growth it remains unclear whether growth occurs isothermally or via precipitation on cooling [130]. Hence, in-situ and ex-situ characterisation is applied to establish a first order understanding of the underlying growth mechanisms as basis for further process development. In-situ X-ray photoelectron

spectroscopy (XPS) provides surface-sensitive information on the growth mechanism of h-BN [109, 124].

Fig. 5.2 shows in-situ XPS measurements of a Pt foil during a basic one-step borazine exposure (process diagram Fig. 5.2(a)). XPS measurements are taken throughout the CVD process, i.e. during heating to T_{gr}, subsequent borazine exposure at constant pressure P_{sd} and cool-down. Fig. 5.2(b) shows the evolution of B1s and N1s core-level spectra taken during borazine exposure (3 x 10^{-4} mbar), at a temperature of T_{gr} = 1100 °C (step II.1 - II.2). Both the B1s and N1s spectra show the emergence of a peak that grows in intensity with time, consistent with the isothermal growth of h-BN on the Pt surface. XPS spectra measured toward the end of borazine exposure show a main B1s peak centred at a binding energy of ~191.5 eV and N1s peak centred at ~399.0 eV (Fig. 5.2(c)). We observe the $\pi \rightarrow \pi^*$ plasmon shake up satellite at ~200 eV corresponding to sp^2 bonded h-BN, which can be more clearly discerned when multiple spectra are summed to improve the signal to noise ratio as given in Fig. 5.3. Analysis of the relative peak intensities also confirms that the B:N ratio is ~1.

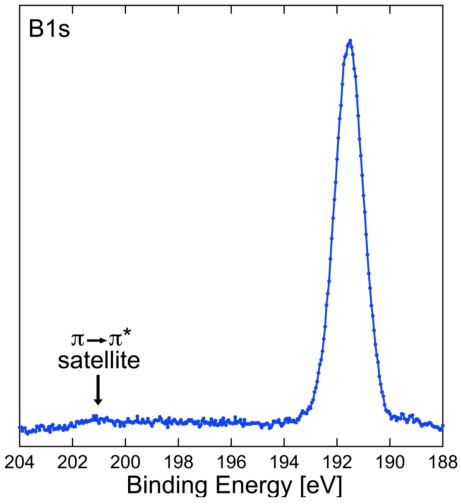

Fig. 5.3 Summed B1s XPS core level spectrum consisting of 7 spectra acquired consecutively during borazine (3 x 10^{-4} mbar) exposure for a Pt foil at 1100 °C, between 200-1100 s after borazine introduction. The improved signal to noise ratio allows the $\pi \rightarrow \pi^*$ plasmon shake up satellite to be more clearly resolved.

Based on ex-situ measurements using transmission electron microscopy (TEM) and Raman spectroscopy (given below), significant formation of cubic BN and multilayer h-BN can be excluded. Hence the given XPS signatures are assigned to mono-layer h-BN, consistent with previous literature [124, 120, 221]. After the first exposure step in SSG and when removing the precursor (temperature kept at T_{gr} = 1100 °C), the B1s and N1s peaks disappear within less than 2 minutes (Fig. 5.2c). The B1s and N1s peaks do not reappear upon cooling at these conditions. There are multiple possible explanations for the disappearance of the Pt supported h-BN mono-layer. One process that has been reported in the context of removing Gr grown on Pt is etching with H_2 at 1060 °C [222]. Other studies have investigated the stability of h-BN on SiO_2, a non-catalytic substrate, in an oxygen containing atmosphere and found the onset of degradation at 850 °C [65] and complete removal at 1000 °C [125]. The stability of h-BN may be further reduced when on a catalyst such as the growth substrate, as in the case of h-BN on Cu where

depending on the state of oxygen intercalation, the h-BN can dissociate completely at 700 °C [124].

Given the absence of any gas after precursor removal and a base pressure of below 1 x 10^{-8} mbar, the possibility of significant etching can be excluded in these experiments. Instead, it is suggested that at the given growth temperatures h-BN is not stable on the growth catalyst once the precursor has been removed. It either desorbs, is dissolved into the bulk or both. The bulk solubility of B in Pt is reported to be ~2.5 at% at T_{gr} = 1100 °C [223]. We could not find any relevant ternary phase diagrams in literature, or reliable data on N solubility in Pt, but it has previously been assumed that the N solubility in bulk Pt is negligible [118]. Simple thermodynamic bulk solubility considerations are typically inadequate for describing the growth of nanomaterials where kinetic processes and local supersaturations are often dominant [105].

To investigate the solubility and the possibility of growth via precipitation, a series of experiments were performed, which are presented in Fig. 5.4. Samples were grown at high temperature (T_{gr} = 1275 °C) following the SSG procedure. After SEM analysis the same samples were loaded again into the reactor and annealed at a lower temperature (T_{pr} = 950 °C) without any precursor. After this step, smaller secondary nuclei are formed in addition to the previous ones. We attribute this to growth by precipitation, due to supersaturation achieved by lowered solubility. These secondary nuclei are not formed during initial SSG, as the samples are quenched. The given evidence indicates not only boron (see also Fig. 5.7) but also nitrogen solubility, consistent with the h-BN layers dissolving into the catalyst bulk (Fig. 5.2(c)).

As well as revealing the presence and evolution of h-BN on the Pt surface, it is also possible to monitor the chemical state of the Pt catalyst with in situ XPS. Fig. 5.2(d) presents the Pt 4f core level spectra for bare (prior to borazine exposure) and h-BN covered Pt surfaces at two different X-ray excitation energies taken at T_{gr} = 950 °C. Photoelectrons collected with higher X-ray energy have longer inelastic mean free paths ($\lambda_{IMFP} \approx 4.5$ Å at 225 eV, $\lambda_{IMFP} \approx 7.6$ Å at 525 eV) [224], and thus higher information depth, i.e. the data represents depth resolved information about the catalyst surface composition. We observed no changes in the Pt4f spectrum compared to the clean surface indicating the absence of any significant B and N phases near the surface.

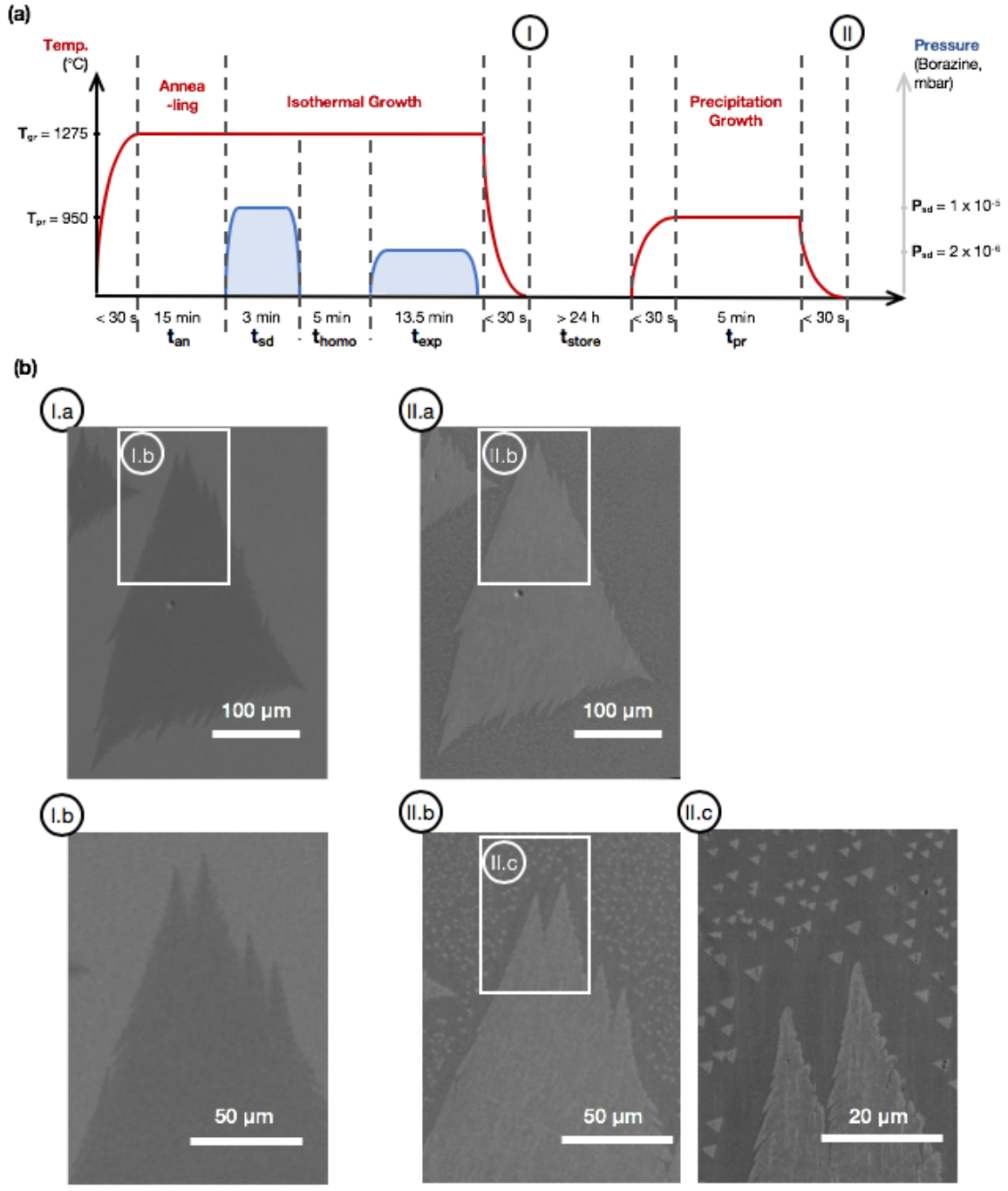

Fig. 5.4 **(a)** Schematic process flow diagram highlighting at which point of the process the spectra shown in (b) were recorded. First the sample was grown using SSG as shown in Fig. 5.1, but at higher temperature. **(b)** (I.a) & (I.b) are SEM images taken of the samples immediately after SSG growth. The sample was quenched post SSG by turning off the heater immediately. (I.b) shows the area marked in (I.a) at higher magnification. (II.a), (II.b) & (II.c) are SEM images taken of the same sample after precipitation growth. The images are taken more than 24h after the process. In this period, the samples were kept in ambient, resulting in the change of contrast associated with intercalation (see Fig. 5.15) (II.b) shows the area marked in (II.a) at higher magnification; same for (II.c) and (II.b). Smaller h-BN islands have formed in addition to the previous ones, despite absence of precursor.

The results for CVD of h-BN on Pt are consistent with a first-order kinetic growth model previously introduced for other transition metal catalysts, which takes into account precursor and elemental flux balances [124, 105]. The key findings regarding the optimized CVD process in Fig. 5.1 are that h-BN grows isothermally on Pt and no further growth occurs upon cooling due to precipitation. This is in contrast h-BN growth on Fe, where the contribution to growth due to precipitation is significant and thus control thereof is crucial for growth of large grain size h-BN [109]. At the chosen CVD conditions, h-BN growth appears to be driven by a local B and N supersaturation at the surface. At high temperatures (T_{gr} = 1100 °C, Fig. 5.2c) the Pt supported h-BN mono-layer film dissociates and at least partly dissolves into the Pt bulk once the borazine flux is removed. Within the parameter space covered by our in- and ex-situ experiments (max. borazine pressure of 10^{-2} mbar; max. temperature of 1400 °C; max. exposure time of 30 min) we only observe monolayer h-BN on Pt. This is independent of the cooling rate which we have varied from 10 °C/min to immediate quenching (temperature drop of > 500 °C in a period of ~ 5 s).

5.5 Details of growth process

A systematic set of SG experiments was carried out focusing on the role of key parameters, particularly exposure times (t_{sd} , t_{homo}, t_{exp}), exposure pressures (P_{sd}, P_{exp}) and temperatures (T_{gr}). The motivation is to find the optimal set of parameters and for each individual step of the integrated SSG process. Each step as shown in Fig. 5.1 is discussed individually in the following paragraphs.

Crystallization Given a Pt catalyst, 2DLM growth depends not only on the substrate material itself, but also on the respective facet. Different catalyst foil facets show different catalytic growth activities and lead to varying 2DLM nucleation density, domain alignment and domain shape evolution [157]. This effect can be related to differences in the precursor dissociation rate, barrier to nucleation or both. Most likely, these originate from the density of step edges on the respective surfaces [225]. Multiple studies have investigated the growth, stacking and interaction of h-BN on Pt for the (1 1 1) surface [121, 226, 126, 128, 227]. Epitaxial growth was found with two preferred orientations, which are rotated by 30 °. It was suggested that this is caused by the competition to either adapt to the underlying lattice symmetry, which results in the dominating orientation, or to minimize the lattice mismatch, leading to the other secondary one [126]. Not much is known regarding the alignment of h-BN on other crystal facets. However, it is very likely that similar epitaxial growth exists,

although with different geometries and orientations. Nonetheless, between different Pt grains, the islands will be misaligned. In fact, even when h-BN islands cross a grain boundary, the change in underlying lattice symmetry will result in a change of the h-BN domain shape. This means that even given optimized growth with extremely large h-BN domains, defects might be induced at the location of the Pt grain boundary.

In order to investigate the dependency of h-BN growth on Pt with different crystal sizes, it is necessary to obtain such substrates. One straightforward method is to anneal a highly polycrystalline samples at high temperature (high T_{an}) for an exended period (long t_{an}). There are a number of reports on thermal recrystallization of Cu foils for improved CVD of Gr, using extended thermal pre-treatment [228, 229] and thermal gradients [230]. The effect of thermal gradients and extended annealing at high temperature has also been explored as shown in Fig. 5.5 and it should be emphasized that long annealing times also lead to improved foil crystallisation.

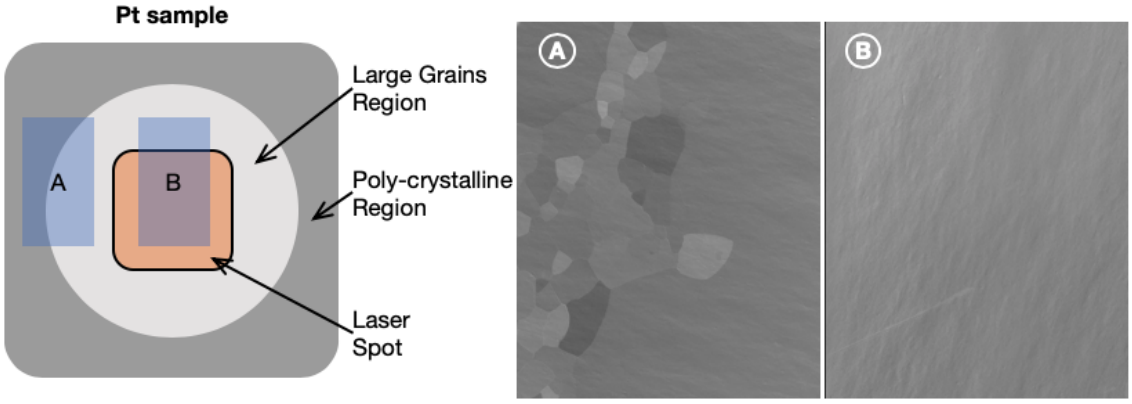

Fig. 5.5 Direct heating of Pt foil. Sample was annealed at 1250 °C for 1h in 0.5 mbar H2. SEM mages (A) and (B) are taken from different location of the foil as shown schematically in the diagram.

In Fig. 5.6 the effect of Pt crystal orientation on h-BN growth is highlighted through a set of SG experiments. In Fig. 5.6(b) the substrate itself still consists of small Pt grains on the order of tens of µ. The h-BN islands do not show any form of orientation and vary widely in size and shape. The results of an identical SG process, performed on a large grain Pt substrate is shown in in Fig. 5.6(c). The background is highly uniform, indicating a single large grain within the visible area. As expected from the uniformity of the substrate crystallinity, all h-BN islands are oriented in two directions, which differ by a 180°C rotation.

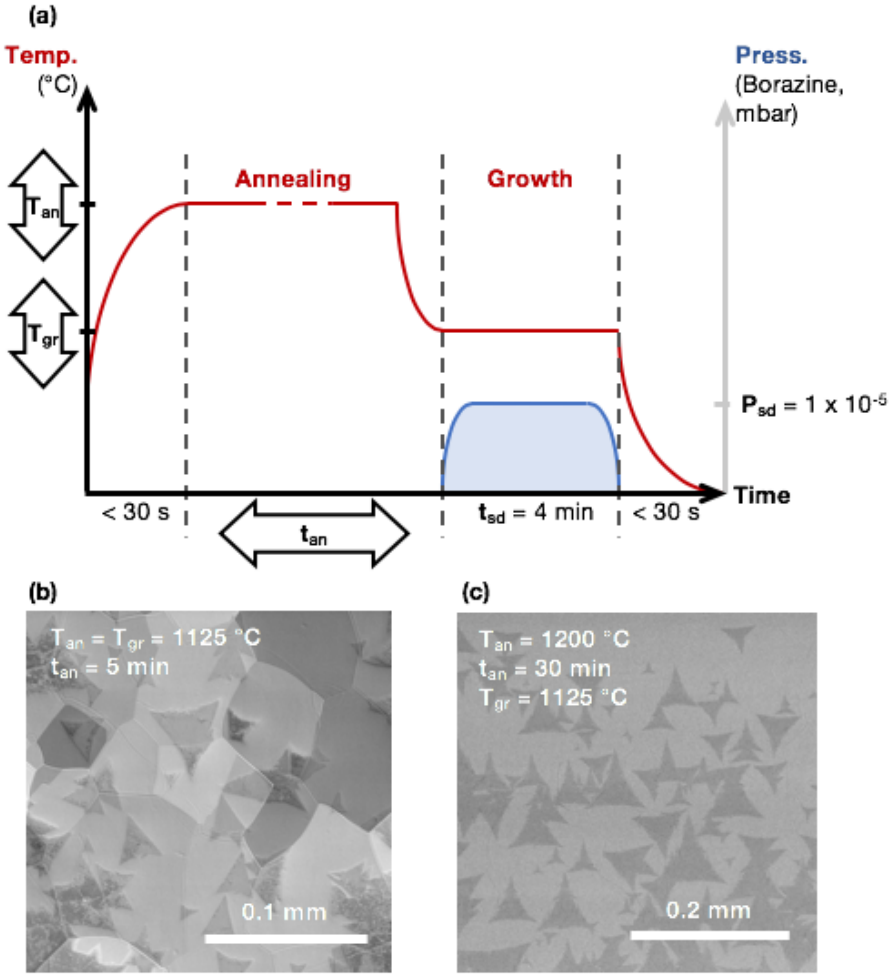

Fig. 5.6 **(a)** SG of h-BN for different growth temperatures T_{gr} and crystallinity of foil. **(b)** SEM image of baseline sample grown using standard growth (SG) process at $T_{an} = T_{gr} = 1125$ °C. **(c)** Change of crystallinity of foil. Identical growth parameter as baseline sample, but foil was pre-annealed at $T_{an} = 1200$ °C for 30 min. The uniform contrast in the background indicates single crystal Pt in field of view.

Due to challenges arising from grain dependent growth, to achieve uniform h-BN it is most desirable to grow h-BN on a single crystal or at least very large grains. Considering cost, growth on single crystals is not desirable. As shown above, it is possible to start off with a highly polycrystalline substrate and to adjust its structure prior to growth. High temperature annealing for an extended period has been mentioned above as one possibility. Fig. 5.7 shows the effect of annealing of the Pt foil and how the choice of CVD atmosphere prior to growth impacts its texture and crystallinity. A systematic set of experiments were carried out with commercial Pt foils that were annealed in vacuum for 15 min, similar to the general

SSG process outlined in Fig. 5.1, and then subjected to an additional 2 min of annealing under different gas environments (Fig. 5.7(a)).

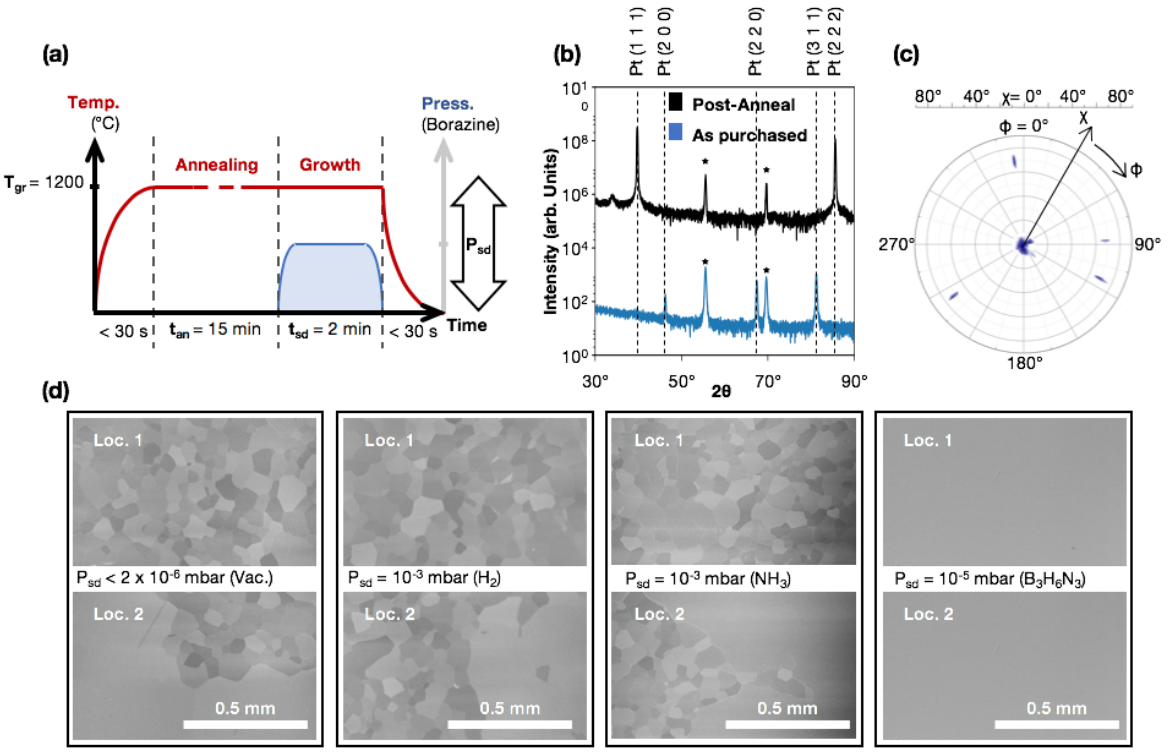

Fig. 5.7 One-step process at identical T_{gr}=1200°C for 2 min, but with different gas environments. **(a)** Process flow diagram for recrystallization baseline experiment. All parameters were held constant, only type of gas and the pressure was varied. **(b)** SEM images of Pt foils after annealing. For each experimental condition, SEM images of two locations on the same substrate were provided to highlight the differences in texture. When annealing in vacuum, H2, or NH_3, although certain polycrystalline regions remain (top images), it is apparent that the growth of large single crystal regions has occurred (bright region in bottom images). In contrast, the sample treated with borazine shows no polycrystalline regions. (c) XRD measurement of Pt foils as purchased and after recrystallization in borazine (Psc = 10^{-5} mbar, T_{gr} = 1200 °C, T_{an} = 15 min and. t_{sd} = 2 min). The spectra have been offset for better visibility (Post-Anneal spectrum was multiplied with a factor of 104). All Pt related peaks are marked. The peaks marked with * originate from the Ta susceptor on which the Pt foil is mounted. While there are multiple orientations for the pristine foil, the dominating orientation is (1 1 1) after annealing. **(d)** Texture map of the Pt (1 1 1) reflection at $2\vartheta = 39.73°$. The Pt foil behaves like a single crystal, with one pole in the symmetric position ($\chi \sim 0°$) and 3 poles at $\chi \sim 70°$ and $\varphi = 120°$ apart from each other. A minor pole is visible at $\chi \sim 70°$and $\varphi = 90°$, which indicates a minority of differently oriented grains.

For annealing in vacuum (at base pressure < 2 x 10^{-6} mbar), H_2 (10^{-3} mbar) or NH_3 (10^{-3} mbar), SEM shows a binary distribution of grain sizes. The majority of the Pt grains have a lateral size around 50 µm - 100 µm (Fig. 5.7(b), Loc. 1). A few selected Pt grains

grow significantly larger, reaching millimetre-scale (Fig. 5.7(b), Loc. 2). In contrast, when annealed in borazine for 2 min, at otherwise identical conditions, the Pt surface shows uniform SEM contrast across a few mm^2 of sample area, indicative of a dominant single in-plane orientation (Fig. 5.7(b)). No evidence of h-BN growth is observed at this stage. X-ray diffraction measurements (XRD) were taken to investigate the Pt foil texture in more detail after borazine annealing. The scan presented in Fig. 5.7(c) shows a dominant Pt (1 1 1) orientation following annealing. This is to be expected given that (1 1 1) is the lowest energy interface for FCC crystals, such as Pt. The texture map in Fig. 5.7(d) of the Pt (1 1 1) reflection (at 2ϑ= 39.73°) shows one pole in the symmetric position (χ ~ 0°) and 3 poles at χ ~ 70°and spaced by φ = 120°from each other. This is evidence that the vast majority of the Pt grains have the same orientation, i.e. the grains are not rotated relative to each other. The foil is not completely single-crystalline as highlighted by the additional weaker poles, for example the one at χ ~ 70°C and φ = 90°, which indicate that there are some grains, albeit a minority (potentially in the bulk of the foil), that are rotated with respect to the dominant orientation. It should be noted that the Pt surface roughness is not significantly altered by this process, with an average roughness measured by atomic force microscopy (AFM) of R_a = 5.3 nm for the poly-crystalline and R_a = 4.7 nm for the crystallized foil, as shown in Fig . 5.8.

Here, however, the focus is on the accelerated recrystallisation observed for borazine exposure, which has benefits as part of an integrated process. Upon thermal annealing, recrystallization is at first driven by a reduction of dislocation energy, followed by grain growth driven by the minimisation of the overall energy associated with grain-boundaries (GB). The latter involves normal grain growth where all grains grow uniformly, as well as abnormal grain growth (also known as secondary crystallization) where one type of grain will grow significantly faster than the others driven by the difference in surface energies between different grain orientations [231–235]. Our data shows that such abnormal growth in Pt is significantly enhanced by the presence of borazine. For Pt thin films it has been frequently observed that the presence of oxygen is detrimental to the formation of grains with (1 1 1) surface orientation [232, 236]. In this context B, which can readily adsorb in Pt grain boundaries [237], is frequently used as deoxidizer [238], and the addition of B to Pt has been seen to cause GB unpinning [235]. We therefore attribute the accelerated abnormal Pt grain growth to GB unpinning via removal of pre-existing solutes. Another potential mechanism could be B causing solute drag by decorating and pinning selective GBs, leaving only high mobility GBs able to grow. Having established the rationale for the catalyst foil crystallisation step, now each subsequent step in the SSG process (Fig. 5.1(a))

will be discussed in detail. This includes the seeding, homogenization and domain expansion steps.

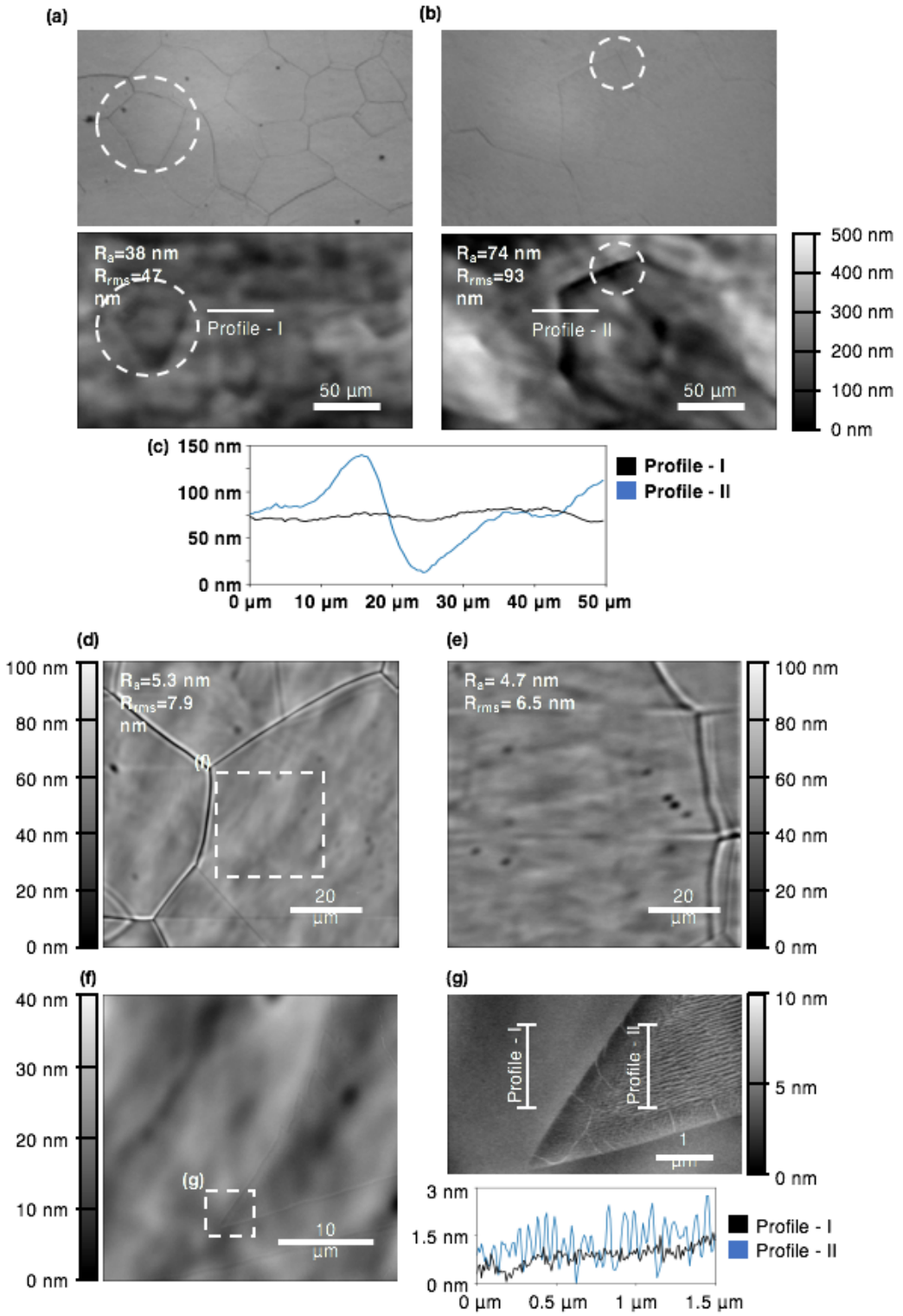

Fig. 5.8 White light interferometer (WLI) **(a)-(c)** and PF-AFM **(d)-(g)** measurements of h-BN on Pt after growth for polycrystalline [(a), (d), (f) & (g)] recrystallized [(b) & (e)] Pt foil. In (a) and (b) the surface map by WLI and the corresponding optical image are shown. Common features are highlighted by dotted circle for better visibility. The origin of the apparent difference in roughness is highlighted in (c). The surface profile of the recrystallized foil shows, that the higher roughness originates from a large-scale curvature of the foil. The comparison of PF-AFM images of polycrystalline (d) and recrystallized (e) foil, shows that on small scales, the roughness is similar. (f) & (g) are magnified images of (d) & (f), corner of an h-BN island. It should be noted that the h-BN is mainly visible due to a change in measured roughness and not step height.

Seeding Knowing the influence of temperature and Pt grain orientation, the most obvious approach for growing large islands of h-BN would be to recrystallize the substrate and grow at the maximum temperature. The motivation hereby is that in general increase in temperature can result in an increase of the growth rate, while reducing the nucleation density [20]. However, by continually increasing the deposition temperature, eventually nucleation and growth rate will reduce, due to the increased desorption, the instability of the h-BN nuclei or both. This is highlighted by a series of growth results in Fig. 5.9

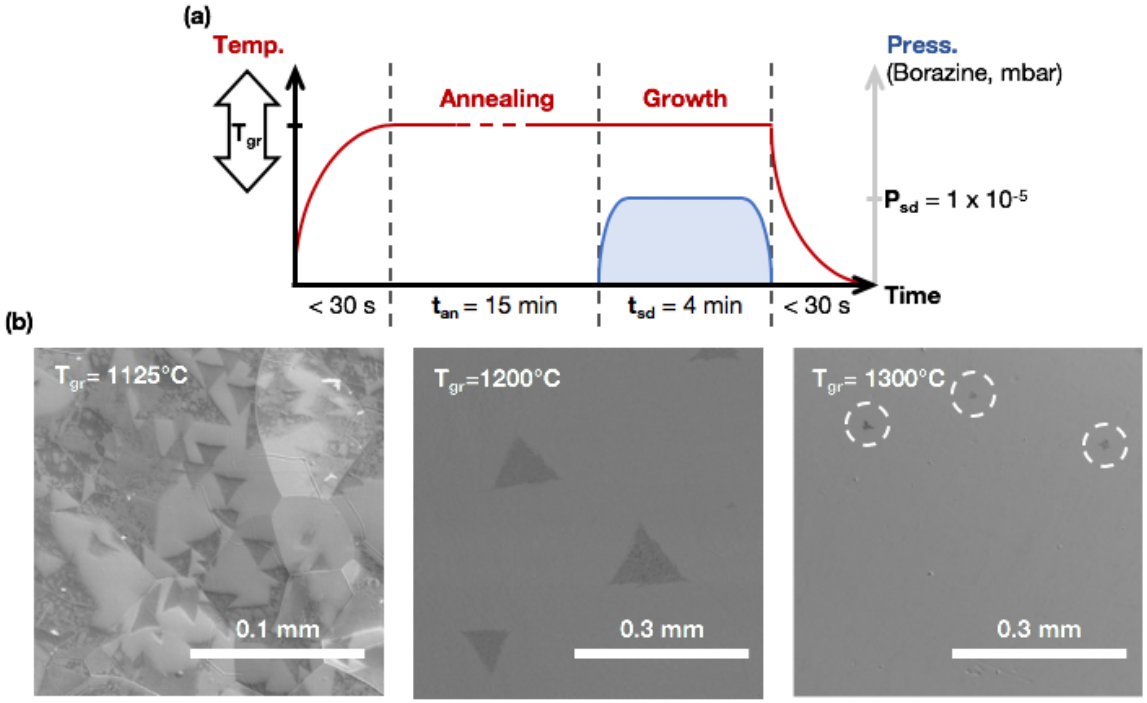

Fig. 5.9 **(a)** SG of h-BN at different temperatures Tgr, while keeping all other parameters constant. **(b)** For each SEM image the growth was stopped at the respective time by quenching the sample. An increase of temperature leads to reduced nucleation (different scale bars chosen for improved visibility). Increasing the temperature further does not have significant impact on nucleation reduction, but growth is slowed.

In Fig. 5.10, a series of SEM images show the outcome of SG growth experiments at a precursor pressure (P_{sd}=1x10^{-5} mbar) corresponding to those used in the first SSG step (Fig. 5.1(a). After initial nucleation at t_{sd} = 3 min, not only will these islands grow, but additional nuclei will form. This is clearly evidenced by the difference in h-BN island size. Furthermore, this secondary nucleation limits the attainable maximal size, as islands will coalesce at an early growth stage. In SSG, the main underlying idea is to achieve low initial nucleation density and then to grow the h-BN film from these nuclei, while avoiding further nucleation.

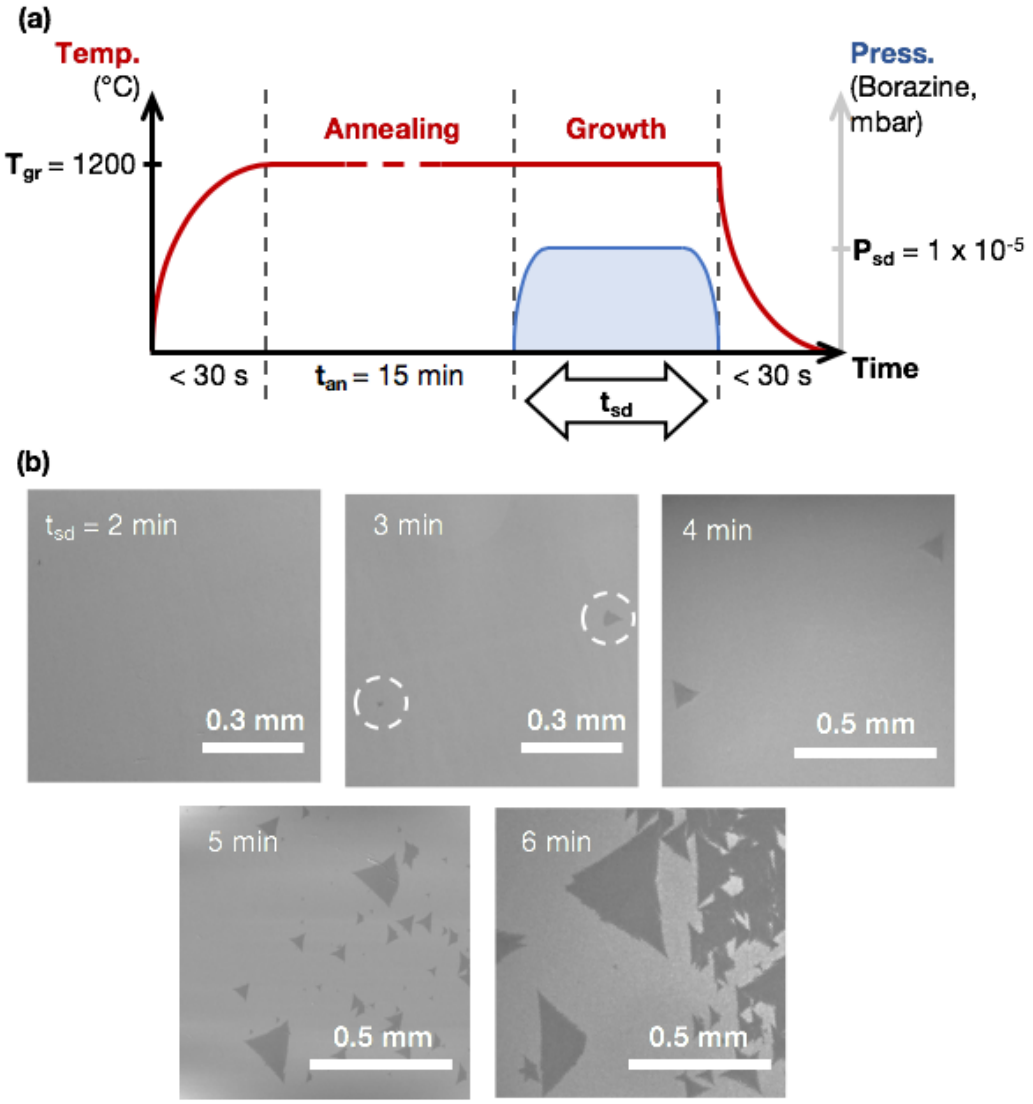

Fig. 5.10 **(a)** Process flow diagram for SG at Tgr=1200°C and precursor pressure of P_{sd} =1x10^{-5}mbar, while varying the growth time tsd. **(b)** SEM images of the samples after growth. For each SEM image the growth was stopped at the respective time by quenching the sample. After 3 min, the onset of nucleation begins (nuclei marked by white dotted circles). These grow in size, however, at 5 min, secondary nucleation sets in. While there will be very large islands formed eventually (>0.4mm after 6 min), there is a large number of smaller nuclei that prevent their continued growth due to coalescence.

Homogenization The effect of the homogenization step is highlighted in Fig. 5.11. The topmost images in Fig. 5.11(b) and 5.11(c) represent the outcome of seeding for t_{sd} = 3 min and t_{sd} = 5 min prior to homogenization (i.e. t_{homo} = 0 min, compare to Fig. 5.10). For t_{sd} = 3 min a few h-BN domains of very similar sizes have nucleated. At t_{sd} = 5 min these h-BN domains have grown in size, but secondary h-BN nucleation has occurred as evidenced by the

many additional smaller domains. It should be noted that the onset of secondary nucleation varies and starts occurring from t_{sd} = 3min onwards. This highlights a key challenge for controlling the microstructure of the resulting h-BN.

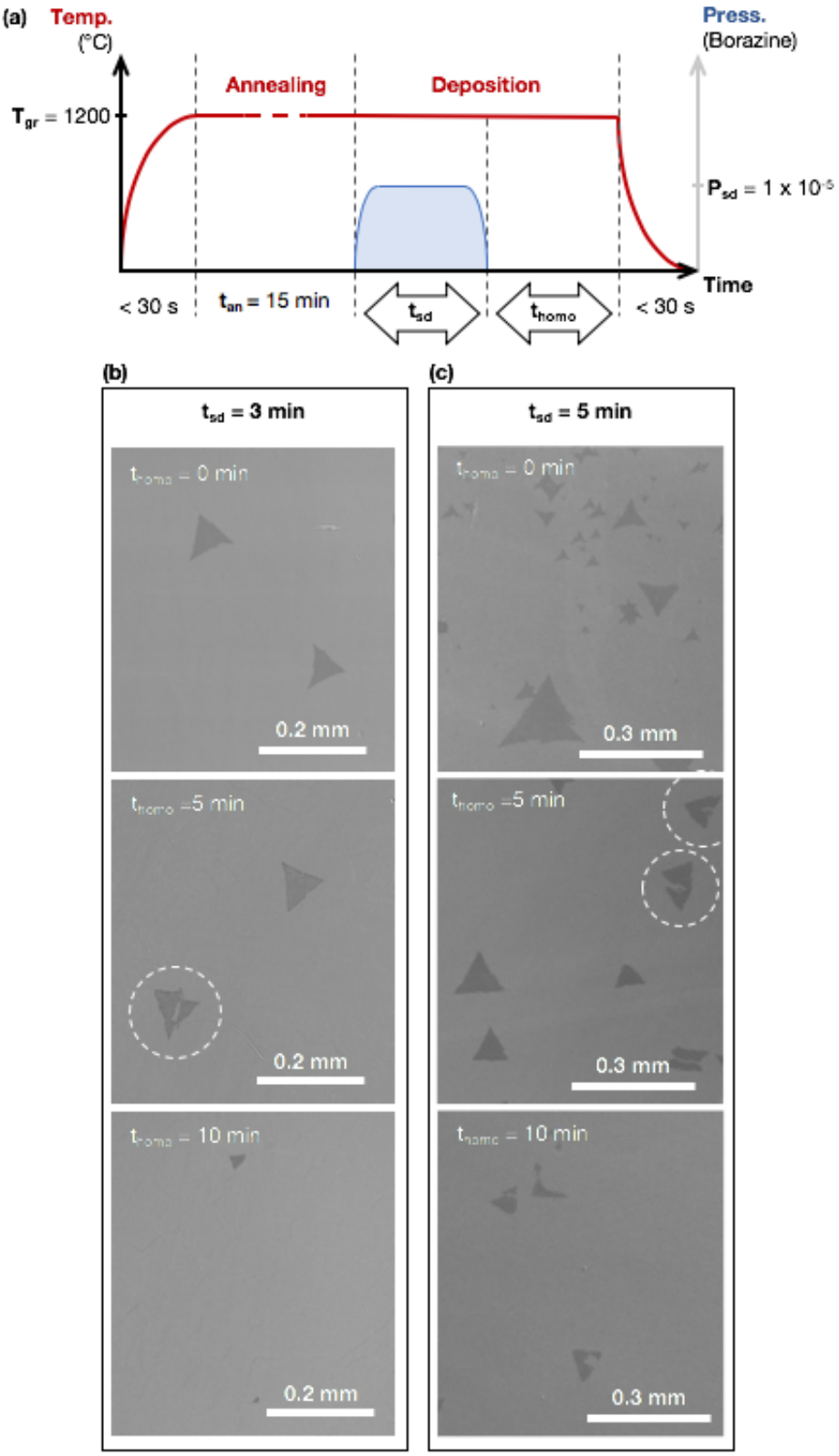

Fig. 5.11 **(a)** Schematic process flow diagram for SG experiment to highlight the effect of seeding and homogenization. **(b)** & **(c)** SEM images of growth result. Growth was stopped at the respective stages, by removing the precursor and turning off the laser heating. All parameters were kept constant, except of t_{sd}, which is varied between the series [3min in (b) and in 5 min (c)] and t_{homo} , which is varied within each of the series.

A high precursor exposure pressure is desirable to minimise incubation time and achieve rapid nucleation and growth, however the accompanying secondary nucleation is detrimental to achieving large domain sizes. Thus a homogenization stage is introduced in SSG, and Fig. 5.11(b) and 5.11(c) show the effects of increasing t_{homo}. After t_{homo} = 5 min all smaller h-BN secondary nuclei have disappeared (Fig. 5.11(c)) and for t_{homo} = 10 min also the larger h-BN domains are removed or significantly reduced in size. The XPS data (Fig. 5.2) showed that existing h-BN nuclei are unstable and start to dissociate when borazine is removed. Given a constant rate of dissociation, it is expected that smaller nuclei will disappear first, consistent with this data. This enables the control of the h-BN nucleation density, which justifies the choice of t_{homo} = 5 min to achieve optimal growth results (Fig. 5.1(a)). In general, the overall parameters are highly interdependent. Thus the suggested time of t_{homo} = 5 min is optimized for the given set of parameters of temperature, precursor pressure, seeding time and catalyst dimensions.

It should be noted that simply reducing the precursor pressure, an often employed strategy to decrease nucleation density, does not have the same effect as the combination of seeding and homogenization. In Fig. 5.12 the result of SG at a low precursor pressure of P_{sd} = 2.5 x 10^{-6} is shown. As to be expected, the onset of nucleation occurs at a much later stage compared to higher precursor pressures (see Fig. 5.10), but once nucleation sets in, it is of comparable density, thus highlighting the necessity of the separate seeding and homogenization steps.

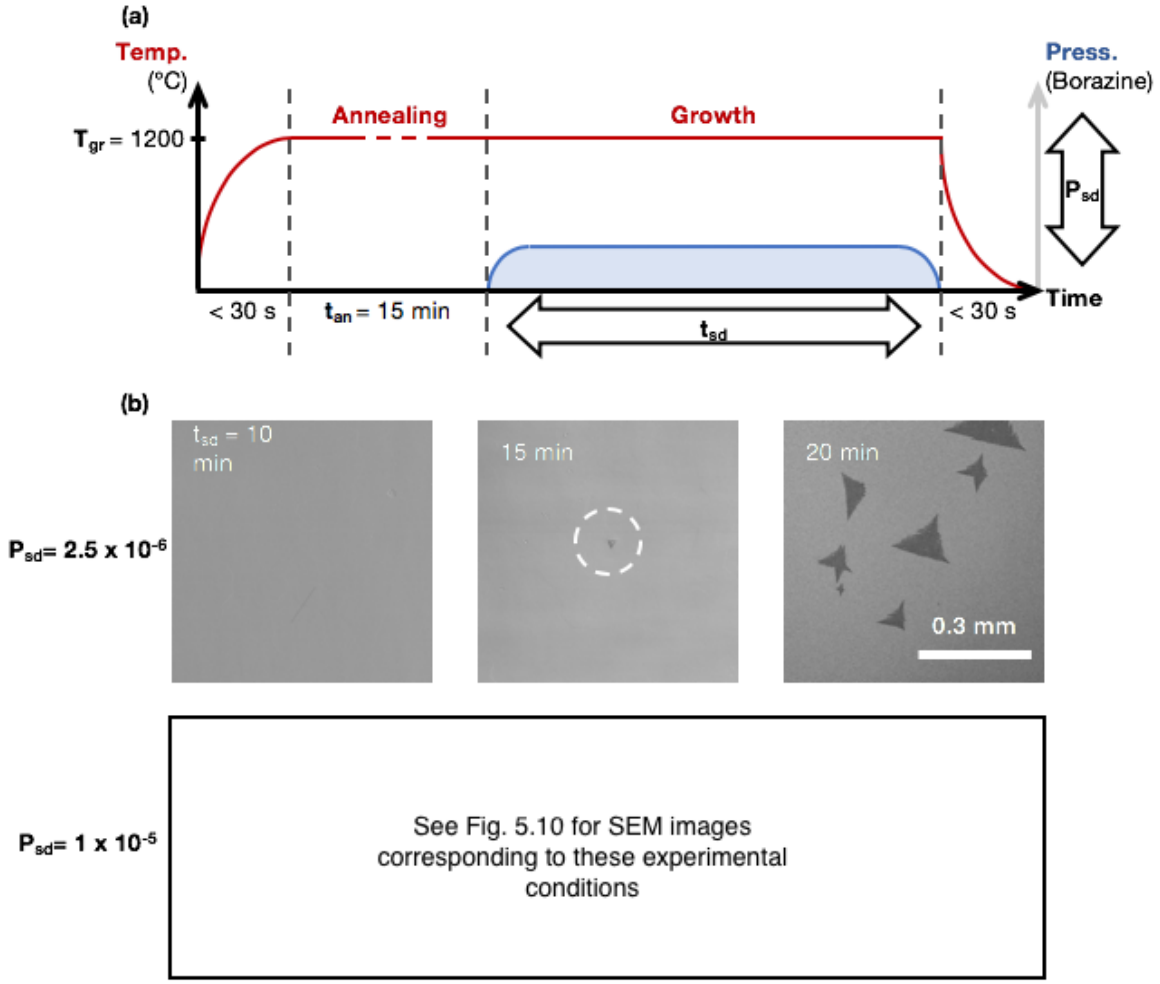

Fig. 5.12 **(a)** SG at T_{gr}=1200°C. The precursor pressure of P_{sd} is varied. In order to show the effect on nucleation and growth, the growth was stopped at different times tsd. **(b)** Comparison of nucleation between P_{sd} = 2.5 x 10^{-6} mbar (shown here) and P_{sd} = 1 x 10^{-6} mbar (shown in Fig. 5.10). Due to the lower precursor pressure, a much higher incubation time is required before the onset of nucleation. After 15 min of precursor exposure, the first nuclei are formed. When extending the exposure time, more nuclei form, as evidenced after 20 min. The scale bar applies to all SEM images.

Domain expansion Following homogenization (see Fig. 5.1(a), IV-VII) the expansion of existing domains is performed at a lower borazine pressure of P_{exp} = 2.5 x 10^{-6} mbar. Through this separation of nucleation and domain growth, secondary nucleation is effectively suppressed, while growth of existing domains continues. Thus it is possible to achieve extremely large h-BN domain sizes in excess of 0.5 mm.

5.6 Characterization of h-BN crystal alignment

A combination of characterization techniques is used to assess the quality of the h-BN films. Fig. 5.13(a) shows a representative bright field (BF) transmission electron microscopy (TEM) image. The h-BN film is only indirectly visible by the presence of a suspended particle (see dotted circle, Fig. 5.13(a)), which highlights that the h-BN is uniform and has little contrast and/or features. The selected area electron diffraction pattern in dark field (DF) TEM (Fig. 5.13(b) shows sets of hexagonal diffraction patterns consistent with single crystal mono-layer h-BN. To determine the crystal orientation over a reasonably large area, DF-TEM diffraction patterns from various points across the h-BN film were recorded and analysed. The angle α is defined as the angle between the vertical and the closest first-order diffraction spot in a clockwise direction (Fig. 5.13(b). The resulting distribution of α is summarised in Figs. 5.13 (c) and (d). For most recorded diffraction patterns α lies within a margin of $\pm$ 2.5° of the median (α_{med}). The peaks at -30° and 30° Correspond to identical orientations due to the hexagonal lattice symmetry. This distribution of orientations is in good agreement with previous studies [126], and highlights that the h-BN is highly crystalline. Over the mapped area (~2 x 2 mm) the TEM signature is as expected for a single crystal, although we cannot rule out small rotations below the limit of resolution or defects induced by imperfect merging of domains. Figs. 5.13 (e), (f) show the edge of the film, with only one fringe visible, consistent with mono-layer h-BN. The region marked with the white arrow in Fig. 5.13(f) corresponds to a fold. The contrast between the h-BN mono-layer edge and folded edge can be clearly seen.

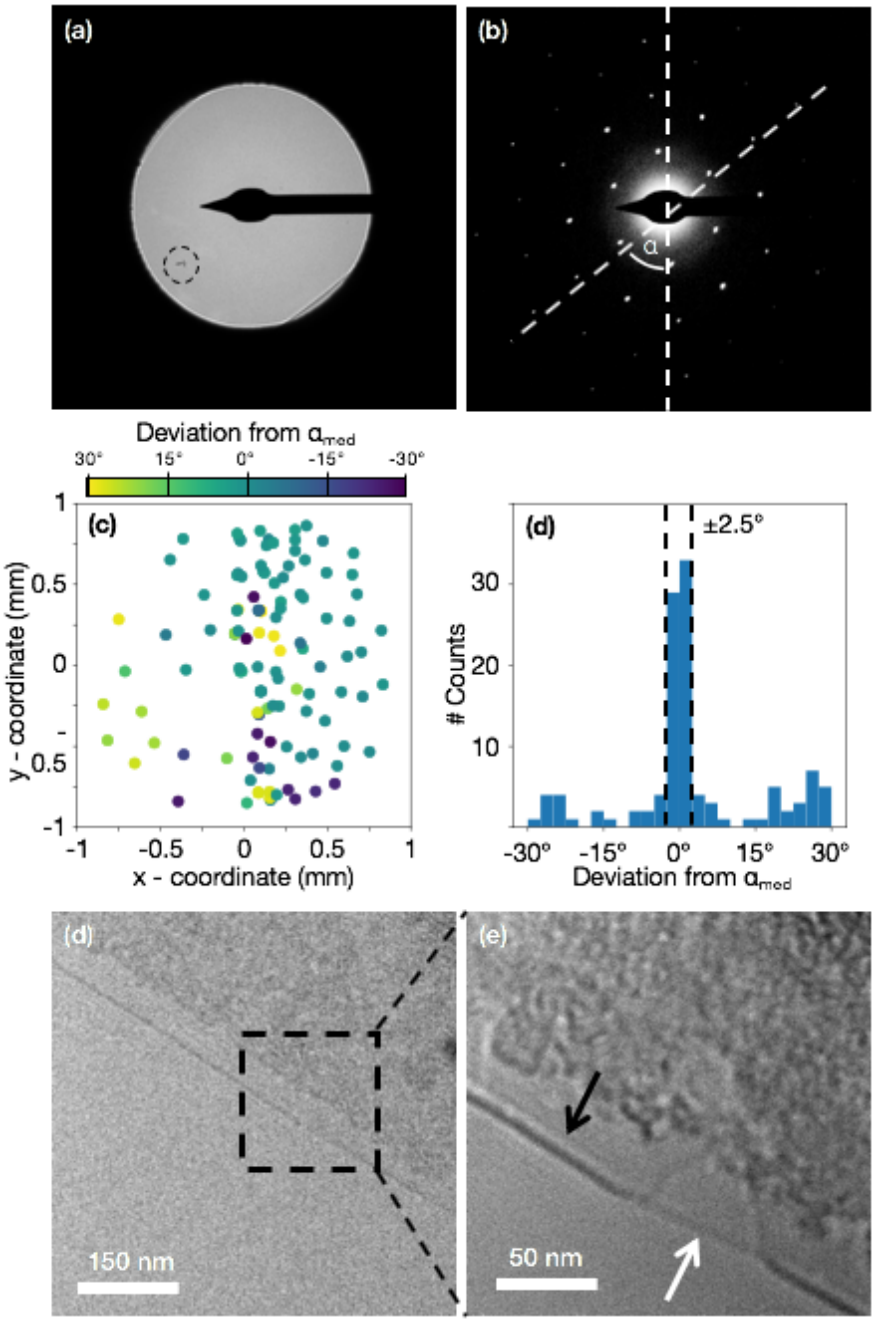

Fig. 5.13 **(a)** BF-TEM images of h-BN. The dotted circle marks a particle on the suspended h-BN, which is otherwise indiscernable. **(b)** DF-TEM image corresponding to (a). α is defined as the angle between the vertical and the closest first order diffraction spot in clockwise direction. **(c)** Scatter map of the rotational deviation from α_{med} (median value of α). **(d)** Distribution of orientation as deviation from α_{med} . (e) & (f) High magnification BF-TEM image of the edge of the h-BN film. Only one fringe is found (black arrow), which confirms the monolayer nature of h-BN. A small dent can be seen (white arrow) caused by folding of the layer. The contrast between single layer edge and folded edge is clearly visible.

The layer number and homogeneity of as-grown h-BN through SEM and AFM. In all SEM images, where h-BN was immediately imaged, the h-BN domains have homogenous contrast, which indicates a constant number of layers across the whole observed region (see for example Fig. 5.1. AFM measurements given in Fig. 5.14) reveal a ~0.4 nm step height for h-BN after transfer onto SiO_2, consistent with mono-layer h-BN thickness. Furthermore the layers are extremely smooth, with only few wrinkles in the central region of the layer. The layers were transferred using direct delamination transfer, which is discussed in Section 5.7.

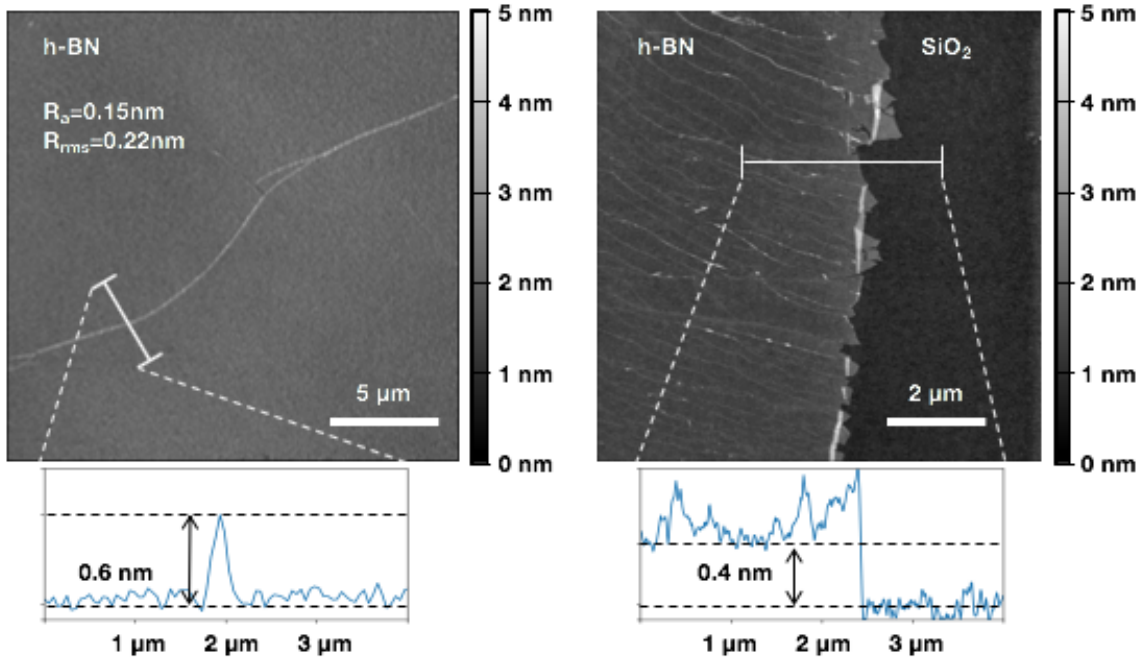

Fig. 5.14 Peak force atomic force microscope (PF-AFM, details in experimental Section) measurement of h-BN transferred onto SiO_2 using direct exfoliation. Prior to the measurements, the sample was heated to 250°C in ambient condition for 5 min. to remove atmospheric adsorbents. **(a)** Height profile of central region of film. The average deviation from mean (R_a) and root mean square average deviation from mean (R_{rms}) are given for the field of view. Due to the extremely low roughness of the surface, the only visible feature is the wrinkle in the central region. **(b)** Step height measurement at the edge of the film. The height is ~0.4nm, which corresponds to monolayer h-BN. More wrinkles are found on the edge, compared with (A), which is potentially induced by the transfer process.

5.7 Delamination Transfer

The SEM images of h-BN flakes shown so far (Figs. 5.1 and 5.11), were taken immediately after growth (reactor to SEM transfer time of around 30 min or less). Fig. 5.15(a) shows a

SEM image recorded 5 hours after removing the sample from the growth chamber, during which time it was stored in ambient environment. Unlike the SEM immediately post-growth of an h-BN domain of similar size and grown under identical conditions (see Fig. 5.1(b) V), where the h-BN appears uniformly darker relative to the Pt substrate, in Fig. 5.15(a) the contrast of the h-BN domain is not uniform. The observed lighter edge region (marked "Decoupled" in Fig. 5.15(a) and contrast change is triggered by the intercalation of oxygen species. This has been previously observed in SEM and for instance LEEM for various systems of 2DLM on weakly interacting substrates [153, 179, 180]. The change takes place at room temperature within the time scale of hours as showns in 5.15(b), similar to G/Pt [153] and G/Cu [152]. It should be noted that the intercalation takes place irrespective of the texture of the underlying Pt substrate.

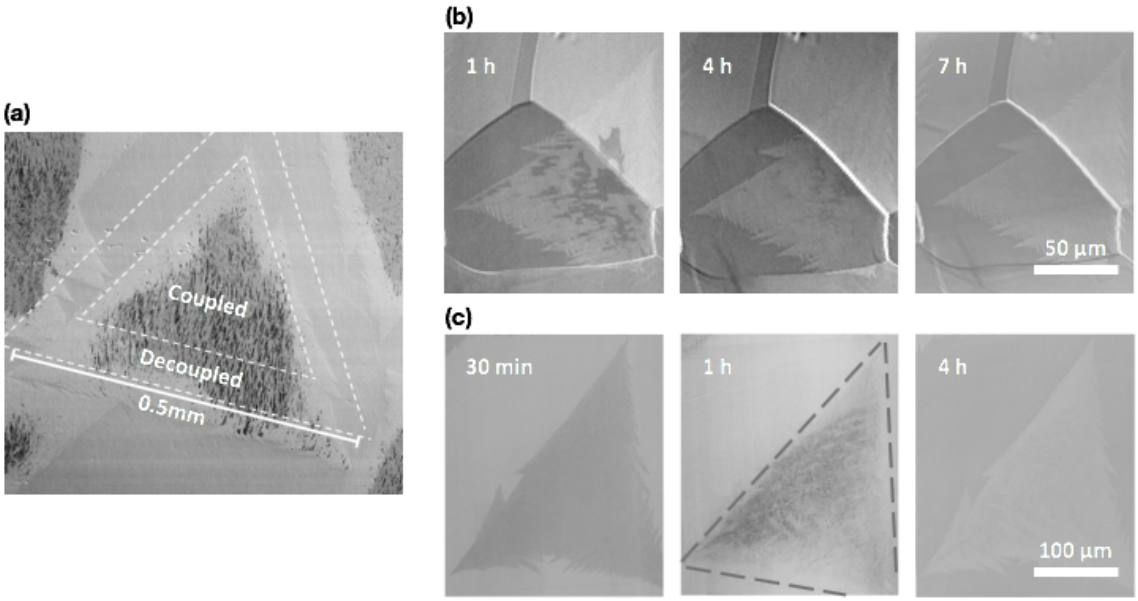

Fig. 5.15 **(a)**SEM image of h-BN on Pt. The image is taken 5 hours after removing the sample from the reactor. The dotted lines mark the outer edge of the domains and the limit between the coupled (black) and decoupled (white) regions. SEM images of the evolution of decoupling of h-BN on Pt for two different samples. Both samples were grown using SG. **(b)** Sample grown at Tgr=1150°C to retain polycrystalline structure of Pt foil. **(c)** Sample grown at Tgr=1200°C after Pt foil recrystallization

The fact that intercalation occurs uniformly from the edges in Fig. 5.15 is a further indication of the quality of the h-BN, as the presence of large defects (such as grain boundaries or pinholes) within a h-BN domain would reveal itself by the onset of local intercalation. In fact, even for domains that have partially merged, intercalation is observed to only proceed from the edges and not from where any potential GB would be located. The SEM image

shown in Fig. 5.16 was taken about 45 min after growth process. The areas with white dotted lines (a) and blue dotted lines (b) are two h-BN islands in the process of merging. (c) marks another island. Due to the difference in size, (c) has already completely decoupled, while islands (a) and (b) are still in the process of decoupling. The red box marks the most likely location for the grain boundary between islands (a) and (b), if any were present. Intercalation is not observed from this location, which indicates the high quality of the h-BN.

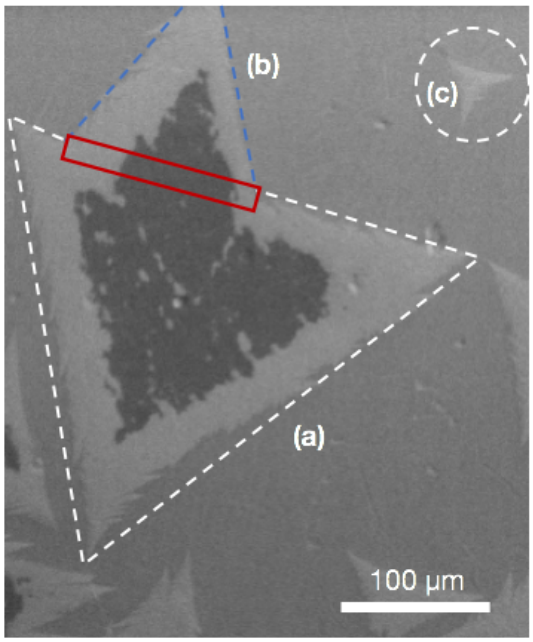

Fig. 5.16 SEM image of sample grown at Tgr=1200°C after Pt foil recrystallization. Image taken about 45 min after growth process. The areas with white dotted lines (a) and blue dotted lines (b) are two h-BN islands in the process of merging. (c) marks another island. Due to the difference in size, (c) has already completely decoupled. Islands (a) & (b) are in the process of decoupling. The red box marks the most likely location for the grain boundary between islands (a) and (b), if any were present. Intercalation is not observed from this location.

The observed intercalation at the interface between h-BN and Pt is an indication of their weak interaction, and a key motivation of our work. Here, a dry transfer approach is introduced to transfer h-BN grown on Pt, as schematically shown in Fig. 5.17(a). A polyvinyl acetate (PVA) stamp is applied to the as-grown h-BN film through drop-casting. The PVA/h-BN stack is then delaminated mechanically (Fig. 5.17(a)I). For monolayer h-BN transfer this stack is then stamped down onto the target substrate (Fig. 5.17(a) IV) and the stamp is removed by dissolution in water. In line with previous experiments on delamination of Gr from Cu [54, 42], an improvement in the ease of transfer is observed by leaving the sample in an ambient environment for an extended period (typically >24h). We relate this effect to the decoupling of the h-BN layer, consistent with the time dependent change in SE contrast of h-BN on Pt (Fig. 5.15 & 5.16).

The given method of dry transfer is not limited to monolayer transfer, but can also be used for the assembly of 2DLM stacks. After picking up the first h-BN layer, the same PVA/h-BN stack can be used for repeated exfoliation of further 2DLM layers. This is performed by simply stamping the stack onto another as-grown 2DLM on its growth substrate (Fig. 5.17(a) II) followed by mechanical delamination (Fig. 5.17a III), which results in the pick-up of an additional 2DLM layer. Such an approach seeks to keep interfacial contamination to a minimum as the second 2DLM layer

is only ever in contact with the growth catalyst and the first 2DLM layer. Through sequential pickup in this way, it is possible to assemble stacks of 2DLMs. This approach is not limited to a specific 2DLMs. However, it requires the adhesion between stamp and 2DLM to be higher than between 2DLM and substrate, highlighting the need for weakly interacting substrates. Sequential pick up of 2DLM is used to fabricate a variety of structures, with Fig. 5.17(b) (left) showing an optical image of multilayer h-BN on SiO_2 obtained by four sequential peelings of CVD mono-layer h-BN. A heterostructure of CVD h-BN and CVD Gr grown on Cu (Gr between h-BN and SiO_2) was also fabricated and an optical image of the result is shown in Fig. 5.17(b) (right). Since the transfer does not involve any modification of the growth catalyst, the Pt foil can be reused for additional growth cycles. In fact, Pt substrates were used for multiple growth runs without noticeable changes to the quality as shown in Fig. 5.18 .

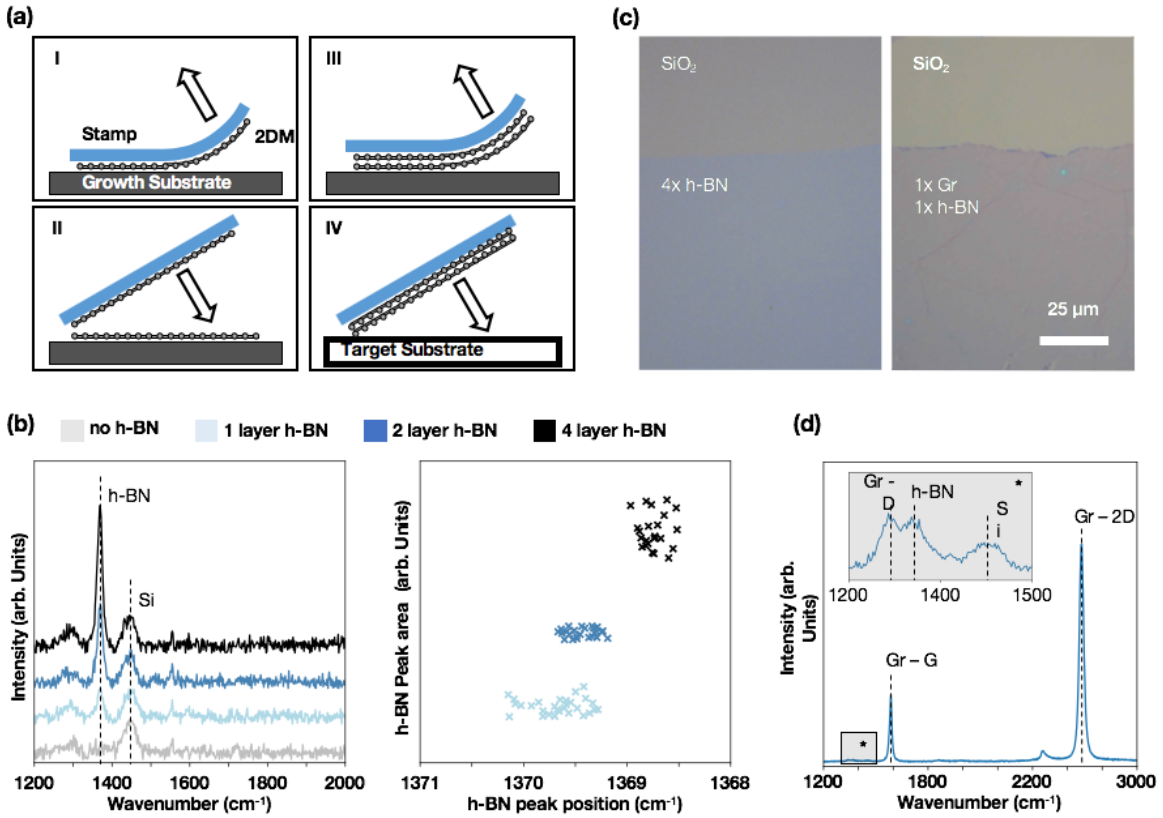

Fig. 5.17 **(a)** Process flow diagram of exfoliation based transfer. The PVA stamp is drop-cast onto the as-grown h-BN, which can then be peeled off and used for sequential exfoliation. After transfer onto the target substrate the stamp is dissolved in water. **(c)** Optical images after transfer onto SiO_2 of 4-layer h-BN and h-BN /Gr (Gr in contact with SiO_2) **(c)** The left graph shows the Raman spectrum of h-BN after transfer onto SiO_2 depending on the layer number. The spectra have been offset for better visibility. Si marks the 3rd order silicon peak at ~1450cm^{-1} [206]. The peak at ~1370cm^{-1} corresponds to h-BN [103]. The right-hand plot presents the peak area after fitting with a Lorentzian curve, against the peak position for multiple measurements of different numbers of h-BN layers. For better visibility, only points between the 1st and 3rd quartile are shown for each sample. The median of the peak position is 1369.7 cm^{-1}, 1369.4 cm^{-1},1368.7 cm^{-1} and the median normalized peak area is 1, 2.24 and 4.03 for monolayer, bilayer and 4-layer h-BN. **(d)** Raman spectrum of h-BN/Gr stack after transfer (Gr in contact with SiO_2). Inset shows magnified region to highlight the h-BN peak

In order to assess the quality of the stacks and to confirm their structure, we employ Raman spectroscopy. The Raman spectrum of h-BN is characterised by the E_{2g} peak at ~1370 cm^{-1}, which due to its non-resonant nature is very weak [103]. However, its peak position and relative intensity can offer an insight into the thickness of the h-BN [103, 193, 239]. Fig. 5.17(c) shows such Raman characterization of multilayer h-BN obtained through repeated exfoliation. The Raman spectra given in Fig. 5.17(c) (left) show an increase in E_{2g} peak area, which is proportional to the number of sequential transfers. This demonstrates that using this

transfer method we are able to pick-up an additional layer during each cycle. Furthermore, it should be noted that the full-width at half maximum (FWHM) of the E_{2g} peak of monolayer h-BN is ~13cm^{-1}, which is comparable to exfoliated h-BN [103]. Since the FWHM is often cited as an indicator of material quality, it highlights the high quality of this CVD h-BN [239]. Fig. 5.17(c) (right) reflects the results of Raman mapping across 100 µm x 100 µm, whereby the quantitative analysis is based on fitting Lorentzian curves to the E_{2g} peak. The linear relationship between peak area and layer number is maintained across the mapped region, indicating the quality of the transfer method. Furthermore, in agreement with previous studies [193], we observe a slight red-shift in the E_{2g} peak position with increasing layer number from 1369.7cm^{-1} for monolayer h-BN to 1368.7cm^{-1} for four-layer h-BN, which indicates a clean interface as this shift relates to the interaction between layers [103, 193, 239]. The Raman characterization of h-BN/Gr heterostructures is more challenging, due to the large difference in signal intensity of Gr and h-BN. The Raman spectrum of an all CVD heterostructure is shown in Fig. 5.17d. Due to the proximity of peaks, minor imperfections in the Gr will result in the Gr D-peak (1350cm^{-1}) [240] overlapping with and potentially swamping the h-BN peak (1370cm^{-1}). In Fig. 5.17(d) the Gr D-peak/G-peak ratio is less than 0.025, still the h-BN peak is only just visible in the magnification of the plot (inset), demonstrating that Gr can be directly delaminated from the growth catalyst using h-BN.

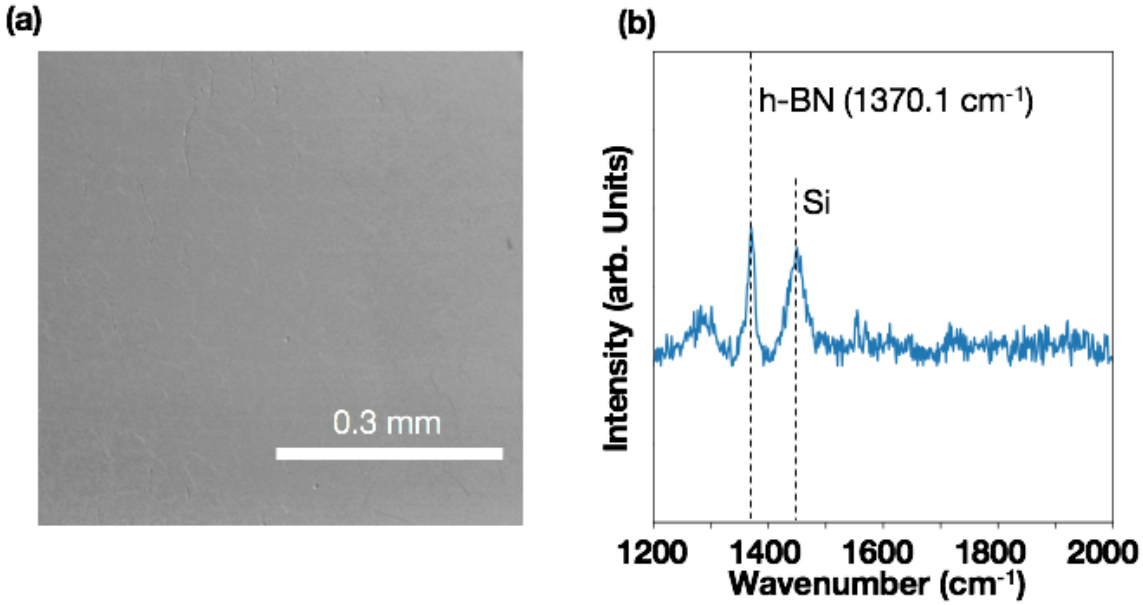

Fig. 5.18 **(a)** Growth of h-BN film on Pt foil. Lack of contrast due to continuous film of h-BN. Image is taken of h-BN grown on Pt foil, which has been used for a previous growth/transfer cycle. During first run a continuous film of h-BN was grown and transferred off using the methods described in the experimental methods Section. Before regrowth, the only catalyst preparation step consists of sonicating the sample in water, to remove potential residues of PVA. The second run was performed using a SG process using the conditions: T_{gr} = 1175°C, t_{sd}= 10min to achieve a continuous layer of h-BN. **(b)** Raman spectrum of sample from image (a). The sample regrown on a previously used Pt foil was transferred using peeling transfer onto SiO_2 (300 nm)/Si wafer. The h-BN/ Si peak intensity ratio (~1, compare with Fig. 6) and peak position (1370.1 cm^{-1}) indicate monolayer h-BN. The h-BN is of high quality as shown by the FWHM of around 13.5 cm^{-1}, which compares well to the FWHM of monolayer bulk exfoliated h-BN [193].

5.8 Integration of CVD h-BN in Gr/h-BN heterostructures

The fabrication of high quality Gr/h-BN heterostructures has been a significant challenge even when relying entirely on exfoliation [3, 12, 220]. Thus, to demonstrate the feasibility of this approach and to narrow-down the parameter space for device processing, the focus here is on just the insertion of a CVD h-BN layer via a model structure consisting of monolayer CVD-h-BN as a capping layer on monolayer exfoliated (exf) Gr. Fig. 5.19(a) shows an optical image of the assembled stack. Using a PVA/CVD h-BN stack, which is obtained by delaminating an as grown h-BN layer from Pt, exf-Gr from a SiO_2/Si wafer. The h-BN is not observed optically as it uniformly covers the sample. It becomes apparent in Fig. 5.19(a) II and III, which presents the result of a peak force (PF-)AFM measurement of the transition

region from CVD h-BN/exf-Gr to CVD h-BN only. The measured step height for the exf-Gr layer is ~0.4 nm and the surface is atomically smooth, which are indications of an interface without significant amounts of trapped residues.

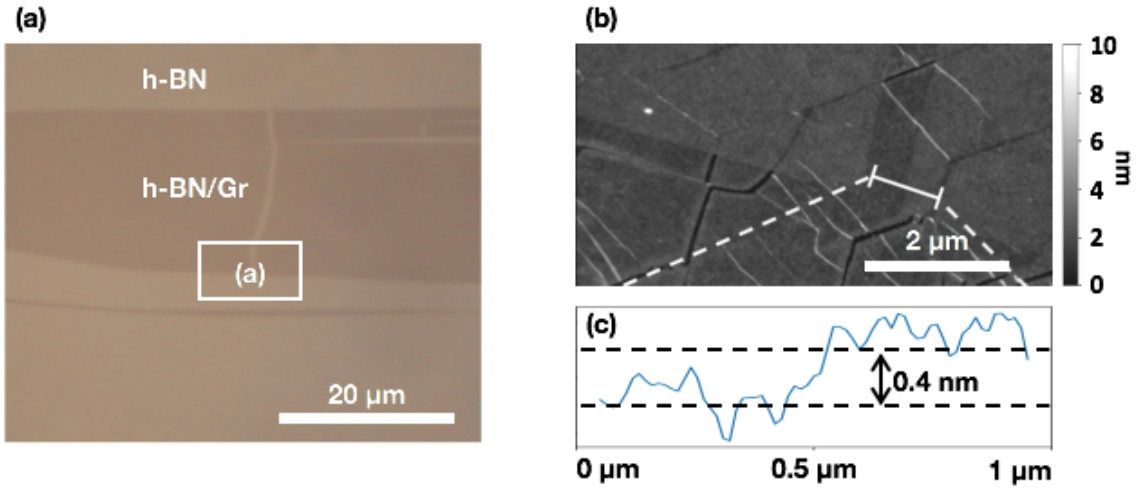

Fig. 5.19 **(a)** Optical image of monolayer CVD h-BN on exfoliated Gr transferred onto a 90 nm SiO_2/Si wafer (Gr between h-BN and SiO_2). h-BN is not discernible as it uniformly covers the sample. **(b)** Peak force atomic force microscope (PF-AFM, details in experimental Section) of area marked in (a). **(c)** Profile of line marked in (b). Step height of transition from h-BN only to h-BN/Gr region is about ~0.4 nm, as expected for single layer Gr, indicating a clean interface.

Fig. 5.20 shows the result of the Raman analysis. The Gr G peak and 2D peak position of each spectrum is plotted with the strain and doping axis for reference [189]. The colour of each point indicates the FWHM of the Gr 2D peak. The median of the Gr G peak and 2D peak positions are 1584.7 cm^{-1} and 2684.6 cm^{-1} respectively, compared to 1581.6 cm^{-1} and 2676.9 cm^{-1} for suspended exf-Gr [189]. The median FWHM of the Gr 2D peak is 26.2 cm^{-1}, which is similar to previous studies, where exf-h-BN/exf-Gr on SiO_2 has a 2D peak FWHM of about 25 cm^{-1} [192]. The measurement points are aligned along the strain axis, indicating that the sample is undoped, but is affected by strain.

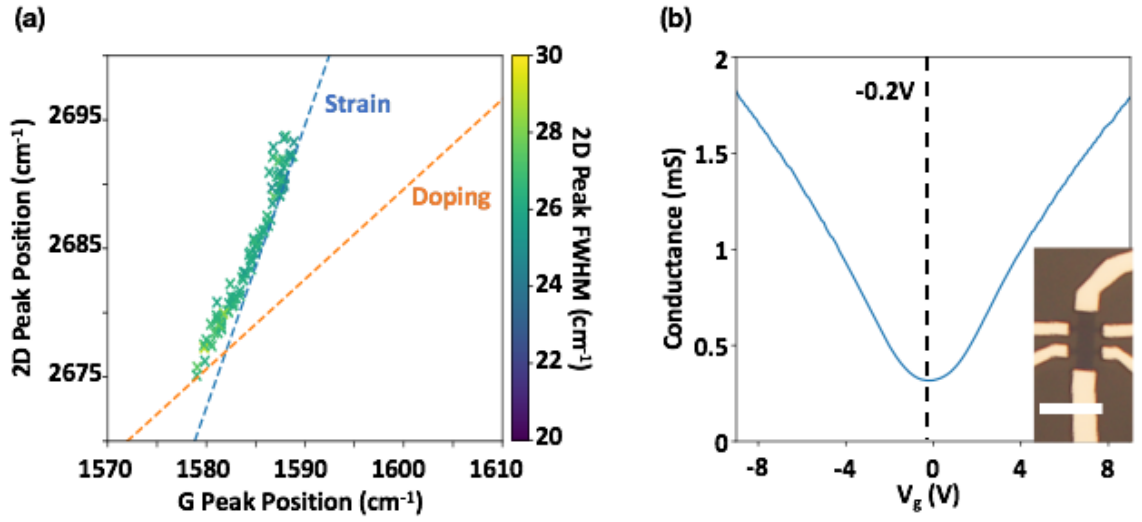

Fig. 5.20 **(a)** Peak position of the G- and 2D-peak of Gr measured by Raman spectroscopy. Colour of cross relates to FWHM of the 2D peak (See associated colour bar). The dotted blue line is the strain axis (slope 2.2), dotted orange line the doping axis (slope 0.7) and the charge neutrality point is (1582 cm -1, 2677 cm^{-1}) [189]. **(b)** Transfer curve obtained via 4-terminal measurement. The position of the Dirac point is marked. An optical image of the Hall bar measured is shown in the inset. The scale bar indicates 10 µm.

The sheet conductivity of a representative CVD h-BN/exf-Gr field effect transistor (FET) device (where the Si substrate acts a back gate) is shown in Fig. 5.20(b). The position of the charge neutrality point (CNP), at -0.2V, confirms that the Gr is highly intrinsic. The devices are shaped as Hall bars, allowing independent measurement of gate-dependent conductivity and charge carrier concentration (by applying an out of plane magnetic field). The Hall mobility (μ_H) is then extracted assuming a Drude model for conductivity, leading to a maximum mobility of μ_H = 7200 $cm^2V^{-1}s^{-1}$ at room temperature. The charge carrier density without the application of a back-gate voltage for this device is n_0 = 4.8 x $10^{10}cm^{-2}$, confirming the low doping level indicated by the Raman analysis. We note that such low doping is achieved without the need for any high temperature annealing to remove residuals post-transfer. We repeated the analysis for two additional independent devices and find the values reproducible, with μ_H = 7950 $cm^2V^{-1}s^{-1}$, n_0 = 2.5 x $10^{10}cm^{-2}$ and μ_H = 7270 $cm^2V^{-1}s^{-1}$, n_0 = 1.15 x $10^{11}cm^{-2}$ for each of the respective devices. The performance of the given devices underscores the cleanliness of the Gr/h-BN interface and is, to the best of our knowledge, the highest for heterostructures using CVD h-BN. Further improvements in mobility should be achievable by introducing an additional h-BN layer underneath the Gr to screen the roughness and charged impurities of the SiO_2 [3]. The given

stack serves as a first demonstrator for our proposed approach of growing h-BN via CVD and integrating it into heterostructure devices with the goal to replace exfoliated h-BN.

5.9 Conclusion

Improving current 2DLM integration strategies requires careful consideration of the growth catalyst. In this Chapter, it has been demonstrated that Pt is a suitable weakly interacting catalyst that enables not only h-BN growth with mono-layer control and crystal sizes in excess of 0.5 mm, but also direct transfer by delaminating as-grown layers to achieve clean processing. The in-situ experiments show that h-BN grows isothermally on Pt within the given CVD parameter space, driven by a local B and N supersaturation at the surface, and that when the precursor flux is removed the h-BN layer starts to dissolve. The initial B dissolution and decoration of Pt GBs leads to significantly accelerated Pt crystallisation. These insights enbaled the design of an integrated CVD growth process, that is referred to as SSG, which based on two coupled borazine exposures not only transforms poly-crystalline Pt foils into a dominant (111) orientation but enables independent control of h-BN nucleation and domain expansion, i.e. the CVD of highly crystalline mono-layer h-BN. Delamination transfer method is demonstrated that makes use of the weak Pt/h-BN interaction, to directly delaminate the as-grown films from the catalyst. Thereby the catalyst is preserved for regrowth and it is possible to achieve a clean transfer process. This approach allows the precise control of the thickness of the h-BN layer, something that has not been achieved for exfoliated h-BN, but is critical to many applications.

Chapter 6

Conclusion and Outlook

Developing reliable and industry scale methods for the fabrication of 2DLMs is the key challenge to creating commercially relevant applications based on this family of materials. So far a compromise had always to be made between the scalability of the material production and its quality. The main problem hereby has not been the lack of growth methods for high quality material, but strategies to integrate these into devices, whether on their own or as part of a van der Waals heterostructure.

Two approaches are possible to overcome this challenge. The most straightforward one is to continue the effort on improving transfer for existing 2DLM/catalyst system. This work has led to the development of the Lift-Off Transfer (LOT) method, that has been described in detail in Chapter 4. Based on a detailed understanding of the interaction of 2DLM and its underlying substrate, it has been possible to develop a general process rationale transfer. Transfer using LOT lead to a significant improvement in device performance over standard transfer methods. Furthermore, this work lead to important insights regarding the limitations of transfers, specifically ones that involve catalyst treatment with a chemical solution.

Instead of tuning transfer processes for a given combination of 2DLM and growth catalyst, the other approach has been to identify a combination that can best accomodate the only known method of transfer that leads to truly high performance devices, which is mechanical delamination. The key requirement hereby is the growth of high quality h-BN on a weakly interacting substrate. As discussed in Chapter 5, not only was the growth of h-BN with domain sizes exceeding 0.5 mm achieved, but more importantly an associated transfer process was developed that enables transfer through delamination. It was shown how these individual monolayers of h-BN could be combined into stacks with atomic precision, or used to pick up

layers of other 2DLM such as Gr directly from the growth catalyst. The devices proved that the Gr remains protected and highly intrinsic throughout the entire fabrication process.

The work described in this thesis, especially regarding the delamination transfer of high quality h-BN and the assembly of vertical 2DLM stacks, will have significant impact on the scalable manufacture of 2DLMs. This method demonstrates the feasibility of producing heterostructures using only fast, scalable and industry compatible methods. The immediate next steps will be the automation of the processing steps to improve the process yield, with the final goal of large scale implementation and device integration. The application of the processes described in this thesis will finally enable a large variety of 2DLM based devices, which so far have been hindered by the lack of sufficiently advanced methods of scalable production. These include for example a new generation of sensors for the fast and sensitive detection of biomarkers, which will the focus of the next project.

List of Figures

References

[1] K. S. Novoselov, A. K. Geim, S. V. Morozov, D. Jiang, Y. Zhang, S. V. Dubonos, I. V. Grigorieva, and A. A. Firsov, "Electric field effect in atomically thin carbon films," *Science*, vol. 306, no. 5696, pp. 666–669, 2004.

[2] Y. Zhang, Y.-W. Tan, H. L. Stormer, and P. Kim, "Experimental observation of the quantum Hall effect and Berry's phase in graphene," *Nature*, vol. 438, no. 7065, p. 201, 2005.

[3] C. R. Dean, A. F. Young, I. Meric, C. Lee, L. Wang, S. Sorgenfrei, K. Watanabe, T. Taniguchi, P. Kim, K. L. Shepard, and J. Hone, "Boron nitride substrates for high-quality graphene electronics," *Nature Nanotechnology*, vol. 5, no. 10, pp. 722–726, 2010.

[4] L. Britnell, R. V. Gorbachev, R. Jalil, B. D. Belle, F. Schedin, A. Mishchenko, T. Georgiou, M. I. Katsnelson, L. Eaves, S. V. Morozov, N. M. R. Peres, J. Leist, A. K. Geim, K. S. Novoselov, and L. A. Ponomarenko, "Field-Effect Tunneling Transistor Based on Vertical Graphene Heterostructures," *Science*, vol. 335, no. 6071, pp. 947–950, 2012.

[5] H. Yang, J. Heo, S. Park, H. J. Song, D. H. Seo, K.-E. Byun, P. Kim, I. Yoo, H.-J. Chung, and K. Kim, "Graphene Barristor, a Triode Device with a Gate-Controlled Schottky Barrier," *Science*, vol. 336, no. 6085, pp. 1140–1143, 2012.

[6] V. E. Calado, S. Goswami, G. Nanda, M. Diez, A. R. Akhmerov, K. Watanabe, T. Taniguchi, M. T. Klapwijk, and K. L. M. Vandersypen, "Ballistic Josephson junctions in edge-contacted graphene," *Nature Nanotechnology*, vol. 10, no. 9, pp. 761–764, 2015.

[7] C. Liu, X. Yan, X. Song, S. Ding, D. W. Zhang, and P. Zhou, "A semi-floating gate memory based on van der Waals heterostructures for quasi-non-volatile applications," *Nature Nanotechnology*, vol. 13, no. 5, p. 1, 2018.

[8] Y. Cao, V. Fatemi, S. Fang, K. Watanabe, T. Taniguchi, E. Kaxiras, and P. Jarillo-Herrero, "Unconventional superconductivity in magic-angle graphene superlattices," *Nature*, vol. 556, p. 43, 2018.

[9] T. Georgiou, R. Jalil, B. D. Belle, L. Britnell, R. V. Gorbachev, S. V. Morozov, Y.-J. Kim, A. Gholinia, S. J. Haigh, O. Makarovsky, L. Eaves, L. A. Ponomarenko, A. K. Geim, K. S. Novoselov, and A. Mishchenko, "Vertical field-effect transistor based

on graphene-WS2 heterostructures for flexible and transparent electronics," *Nature Nanotechnology*, vol. 8, no. 2, pp. 100–103, 2013.

[10] F. Withers, O. Del Pozo-Zamudio, A. Mishchenko, A. P. Rooney, A. Gholinia, K. Watanabe, T. Taniguchi, S. J. Haigh, A. K. Geim, A. I. Tartakovskii, and K. S. Novoselov, "Light-emitting diodes by band-structure engineering in van der Waals heterostructures," *Nature Materials*, vol. 14, no. 3, pp. 301–306, 2015.

[11] P. Blake, E. W. Hill, A. H. C. Neto, K. S. Novoselov, D. Jiang, R. Yang, T. J. Booth, and A. K. Geim, "Making graphene visible," *Applied Physics Letters*, vol. 91, no. 6, 2007.

[12] F. Pizzocchero, L. Gammelgaard, B. S. Jessen, J. M. Caridad, L. Wang, J. Hone, P. Bøggild, and T. J. Booth, "The hot pick-up technique for batch assembly of van der Waals heterostructures," *Nature Communications*, vol. 7, 2016.

[13] S. Masubuchi, M. Morimoto, S. Morikawa, M. Onodera, Y. Asakawa, K. Watanabe, T. Taniguchi, and T. Machida, "Autonomous robotic searching and assembly of two-dimensional crystals to build van der Waals superlattices," *Nature Communications*, vol. 9, no. 1, p. 1413, 2018.

[14] K. S. Novoselov, V. I. Falko, L. Colombo, P. R. Gellert, M. G. Schwab, and K. Kim, "A roadmap for graphene," *Nature*, vol. 490, p. 192, 2012.

[15] Y. Hernandez, V. Nicolosi, M. Lotya, F. M. Blighe, Z. Sun, S. De, I. T. McGovern, B. Holland, M. Byrne, and Y. K. Gun'Ko, "High-yield production of graphene by liquid-phase exfoliation of graphite," *Nature nanotechnology*, vol. 3, no. 9, p. 563, 2008.

[16] V. Nicolosi, M. Chhowalla, M. G. Kanatzidis, M. S. Strano, and J. N. Coleman, "Liquid Exfoliation of Layered Materials," *Science*, vol. 340, no. 6139, p. 1226419, 2013.

[17] S. Hofmann, P. Braeuninger-Weimer, and R. S. Weatherup, "CVD-enabled graphene manufacture and technology," *The Journal of Physical Chemistry Letters*, vol. 6, no. 14, pp. 2714–2721, 2015.

[18] M. Segal, "Selling graphene by the ton," *Nature Nanotechnology*, vol. 4, p. 612, 2009.

[19] F. Torrisi, T. Hasan, W. Wu, Z. Sun, A. Lombardo, T. S. Kulmala, G.-W. Hsieh, S. Jung, F. Bonaccorso, P. J. Paul, D. Chu, and A. C. Ferrari, "Inkjet-Printed Graphene Electronics," *ACS Nano*, vol. 6, no. 4, pp. 2992–3006, 2012.

[20] M. L. Hitchman and A. C. Jones, *Chemical vapor deposition: Precursors, Processes, Applications*. RSC Publishing, 2009.

[21] J. Kong, A. M. Cassell, and H. Dai, "Chemical vapor deposition of methane for single-walled carbon nanotubes," *Chemical Physics Letters*, vol. 292, no. 4, pp. 567–574, 1998.

[22] C. H. Lee, M. Xie, V. Kayastha, J. Wang, and Y. K. Yap, "Patterned growth of boron nitride nanotubes by catalytic chemical vapor deposition," *Chemistry of Materials*, vol. 22, no. 5, pp. 1782–1787, 2010.

[23] J. Westwater, D. P. Gosain, S. Tomiya, S. Usui, and H. Ruda, "Growth of silicon nanowires via gold/silane vapor - liquid - solid reaction," *Journal of Vacuum Science & Technology B: Microelectronics and Nanometer Structures Processing, Measurement, and Phenomena*, vol. 15, no. 3, pp. 554–557, 1997.

[24] K. S. Kim, Y. Zhao, H. Jang, S. Y. Lee, J. M. Kim, K. S. Kim, J.-H. Ahn, P. Kim, J.-Y. Choi, and B. H. Hong, "Large-scale pattern growth of graphene films for stretchable transparent electrodes," *Nature*, vol. 457, no. 7230, pp. 706–710, 2009.

[25] X. S. Li, W. W. Cai, J. H. An, S. Kim, J. Nah, D. X. Yang, R. Piner, A. Velamakanni, I. Jung, E. Tutuc, S. K. Banerjee, L. Colombo, and R. S. Ruoff, "Large-area synthesis of high-quality and uniform graphene films on copper foils," *Science*, vol. 324, no. 5932, pp. 1312–1314, 2009.

[26] Y. Shi, C. Hamsen, X. Jia, K. K. Kim, A. Reina, M. Hofmann, A. L. Hsu, K. Zhang, H. Li, and Z.-Y. Juang, "Synthesis of few-layer hexagonal boron nitride thin film by chemical vapor deposition," *Nano letters*, vol. 10, no. 10, pp. 4134–4139, 2010.

[27] A. Pakdel, Y. Bando, and D. Golberg, "Nano boron nitride flatland," *Chemical Society Reviews*, vol. 43, no. 3, pp. 934–959, 2014.

[28] S. M. Eichfeld, L. Hossain, Y.-C. Lin, A. F. Piasecki, B. Kupp, A. G. Birdwell, R. A. Burke, N. Lu, X. Peng, and J. Li, "Highly Scalable, Atomically Thin WSe2 Grown via Metal - Organic Chemical Vapor Deposition," *ACS nano*, vol. 9, no. 2, pp. 2080–2087, 2015.

[29] Y. Shi, H. Li, and L.-J. Li, "Recent advances in controlled synthesis of two-dimensional transition metal dichalcogenides via vapour deposition techniques," *Chemical Society Reviews*, vol. 44, no. 9, pp. 2744–2756, 2015.

[30] A.-R. Jang, S. Hong, C. Hyun, S. I. Yoon, G. Kim, H. Y. Jeong, T. J. Shin, S. O. Park, K. Wong, S. K. Kwak, N. Park, K. Yu, E. Choi, A. Mishchenko, F. Withers, K. S. Novoselov, H. Lim, and H. S. Shin, "Wafer-Scale and Wrinkle-Free Epitaxial Growth of Single-Orientated Multilayer Hexagonal Boron Nitride on Sapphire," *Nano Letters*, vol. 16, no. 5, pp. 3360–3366, 2016.

[31] H. Wang and G. Yu, "Direct CVD Graphene Growth on Semiconductors and Dielectrics for Transfer-Free Device Fabrication," *Advanced Materials*, vol. 28, no. 25, pp. 4956–4975, 2016.

[32] D. V. Badami, "X-ray studies of graphite formed by decomposing silicon carbide," *Carbon*, vol. 3, no. 1, pp. 53–57, 1965.

[33] W. Norimatsu and M. Kusunoki, "Epitaxial graphene on SiC {0001}: advances and perspectives," *Physical Chemistry Chemical Physics*, vol. 16, no. 8, pp. 3501–3511, 2014.

[34] C. Berger, Z. M. Song, X. B. Li, X. S. Wu, N. Brown, C. Naud, D. Mayou, T. B. Li, J. Hass, A. N. Marchenkov, E. H. Conrad, P. N. First, and W. A. de Heer, "Electronic confinement and coherence in patterned epitaxial graphene," *Science*, vol. 312, no. 5777, pp. 1191–1196, 2006.

[35] H. C. Lee, W.-W. Liu, S.-P. Chai, A. R. Mohamed, A. Aziz, C.-S. Khe, N. M. S. Hidayah, and U. Hashim, "Review of the synthesis, transfer, characterization and growth mechanisms of single and multilayer graphene," *RSC Advances*, vol. 7, no. 26, pp. 15644–15693, 2017.

[36] C. Tan, X. Cao, X.-J. Wu, Q. He, J. Yang, X. Zhang, J. Chen, W. Zhao, S. Han, and G.-H. Nam, "Recent Advances in Ultrathin Two-Dimensional Nanomaterials," *Chemical Reviews*, 2017.

[37] J. Hackley, D. Ali, J. DiPasquale, J. D. Demaree, and C. J. K. Richardson, "Graphitic carbon growth on Si (111) using solid source molecular beam epitaxy," *Applied Physics Letters*, vol. 95, no. 13, p. 133114, 2009.

[38] M. Zheng, K. Takei, B. Hsia, H. Fang, X. Zhang, N. Ferralis, H. Ko, Y.-L. Chueh, Y. Zhang, and R. Maboudian, "Metal-catalyzed crystallization of amorphous carbon to graphene," *Applied Physics Letters*, vol. 96, no. 6, p. 63110, 2010.

[39] Z. Sun, Z. Yan, J. Yao, E. Beitler, Y. Zhu, and J. M. Tour, "Growth of graphene from solid carbon sources," *Nature*, vol. 468, no. 7323, pp. 549–552, 2010.

[40] S. Suzuki, Y. Ogawa, S. Wang, and K. Kumakura, "Initial stage of hexagonal boron nitride growth in diffusion and precipitation method," *Japanese Journal of Applied Physics*, vol. 56, no. 6S1, p. 06GE06, 2017.

[41] S. Bae, H. Kim, Y. Lee, X. F. Xu, J. S. Park, Y. Zheng, J. Balakrishnan, T. Lei, H. R. Kim, Y. I. Song, Y. J. Kim, K. S. Kim, B. Ozyilmaz, J. H. Ahn, B. H. Hong, and S. Iijima, "Roll-to-roll production of 30-inch graphene films for transparent electrodes," *Nature Nanotechnology*, vol. 5, no. 8, pp. 574–578, 2010.

[42] L. Banszerus, M. Schmitz, S. Engels, J. Dauber, M. Oellers, F. Haupt, K. Watanabe, T. Taniguchi, B. Beschoten, and C. Stampfer, "Ultrahigh-mobility graphene devices from chemical vapor deposition on reusable copper," *Science Advances*, vol. 1, no. 6, p. e1500222, 2015.

[43] K.-B. Kim, C.-M. Lee, and J. Choi, "Catalyst-free direct growth of triangular nanographene on all substrates," *The Journal of Physical Chemistry C*, vol. 115, no. 30, pp. 14488–14493, 2011.

[44] M. A. Fanton, J. A. Robinson, C. Puls, Y. Liu, M. J. Hollander, B. E. Weiland, M. LaBella, K. Trumbull, R. Kasarda, and C. Howsare, "Characterization of graphene films and transistors grown on sapphire by metal-free chemical vapor deposition," *Acs Nano*, vol. 5, no. 10, pp. 8062–8069, 2011.

[45] J. Sun, N. Lindvall, M. T. Cole, K. B. K. Teo, A. Yurgens, J. Sun, N. Lindvall, M. T. Cole, and K. B. K. Teo, "Large-area uniform graphene-like thin films grown by chemical vapor deposition directly on silicon nitride Large-area uniform graphene-like

thin films grown by chemical vapor deposition directly on silicon nitride," vol. 252107, no. 98, 2011.

[46] G. Kim, A.-R. Jang, H. Y. Jeong, Z. Lee, D. J. Kang, and H. S. Shin, "Growth of High-Crystalline, Single-Layer Hexagonal Boron Nitride on Recyclable Platinum Foil," *Nano Letters*, vol. 13, no. 4, pp. 1834–1839, 2013.

[47] S. Caneva, R. S. Weatherup, B. Bayer, B. Brennan, S. J. Spencer, K. Mingard, A. Cabrero-Vilatela, C. Baehtz, A. J. Pollard, and S. Hofmann, "Nucleation control for large, single crystalline domains of monolayer hexagonal boron nitride via Si-doped Fe catalysts," *Nano Letters*, vol. 15, no. 3, pp. 1867–1875, 2015.

[48] A. Cabrero-Vilatela, R. S. Weatherup, P. Braeuninger-Weimer, S. Caneva, and S. Hofmann, "Towards a general growth model for graphene CVD on transition metal catalysts," *Nanoscale*, vol. 8, no. 4, pp. 2149–2158, 2016.

[49] B. Dlubak, M.-B. Martin, R. S. Weatherup, H. Yang, C. Deranlot, R. Blume, R. Schloegl, A. Fert, A. Anane, S. Hofmann, P. Seneor, and J. Robertson, "Graphene-Passivated Nickel as an Oxidation-Resistant Electrode for Spintronics," *ACS Nano*, vol. 6, no. 12, pp. 10930–10934, 2012.

[50] M. Piquemal-Banci, R. Galceran, S. Caneva, M.-B. Martin, R. S. Weatherup, P. R. Kidambi, K. Bouzehouane, S. Xavier, A. Anane, F. Petroff, A. Fert, J. Robertson, S. Hofmann, B. Dlubak, and P. Seneor, "Magnetic tunnel junctions with monolayer hexagonal boron nitride tunnel barriers," *Applied Physics Letters*, vol. 108, no. 10, p. 102404, 2016.

[51] X. L. Liang, B. A. Sperling, I. Calizo, G. J. Cheng, C. A. Hacker, Q. Zhang, Y. Obeng, K. Yan, H. L. Peng, Q. L. Li, X. X. Zhu, H. Yuan, A. R. H. Walker, Z. F. Liu, L. M. Peng, and C. A. Richter, "Toward Clean and Crackless Transfer of Graphene," *Acs Nano*, vol. 5, no. 11, pp. 9144–9153, 2011.

[52] Y. Wang, Y. Zheng, X. Xu, E. Dubuisson, Q. Bao, J. Lu, and K. P. Loh, "Electrochemical delamination of CVD-grown graphene film: toward the recyclable use of copper catalyst," *ACS Nano*, vol. 5, no. 12, pp. 9927–9933, 2011.

[53] F. Pizzocchero, B. S. Jessen, P. R. Whelan, N. Kostesha, S. Lee, J. D. Buron, I. Petrushina, M. B. Larsen, P. Greenwood, W. J. Cha, K. Teo, P. U. Jepsen, J. Hone, P. Bøggild, and T. J. Booth, "Non-destructive electrochemical graphene transfer from reusable thin-film catalysts," *Carbon*, vol. 85, pp. 397–405, 2015.

[54] P. R. Whelan, B. S. Jessen, R. Wang, B. Luo, A. C. Stoot, D. M. A. Mackenzie, P. Braeuninger-Weimer, A. Jouvray, L. Prager, and L. Camilli, "Raman spectral indicators of catalyst decoupling for transfer of CVD grown 2D materials," *Carbon*, vol. 117, pp. 75–81, 2017.

[55] X. Du, I. Skachko, A. Barker, and E. Y. Andrei, "Approaching ballistic transport in suspended graphene," *Nature Nanotechnology*, vol. 3, no. 8, pp. 491–495, 2008.

[56] L. Banszerus, M. Schmitz, S. Engels, M. Goldsche, K. Watanabe, T. Taniguchi, B. Beschoten, and C. Stampfer, "Ballistic transport exceeding 28 μm in CVD grown graphene," *Nano Letters*, vol. 16, no. 2, pp. 1387–1391, 2016.

[57] C. Lee, X. D. Wei, J. W. Kysar, and J. Hone, "Measurement of the elastic properties and intrinsic strength of monolayer graphene," *Science*, vol. 321, no. 5887, pp. 385–388, 2008.

[58] A. A. Balandin, S. Ghosh, W. Z. Bao, I. Calizo, D. Teweldebrhan, F. Miao, and C. N. Lau, "Superior thermal conductivity of single-layer graphene," *Nano Letters*, vol. 8, no. 3, pp. 902–907, 2008.

[59] J. H. Seol, I. Jo, A. L. Moore, L. Lindsay, Z. H. Aitken, M. T. Pettes, X. S. Li, Z. Yao, R. Huang, D. Broido, N. Mingo, R. S. Ruoff, and L. Shi, "Two-Dimensional Phonon Transport in Supported Graphene," *Science*, vol. 328, no. 5975, pp. 213–216, 2010.

[60] K. J. Jeon, Z. Lee, E. Pollak, L. Moreschini, A. Bostwick, C. M. Park, R. Mendelsberg, V. Radmilovic, R. Kostecki, T. J. Richardson, and E. Rotenberg, "Fluorographene: A Wide Bandgap Semiconductor with Ultraviolet Luminescence," *Acs Nano*, vol. 5, no. 2, pp. 1042–1046, 2011.

[61] D. C. Elias, R. R. Nair, T. M. G. Mohiuddin, S. V. Morozov, P. Blake, M. P. Halsall, A. C. Ferrari, D. W. Boukhvalov, M. I. Katsnelson, and A. K. Geim, "Control of graphene's properties by reversible hydrogenation: evidence for graphane," *Science*, vol. 323, no. 5914, pp. 610–613, 2009.

[62] W. S. Hummers and R. E. Offeman, "Preparation of Graphitic Oxide," *Journal of the American Chemical Society*, vol. 80, no. 6, p. 1339, 1958.

[63] D. R. Dreyer, S. Park, C. W. Bielawski, and R. S. Ruoff, "The chemistry of graphene oxide," *Chemical Society Reviews*, vol. 39, no. 1, pp. 228–240, 2010.

[64] J. M. Garcia, U. Wurstbauer, A. Levy, L. N. Pfeiffer, A. Pinczuk, A. S. Plaut, L. Wang, C. R. Dean, R. Buizza, A. M. Van Der Zande, J. Hone, K. Watanabe, and T. Taniguchi, "Graphene growth on h-BN by molecular beam epitaxy," *Solid State Communications*, vol. 152, no. 12, pp. 975–978, 2012.

[65] L. H. Li, J. Cervenka, K. Watanabe, T. Taniguchi, and Y. Chen, "Strong oxidation resistance of atomically thin boron nitride nanosheets," *ACS nano*, vol. 8, no. 2, pp. 1457–1462, 2014.

[66] F. Karlický, K. Kumara Ramanatha Datta, M. Otyepka, and R. Zbořil, "Halogenated Graphenes: Rapidly Growing Family of Graphene Derivatives," *Acs Nano*, vol. 7, no. 8, pp. 6434–6464, 2013.

[67] A. K. Geim and I. V. Grigorieva, "Van der Waals heterostructures," *Nature*, vol. 499, no. 7459, pp. 419–425, 2013.

[68] M. Chhowalla, H. S. Shin, G. Eda, L. J. Li, K. P. Loh, and H. Zhang, "The chemistry of two-dimensional layered transition metal dichalcogenide nanosheets," *Nature Chemistry*, vol. 5, no. 4, pp. 263–275, 2013.

[69] K. F. Mak, C. Lee, J. Hone, J. Shan, and T. F. Heinz, "Atomically thin MoS 2: a new direct-gap semiconductor," *Physical Review Letters*, vol. 105, no. 13, p. 136805, 2010.

[70] A. Pospischil, M. M. Furchi, and T. Mueller, "Solar-energy conversion and light emission in an atomic monolayer p-n diode.," *Nature nanotechnology*, vol. 9, pp. 257–61, 2014.

[71] Q. H. Wang, K. Kalantar-Zadeh, A. Kis, J. N. Coleman, and M. S. Strano, "Electronics and optoelectronics of two-dimensional transition metal dichalcogenides," *Nature Nanotechnology*, vol. 7, no. 11, pp. 699–712, 2012.

[72] S. Lei, L. Ge, Z. Liu, S. Najmaei, G. Shi, G. You, J. Lou, R. Vajtai, and P. M. Ajayan, "Synthesis and photoresponse of Large GaSe Atomic Layers," *Nano Letters*, vol. 13, pp. 2777–2781, 2013.

[73] L.-D. Zhao, S.-H. Lo, Y. Zhang, H. Sun, G. Tan, C. Uher, C. Wolverton, V. P. Dravid, and M. G. Kanatzidis, "Ultralow thermal conductivity and high thermoelectric figure of merit in SnSe crystals," *Nature*, vol. 508, no. 7496, pp. 373–377, 2014.

[74] S. Balendhran, J. Deng, J. Z. Ou, S. Walia, J. Scott, J. Tang, K. L. Wang, M. R. Field, S. Russo, S. Zhuiykov, M. S. Strano, N. Medhekar, S. Sriram, M. Bhaskaran, and K. Kalantar-zadeh, "Enhanced Charge Carrier Mobility in Two-Dimensional High Dielectric Molybdenum Oxide," *Advanced Materials*, vol. 25, no. 1, pp. 109–114, 2013.

[75] A. Castellanos-Gomez, M. Wojtaszek, N. Tombros, N. Agraït, B. J. van Wees, and G. Rubio-Bollinger, "Atomically Thin Mica Flakes and Their Application as Ultrathin Insulating Substrates for Graphene," *Small*, vol. 7, no. 17, pp. 2491–2497, 2011.

[76] K. S. Novoselov, D. Jiang, F. Schedin, T. J. Booth, V. V. Khotkevich, S. V. Morozov, and A. K. Geim, "Two-dimensional atomic crystals," *Proceedings of the National Academy of Sciences of the United States of America*, vol. 102, no. 30, pp. 10451–10453, 2005.

[77] D. Teweldebrhan and A. A. Balandin, "" Graphene-Like" Exfoliation of Atomically-Thin Films of Bi2Te3 and Related Materials: Applications in Thermoelectrics and Topological Insulators," *ECS Transactions*, vol. 33, no. 13, pp. 103–117, 2010.

[78] S.-H. Lin and J.-L. Kuo, "Towards the ionic limit of two-dimensional materials: monolayer alkaline earth and transition metal halides," *Physical Chemistry Chemical Physics*, vol. 16, no. 38, pp. 20763–20771, 2014.

[79] L. Li, Y. Yu, G. J. Ye, Q. Ge, X. Ou, H. Wu, D. Feng, X. H. Chen, and Y. Zhang, "Black phosphorus field-effect transistors," *Nature Nanotechnology*, vol. 9, no. 5, pp. 372–377, 2014.

[80] K. Takeda and K. Shiraishi, "Theoretical possibility of stage corrugation in Si and Ge analogs of graphite," *Physical Review B*, vol. 50, no. 20, pp. 14916–14922, 1994.

[81] A. Molle, J. Goldberger, M. Houssa, Y. Xu, S.-C. Zhang, and D. Akinwande, "Buckled two-dimensional Xene sheets," *Nature Materials*, vol. 16, 2017.

[82] P. Vogt, P. De Padova, C. Quaresima, J. Avila, E. Frantzeskakis, M. C. Asensio, A. Resta, B. Ealet, and G. Le Lay, "Silicene: Compelling Experimental Evidence for Graphenelike Two-Dimensional Silicon," *Physical Review Letters*, vol. 108, no. 15, p. 155501, 2012.

[83] B. Feng, Z. Ding, S. Meng, Y. Yao, X. He, P. Cheng, L. Chen, and K. Wu, "Evidence of silicene in honeycomb structures of silicon on Ag (111)," *Nano letters*, vol. 12, no. 7, pp. 3507–3511, 2012.

[84] M. E. D. Lay, L. Xian, S. Cahangirov, A. Rubio, and G. Le, "Germanene: a novel two-dimensional germanium allotrope akin to graphene and silicene," *New Journal of Physics*, vol. 16, no. 9, p. 95002, 2014.

[85] F.-f. Zhu, W.-j. Chen, Y. Xu, C.-l. Gao, D.-d. Guan, C.-h. Liu, D. Qian, S.-C. Zhang, and J.-f. Jia, "Epitaxial growth of two-dimensional stanene," *Nature Materials*, vol. advance on, 2015.

[86] L. Tao, E. Cinquanta, D. Chiappe, C. Grazianetti, M. Fanciulli, M. Dubey, A. Molle, and D. Akinwande, "Silicene field-effect transistors operating at room temperature," *Nature Nanotechnology*, vol. 10, no. 3, pp. 227–231, 2015.

[87] N. D. Mermin, "Crystalline order in two dimensions," *Physical Review*, vol. 176, no. 1, p. 250, 1968.

[88] A. K. Geim and K. S. Novoselov, "The rise of graphene," *Nature Materials*, vol. 6, no. 3, pp. 183–191, 2007.

[89] T. Lohmann, K. von Klitzing, and J. H. Smet, "Four-Terminal Magneto-Transport in Graphene p-n Junctions Created by Spatially Selective Doping," *Nano Letters*, vol. 9, no. 5, pp. 1973–1979, 2009.

[90] S. Ryu, L. Liu, S. Berciaud, Y. J. Yu, H. T. Liu, P. Kim, G. W. Flynn, and L. E. Brus, "Atmospheric Oxygen Binding and Hole Doping in Deformed Graphene on a SiO2 Substrate," *Nano Letters*, vol. 10, no. 12, pp. 4944–4951, 2010.

[91] C.-G. Andres, V. Leonardo, P. Elsa, O. I. Joshua, K. L. Narasimha-Acharya, I. B. Sofya, J. G. Dirk, B. Michele, A. S. Gary, J. V. Alvarez, W. Z. Henny, J. J. Palacios, and S. J. v. d. Z. Herre, "Isolation and characterization of few-layer black phosphorus," *2D Materials*, vol. 1, no. 2, p. 25001, 2014.

[92] A. ZurutuzaáElorza, "Highly air stable passivation of graphene based field effect devices," *Nanoscale*, vol. 7, no. 8, pp. 3558–3564, 2015.

[93] D. D. L. Chung, "Review Graphite," *Journal of Materials Science*, vol. 37, no. 8, pp. 1475–1489, 2002.

[94] P. R. Wallace, "THE BAND THEORY OF GRAPHITE," *Physical Review*, vol. 71, no. 9, pp. 622–634, 1947.

[95] S. M. Sze and K. K. Ng, *Physics of semiconductor devices*. John Wiley & Sons, 2006.

[96] R. R. Nair, P. Blake, A. N. Grigorenko, K. S. Novoselov, T. J. Booth, T. Stauber, N. M. R. Peres, and A. K. Geim, "Fine Structure Constant Defines Visual Transparency of Graphene," *Science*, vol. 320, no. 5881, p. 1308, 2008.

[97] J. H. Chen, C. Jang, S. D. Xiao, M. Ishigami, and M. S. Fuhrer, "Intrinsic and extrinsic performance limits of graphene devices on SiO2," *Nature Nanotechnology*, vol. 3, no. 4, pp. 206–209, 2008.

[98] O. V. Yazyev and S. G. Louie, "Electronic transport in polycrystalline graphene," *Nature Materials*, vol. 9, no. 10, pp. 806–809, 2010.

[99] A. Pirkle, J. Chan, A. Venugopal, D. Hinojos, C. W. Magnuson, S. McDonnell, L. Colombo, E. M. Vogel, R. S. Ruoff, and R. M. Wallace, "The effect of chemical residues on the physical and electrical properties of chemical vapor deposited graphene transferred to SiO2," *Applied Physics Letters*, vol. 99, no. 12, p. 122108, 2011.

[100] S. Ahn, D. J. Hwang, H. K. Park, and C. P. Grigoropoulos, "Femtosecond laser drilling of crystalline and multicrystalline silicon for advanced solar cell fabrication," *Applied Physics a-Materials Science & Processing*, vol. 108, no. 1, pp. 113–120, 2012.

[101] K. Watanabe, T. Taniguchi, and H. Kanda, "Direct-bandgap properties and evidence for ultraviolet lasing of hexagonal boron nitride single crystal," *Nature Materials*, vol. 3, no. 6, p. 404, 2004.

[102] Y. Lin and J. W. Connell, "Advances in 2D boron nitride nanostructures: nanosheets, nanoribbons, nanomeshes, and hybrids with graphene," *Nanoscale*, vol. 4, no. 22, pp. 6908–6939, 2012.

[103] R. V. Gorbachev, I. Riaz, R. R. Nair, R. Jalil, L. Britnell, B. D. Belle, E. W. Hill, K. S. Novoselov, K. Watanabe, and T. Taniguchi, "Hunting for monolayer boron nitride: optical and Raman signatures," *Small*, vol. 7, no. 4, pp. 465–468, 2011.

[104] O. Olsvik, O. A. Rokstad, and A. Holmen, "Pyrolysis of methane in the presence of hydrogen," *Chemical engineering & technology*, vol. 18, no. 5, pp. 349–358, 1995.

[105] R. S. Weatherup, B. Dlubak, and S. Hofmann, "Kinetic control of catalytic CVD for high-quality graphene at low temperatures," *Acs Nano*, vol. 6, no. 11, pp. 9996–10003, 2012.

[106] R. S. Weatherup, B. C. Bayer, R. Blume, C. Ducati, C. Baehtz, R. Schlögl, and S. Hofmann, "In Situ Characterization of Alloy Catalysts for Low-Temperature Graphene Growth," *Nano Letters*, vol. 11, no. 10, pp. 4154–4160, 2011.

[107] S. Lee, K. Lee, and Z. Zhong, "Wafer Scale Homogeneous Bilayer Graphene Films by Chemical Vapor Deposition," *Nano Letters*, vol. 10, no. 11, pp. 4702–4707, 2010.

[108] Y. Hao, L. Wang, Y. Liu, H. Chen, X. Wang, C. Tan, S. Nie, J. W. Suk, T. Jiang, T. Liang, J. Xiao, W. Ye, C. R. Dean, B. I. Yakobson, K. F. McCarty, P. Kim, J. Hone, L. Colombo, and R. S. Ruoff, "Oxygen-activated growth and bandgap tunability of large single-crystal bilayer graphene," *Nature Nanotechnology*, vol. 11, no. 5, pp. 426–431, 2016.

[109] S. Caneva, R. S. Weatherup, B. C. Bayer, R. Blume, A. Cabrero-Vilatela, P. Braeuninger-Weimer, M.-B. Martin, R. Wang, C. Baehtz, R. Schloegl, J. C. Meyer, and S. Hofmann, "Controlling catalyst bulk reservoir effects for monolayer hexagonal boron nitride CVD," *Nano Letters*, vol. 16, no. 2, pp. 1250–1261, 2016.

[110] Q. Li, H. Chou, J.-H. Zhong, J.-Y. Liu, A. Dolocan, J. Zhang, Y. Zhou, R. S. Ruoff, S. Chen, and W. Cai, "Growth of Adlayer Graphene on Cu Studied by Carbon Isotope Labeling," *Nano Letters*, vol. 13, no. 2, pp. 486–490, 2013.

[111] P. Braeuninger-Weimer, B. Brennan, A. J. Pollard, and S. Hofmann, "Understanding and controlling Cu-catalyzed graphene nucleation: the role of impurities, roughness, and oxygen scavenging," *Chemistry of Materials*, vol. 28, no. 24, pp. 8905–8915, 2016.

[112] V. Babenko, G. Lane, A. A. Koos, A. T. Murdock, K. So, J. Britton, S. S. Meysami, J. Moffat, and N. Grobert, "Time dependent decomposition of ammonia borane for the controlled production of 2D hexagonal boron nitride," *Scientific Reports*, vol. 7, no. 1, pp. 1–12, 2017.

[113] E. L. Cussler, *Diffusion: mass transfer in fluid systems*. Cambridge university press, 2009.

[114] D. R. Kundu, P. K.; Cohen, I. M.; Dowling, *Fluid Mechanics*. Academic Press, 5 ed., 2012.

[115] M. J. Rand and J. F. Roberts, "Preparation and properties of thin film boron nitride," *Journal of the Electrochemical Society*, vol. 115, no. 4, pp. 423–429, 1968.

[116] M. S. Xu, T. Liang, M. M. Shi, and H. Z. Chen, "Graphene-Like Two-Dimensional Materials," *Chemical Reviews*, vol. 113, no. 5, pp. 3766–3798, 2013.

[117] K. K. Kim, A. Hsu, X. Jia, S. M. Kim, Y. Shi, M. Hofmann, D. Nezich, J. F. Rodriguez-Nieva, M. Dresselhaus, T. Palacios, and J. Kong, "Synthesis of Monolayer Hexagonal Boron Nitride on Cu Foil Using Chemical Vapor Deposition," *Nano Letters*, vol. 12, no. 1, pp. 161–166, 2012.

[118] Y. Gao, W. Ren, T. Ma, Z. Liu, Y. Zhang, W.-B. Liu, L.-P. Ma, X. Ma, and H.-M. Cheng, "Repeated and controlled growth of monolayer, bilayer and few-layer hexagonal boron nitride on Pt foils," *ACS Nano*, vol. 7, no. 6, pp. 5199–5206, 2013.

[119] M. V. Kilday, W. H. Johnson, and E. J. Pros, "Heat of combustion of borazine," *Journal of Research of the National Bureau of Standards*, vol. 65, no. 2, pp. 101–104, 1961.

[120] A. B. Preobrajenski, A. S. Vinogradov, and N. Mårtensson, "Monolayer of h-BN chemisorbed on Cu(1 1 1) and Ni(1 1 1): The role of the transition metal 3d states," *Surface Science*, vol. 582, no. 1-3, pp. 21–30, 2005.

[121] M. T. Paffett, R. J. Simonson, P. Papin, and R. T. Paine, "Borazine adsorption and decomposition at Pt(111) and Ru(001) surfaces," *Surface Science*, vol. 232, no. 3, pp. 286–296, 1990.

[122] N. Alem, R. Erni, C. Kisielowski, M. D. Rossell, W. Gannett, and A. Zettl, "Atomically thin hexagonal boron nitride probed by ultrahigh-resolution transmission electron microscopy," *Physical Review B*, vol. 80, no. 15, p. 155425, 2009.

[123] L. Song, L. Ci, H. Lu, P. B. Sorokin, C. Jin, J. Ni, A. G. Kvashnin, D. G. Kvashnin, J. Lou, and B. I. Yakobson, "Large scale growth and characterization of atomic hexagonal boron nitride layers," *Nano letters*, vol. 10, no. 8, pp. 3209–3215, 2010.

[124] P. R. Kidambi, R. Blume, J. Kling, J. B. Wagner, C. Baehtz, R. S. Weatherup, R. Schloegl, B. C. Bayer, and S. Hofmann, "In situ observations during chemical vapor deposition of hexagonal boron nitride on polycrystalline copper," *Chemistry of Materials*, vol. 26, no. 22, pp. 6380–6392, 2014.

[125] Z. Liu, Y. Gong, W. Zhou, L. Ma, J. Yu, J. C. Idrobo, J. Jung, A. H. MacDonald, R. Vajtai, and J. Lou, "Ultrathin high-temperature oxidation-resistant coatings of hexagonal boron nitride," *Nature communications*, vol. 4, 2013.

[126] F. Müller, K. Stöwe, and H. Sachdev, "Symmetry versus commensurability: epitaxial growth of hexagonal boron nitride on Pt(111) from B-Trichloroborazine (ClBNH)3," *Chemistry of Materials*, vol. 17, no. 13, pp. 3464–3467, 2005.

[127] A. B. Preobrajenski, M. A. Nesterov, M. L. Ng, A. S. Vinogradov, and N. Mårtensson, "Monolayer h-BN on lattice-mismatched metal surfaces: On the formation of the nanomesh," *Chemical Physics Letters*, vol. 446, no. 1-3, pp. 119–123, 2007.

[128] A. B. Preobrajenski, A. S. Vinogradov, M. L. Ng, E. Ćavar, R. Westerström, A. Mikkelsen, E. Lundgren, and N. Mårtensson, "Influence of chemical interaction at the lattice-mismatched interfaces on the overlayer morphology," *Physical Review B*, vol. 75, no. 24, p. 245412, 2007.

[129] G. Kim, A.-R. Jang, H. Y. Jeong, Z. Lee, D. J. Kang, and H. S. Shin, "Growth of High-Crystalline, Single-Layer Hexagonal Boron Nitride on Recyclable Platinum Foil," *Nano Letters*, vol. 13, no. 4, pp. 1834–1839, 2013.

[130] J.-H. Park, J. C. Park, S. J. Yun, H. Kim, D. H. Luong, S. M. Kim, S. H. Choi, W. Yang, J. Kong, K. K. Kim, and Y. H. Lee, "Large-area monolayer hexagonal boron nitride on Pt foil," *ACS Nano*, vol. 8, no. 8, pp. 8520–8528, 2014.

[131] V. Babenko, A. T. Murdock, A. A. Koós, J. Britton, A. Crossley, P. Holdway, J. Moffat, J. Huang, J. A. Alexander-Webber, and R. J. Nicholas, "Rapid epitaxy-free graphene synthesis on silicidated polycrystalline platinum," *Nature communications*, vol. 6, p. 7536, 2015.

[132] M. Morscher, M. Corso, T. Greber, and J. Osterwalder, "Formation of single layer h-BN on Pd (1 1 1)," *Surface science*, vol. 600, no. 16, pp. 3280–3284, 2006.

[133] N. A. Vinogradov, A. A. Zakharov, M. L. Ng, A. Mikkelsen, E. Lundgren, N. Mårtensson, and A. B. Preobrajenski, "One-dimensional corrugation of the h-BN monolayer on Fe (110)," *Langmuir*, vol. 28, no. 3, pp. 1775–1781, 2012.

[134] S. M. Kim, A. Hsu, M. H. Park, S. H. Chae, S. J. Yun, J. S. Lee, D.-H. Cho, W. Fang, C. Lee, and T. Palacios, "Synthesis of large-area multilayer hexagonal boron nitride for high material performance," *Nature communications*, vol. 6, 2015.

[135] C. M. Orofeo, S. Suzuki, and H. Hibino, "Ultrathin Chemical Vapor Deposition (CVD)-Grown Hexagonal Boron Nitride as a High-Quality Dielectric for Tunneling Devices on Rigid and Flexible Substrates," *The Journal of Physical Chemistry C*, vol. 118, no. 6, pp. 3340–3346, 2014.

[136] P. Sutter, J. Lahiri, P. Albrecht, and E. Sutter, "Chemical vapor deposition and etching of high-quality monolayer hexagonal boron nitride films," *ACS nano*, vol. 5, no. 9, pp. 7303–7309, 2011.

[137] M. Corso, W. Auwärter, M. Muntwiler, A. Tamai, T. Greber, and J. Osterwalder, "Boron nitride nanomesh," *Science*, vol. 303, no. 5655, pp. 217–220, 2004.

[138] F. Müller, S. Hüfner, H. Sachdev, R. Laskowski, P. Blaha, and K. Schwarz, "Epitaxial growth of hexagonal boron nitride on Ag(111)," *Physical Review B*, vol. 82, no. 11, p. 113406, 2010.

[139] M. Beller, A. Renken, and R. A. van Santen, "Catalysis: from principles to applications," 2012.

[140] O. Deutschmann, H. Knözinger, K. Kochloefl, and T. Turek, "Heterogeneous catalysis and solid catalysts, 1. Fundamentals," *Ullmann's Encyclopedia of Industrial Chemistry*, 2000.

[141] J. K. Nørskov, T. Bligaard, J. Rossmeisl, and C. H. Christensen, "Towards the computational design of solid catalysts," *Nature chemistry*, vol. 1, no. 1, p. 37, 2009.

[142] J. Robertson, "Heterogeneous catalysis model of growth mechanisms of carbon nanotubes, graphene and silicon nanowires," *Journal of Materials Chemistry*, vol. 22, no. 37, pp. 19858–19862, 2012.

[143] R. S. Weatherup, A. J. Shahani, Z.-J. Wang, K. Mingard, A. J. Pollard, M.-G. Willinger, R. Schloegl, P. W. Voorhees, and S. Hofmann, "In situ graphene growth dynamics on polycrystalline catalyst foils," *Nano Letters*, vol. 16, no. 10, pp. 6196–6206, 2016.

[144] R.-J. Chang, X. Wang, S. Wang, Y. Sheng, B. Porter, H. Bhaskaran, and J. H. Warner, "Growth of Large Single-Crystalline Monolayer Hexagonal Boron Nitride by Oxide-Assisted Chemical Vapor Deposition," *Chemistry of Materials*, 2017.

[145] J. S. Bunch, S. S. Verbridge, J. S. Alden, A. M. van der Zande, J. M. Parpia, H. G. Craighead, and P. L. McEuen, "Impermeable atomic membranes from graphene sheets," *Nano Letters*, vol. 8, no. 8, pp. 2458–2462, 2008.

[146] S. Böhm, "Graphene against corrosion," *Nature nanotechnology*, vol. 9, no. 10, p. 741, 2014.

[147] M. Schriver, W. Regan, W. J. Gannett, A. M. Zaniewski, M. F. Crommie, and A. Zettl, "Graphene as a Long-Term Metal Oxidation Barrier: Worse Than Nothing," *ACS Nano*, vol. 7, no. 7, pp. 5763–5768, 2013.

[148] C. Cui, A. T. O. Lim, and J. Huang, "A cautionary note on graphene anti-corrosion coatings," *Nature Nanotechnology*, vol. 12, no. 9, pp. 834–835, 2017.

[149] M.-B. Martin, B. Dlubak, R. S. Weatherup, M. Piquemal-Banci, H. Yang, R. Blume, R. Schlögl, S. Collin, F. Petroff, and S. Hofmann, "Protecting nickel with graphene spin-filtering membranes: A single layer is enough," *Applied Physics Letters*, vol. 107, no. 1, p. 12408, 2015.

[150] M. Piquemal-Banci, R. Galceran, F. Godel, S. Caneva, M.-B. Martin, R. S. Weatherup, P. R. Kidambi, K. Bouzehouane, S. Xavier, and A. Anane, "Insulator-to-metallic spin-filtering in 2D-magnetic tunnel junctions based on hexagonal boron nitride," *ACS nano*, 2018.

[151] P. R. Kidambi, B. C. Bayer, R. Blume, Z. J. Wang, C. Baehtz, R. S. Weatherup, M. G. Willinger, R. Schloegl, and S. Hofmann, "Observing graphene grow: catalyst-graphene interactions during scalable graphene growth on polycrystalline copper," *Nano Letters*, vol. 13, no. 10, pp. 4769–4778, 2013.

[152] R. Blume, P. R. Kidambi, B. C. Bayer, R. S. Weatherup, Z.-J. Wang, G. Weinberg, M.-G. Willinger, M. Greiner, S. Hofmann, A. Knop-Gericke, and R. Schlogl, "The influence of intercalated oxygen on the properties of graphene on polycrystalline Cu under various environmental conditions," *Physical Chemistry Chemical Physics*, vol. 16, no. 47, pp. 25989–26003, 2014.

[153] R. S. Weatherup, L. D'Arsié, A. Cabrero-Vilatela, S. Caneva, R. Blume, J. Robertson, R. Schloegl, and S. Hofmann, "Long-term passivation of strongly interacting metals with single-layer graphene," *Journal of the American Chemical Society*, vol. 137, no. 45, pp. 14358–14366, 2015.

[154] S. Caneva, M. B. Martin, L. D'Arsié, A. I. Aria, H. Sezen, M. Amati, L. Gregoratti, H. Sugime, S. Esconjauregui, J. Robertson, S. Hofmann, and R. S. Weatherup, "From Growth Surface to Device Interface: Preserving Metallic Fe under Monolayer Hexagonal Boron Nitride," *ACS Applied Materials and Interfaces*, vol. 9, no. 35, pp. 29973–29981, 2017.

[155] I. Pasternak, A. Krajewska, K. Grodecki, I. Jozwik-Biala, K. Sobczak, and W. Strupinski, "Graphene films transfer using marker-frame method," *Aip Advances*, vol. 4, no. 9, p. 97133, 2014.

[156] W.-H. Lin, T.-H. Chen, J.-K. Chang, J.-I. Taur, Y.-Y. Lo, W.-L. Lee, C.-S. Chang, W.-B. Su, and C.-I. Wu, "A direct and polymer-free method for transferring graphene grown by chemical vapor deposition to any substrate," *ACS nano*, vol. 8, no. 2, pp. 1784–1791, 2014.

[157] R. S. Weatherup, B. Eren, Y. Hao, H. Bluhm, and M. B. Salmeron, "Graphene Membranes for Atmospheric Pressure Photoelectron Spectroscopy," *The Journal of Physical Chemistry Letters*, vol. 7, no. 9, pp. 1622–1627, 2016.

[158] J. Zhang, L. Lin, L. Sun, Y. Huang, A. L. Koh, W. Dang, J. Yin, M. Wang, C. Tan, and T. Li, "Clean Transfer of Large Graphene Single Crystals for High-Intactness Suspended Membranes and Liquid Cells," *Advanced Materials*, vol. 29, no. 26, 2017.

[159] T. Yoon, W. C. Shin, T. Y. Kim, J. H. Mun, T.-S. Kim, and B. J. Cho, "Direct measurement of adhesion energy of monolayer graphene as-grown on copper and its application to renewable transfer process," *Nano Letters*, vol. 12, no. 3, pp. 1448–1452, 2012.

[160] J.-H. Lee, E. K. Lee, W.-J. Joo, Y. Jang, B.-S. Kim, J. Y. Lim, S.-H. Choi, S. J. Ahn, J. R. Ahn, M.-H. Park, C.-W. Yang, B. L. Choi, S.-W. Hwang, and D. Whang, "Wafer-scale growth of single-crystal monolayer graphene on reusable hydrogen-terminated germanium," *Science*, vol. 344, no. 6181, pp. 286–289, 2014.

[161] L. Gao, W. Ren, H. Xu, L. Jin, Z. Wang, T. Ma, L.-P. Ma, Z. Zhang, Q. Fu, L.-M. Peng, X. Bao, and H.-M. Cheng, "Repeated growth and bubbling transfer of graphene with millimetre-size single-crystal grains using platinum," *Nature Communications*, vol. 3, p. 699, 2012.

[162] L. Liu, X. Liu, Z. Zhan, W. Guo, C. Xu, J. Deng, D. Chakarov, P. Hyldgaard, E. Schröder, A. Yurgens, and J. Sun, "Graphene Transfer: A Mechanism for Highly Efficient Electrochemical Bubbling Delamination of CVD-Grown Graphene from Metal Substrates (Adv. Mater. Interfaces 8/2016)," *Advanced Materials Interfaces*, vol. 3, no. 8, pp. n/a–n/a, 2016.

[163] D. Wang, I. Huang, P. Ho, S. Li, Y. Yeh, D. Wang, W. Chen, Y. Lee, Y. Chang, and C. Chen, "Clean-Lifting Transfer of Large-area Residual-Free Graphene Films," *Advanced Materials*, vol. 25, no. 32, pp. 4521–4526, 2013.

[164] X. Li, Y. Zhu, W. Cai, M. Borysiak, B. Han, D. Chen, R. D. Piner, L. Colombo, and R. S. Ruoff, "Transfer of Large-Area Graphene Films for High-Performance Transparent Conductive Electrodes," *Nano Letters*, vol. 9, no. 12, pp. 4359–4363, 2009.

[165] J. Song, F.-Y. Kam, R.-Q. Png, W.-L. Seah, J.-M. Zhuo, G.-K. Lim, P. K. H. Ho, and L.-L. Chua, "A general method for transferring graphene onto soft surfaces.," *Nature Nanotechnology*, vol. 8, pp. 356–62, 2013.

[166] J. D. Wood, G. P. Doidge, E. A. Carrion, J. C. Koepke, J. A. Kaitz, I. Datye, A. Behnam, J. Hewaparakrama, B. Aruin, and Y. Chen, "Annealing free, clean graphene transfer using alternative polymer scaffolds," *Nanotechnology*, vol. 26, no. 5, p. 55302, 2015.

[167] M. Ishigami, J. H. Chen, W. G. Cullen, M. S. Fuhrer, and E. D. Williams, "Atomic Structure of Graphene on SiO2," *Nano Letters*, vol. 7, no. 6, pp. 1643–1648, 2007.

[168] G. Lupina, J. Kitzmann, I. Costina, M. Lukosius, C. Wenger, A. Wolff, S. Vaziri, M. Östling, I. Pasternak, A. Krajewska, W. Strupinski, S. Kataria, A. Gahoi, M. C. Lemme, G. Ruhl, G. Zoth, O. Luxenhofer, and W. Mehr, "Residual metallic contamination of transferred chemical vapor deposited graphene," *ACS Nano*, vol. 9, no. 5, pp. 4776–4785, 2015.

[169] M. Jang, T. Q. Trung, J.-h. Jung, B.-y. Kim, and N.-e. Lee, "Improved performance and stability of field-effect transistors with polymeric residue-free graphene channel transferred by gold layer.," *Physical chemistry chemical physics : PCCP*, vol. 16, pp. 4098–105, 2014.

[170] H. H. Kim, B. Kang, J. W. Suk, N. Li, K. S. Kim, R. S. Ruoff, W. H. Lee, and K. Cho, "Clean Transfer of Wafer-Scale Graphene via Liquid Phase Removal of Polycyclic Aromatic Hydrocarbons," *ACS Nano*, 2015.

[171] R. S. Weatherup, C. Baehtz, B. Dlubak, B. C. Bayer, P. R. Kidambi, R. Blume, R. Schloegl, and S. Hofmann, "Introducing Carbon Diffusion Barriers for Uniform, High-Quality Graphene Growth from Solid Sources," *Nano Letters*, vol. 13, no. 10, pp. 4624–4631, 2013.

[172] C. J. L. de la Rosa, J. Sun, N. Lindvall, M. T. Cole, Y. Nam, M. Löffler, E. Olsson, K. B. K. Teo, and A. Yurgens, "Frame assisted H2O electrolysis induced H2 bubbling transfer of large area graphene grown by chemical vapor deposition on Cu," *Applied Physics Letters*, vol. 102, no. 2, p. 22101, 2013.

[173] C. T. Cherian, F. Giustiniano, I. Martin-Fernandez, H. Andersen, J. Balakrishnan, and B. Özyilmaz, "Bubble-Free Electrochemical Delamination of CVD Graphene Films," *Small*, vol. 11, no. 2, pp. 189–194, 2015.

[174] L. Liu, X. Liu, Z. Zhan, W. Guo, C. Xu, J. Deng, D. Chakarov, P. Hyldgaard, E. Schröder, and A. Yurgens, "A mechanism for highly efficient electrochemical bubbling delamination of CVD-grown graphene from metal substrates," *Advanced Materials Interfaces*, vol. 3, no. 8, p. 150049, 2015.

[175] L. Song, L. Ci, W. Gao, and P. M. Ajayan, "Transfer printing of graphene using gold film," *ACS nano*, vol. 3, no. 6, pp. 1353–1356, 2009.

[176] A. V. Zaretski and D. J. Lipomi, "Processes for non-destructive transfer of graphene: widening the bottleneck for industrial scale production," *Nanoscale*, vol. 7, no. 22, pp. 9963–9969, 2015.

[177] S. Franssila, *Introduction to microfabrication*. John Wiley & Sons, 2010.

[178] R. Egerton, *Physical principles of electron microscopy: an introduction to TEM, SEM, and AEM*. Springer Science & Business Media, 2006.

[179] Y. Yao, Q. Fu, Y. Y. Zhang, X. Weng, H. Li, M. Chen, L. Jin, A. Dong, R. Mu, and P. Jiang, "Graphene cover-promoted metal-catalyzed reactions," *Proceedings of the National Academy of Sciences*, vol. 111, no. 48, pp. 17023–17028, 2014.

[180] M. L. Ng, A. Shavorskiy, C. Rameshan, A. Mikkelsen, E. Lundgren, A. Preobrajenski, and H. Bluhm, "Reversible modification of the structural and electronic properties of a boron nitride monolayer by CO intercalation," *ChemPhysChem*, vol. 16, no. 5, pp. 923–927, 2015.

[181] K. Takahashi, K. Yamada, H. Kato, H. Hibino, and Y. Homma, "In situ scanning electron microscopy of graphene growth on polycrystalline Ni substrate," *Surface Science*, vol. 606, no. 7-8, pp. 728–732, 2012.

[182] J. Luo, P. Tian, C.-T. Pan, A. W. Robertson, J. H. Warner, E. W. Hill, and G. A. D. Briggs, "Ultralow secondary electron emission of graphene," *ACS nano*, vol. 5, no. 2, pp. 1047–1055, 2011.

[183] P. Riccardi, A. Cupolillo, M. Pisarra, A. Sindona, and L. S. Caputi, "Primary energy dependence of secondary electron emission from graphene adsorbed on Ni (111)," *Applied Physics Letters*, vol. 101, no. 18, p. 183102, 2012.

[184] G. Haugstad, *Atomic force microscopy: understanding basic modes and advanced applications*. John Wiley & Sons, 2012.

[185] P. Vandenabeele, *Practical Raman spectroscopy: an introduction*. John Wiley & Sons, 2013.

[186] A. C. Ferrari, J. C. Meyer, V. Scardaci, C. Casiraghi, M. Lazzeri, F. Mauri, S. Piscanec, D. Jiang, K. S. Novoselov, S. Roth, and a. K. Geim, "Raman Spectrum of Graphene and Graphene Layers," *Physical Review Letters*, vol. 97, no. 18, p. 187401, 2006.

[187] L. M. Malard, M. A. Pimenta, G. Dresselhaus, and M. S. Dresselhaus, "Raman spectroscopy in graphene," *Physics Reports*, vol. 473, no. 5–6, pp. 51–87, 2009.

[188] A. C. Ferrari and D. M. Basko, "Raman spectroscopy as a versatile tool for studying the properties of graphene," *Nature Nanotechnology*, vol. 8, no. 4, pp. 235–246, 2013.

[189] J. E. Lee, G. Ahn, J. Shim, Y. S. Lee, and S. Ryu, "Optical separation of mechanical strain from charge doping in graphene," *Nature Communications*, vol. 3, no. May, pp. 1024–1028, 2012.

[190] S. Berciaud, S. Ryu, L. E. Brus, and T. F. Heinz, "Probing the intrinsic properties of exfoliated graphene: Raman spectroscopy of free-standing monolayers," *Nano letters*, vol. 9, no. 1, pp. 346–352, 2008.

[191] C. Neumann, L. Banszerus, M. Schmitz, S. Reichardt, J. Sonntag, T. Taniguchi, K. Watanabe, B. Beschoten, and C. Stampfer, "Line shape of the Raman 2D peak of graphene in van der Waals heterostructures," *physica status solidi (b)*, 2016.

[192] C. Neumann, S. Reichardt, P. Venezuela, M. Drogeler, L. Banszerus, M. Schmitz, K. Watanabe, T. Taniguchi, F. Mauri, B. Beschoten, S. V. Rotkin, and C. Stampfer, "Raman spectroscopy as probe of nanometre-scale strain variations in graphene," *Nature Communications*, vol. 6, p. 8429, 2015.

[193] Q. Cai, D. Scullion, A. Falin, K. Watanabe, T. Taniguchi, Y. Chen, E. J. G. Santos, and L. H. Li, "Raman signature and phonon dispersion of atomically thin boron nitride," *Nanoscale*, vol. 9, no. 9, pp. 3059–3067, 2017.

[194] R. Wu, L. Gan, X. Ou, Q. Zhang, and Z. Luo, "Detaching graphene from copper substrate by oxidation-assisted water intercalation," *Carbon*, vol. 98, pp. 138–143, 2016.

[195] B. Luo, P. R. Whelan, A. Shivayogimath, D. M. A. Mackenzie, P. Boggild, and T. J. Booth, "Copper Oxidation Through Nucleation Sites of Chemical Vapor Deposited Graphene," *Chemistry of Materials*, vol. 28, no. 11, pp. 3789–3795, 2016.

[196] R. Wang, P. R. Whelan, P. Braeuninger-Weimer, S. Tappertzhofen, J. A. Alexander-Webber, Z. A. Van-Veldhoven, P. R. Kidambi, B. S. Jessen, T. J. Booth, and P. Boggild, "Catalyst interface engineering for improved 2D film lift-off and transfer," *ACS Applied Materials & Interfaces*, 2016.

[197] P. R. Kidambi, C. Ducati, B. Dlubak, D. Gardiner, R. S. Weatherup, M. B. Martin, P. Seneor, H. Coles, and S. Hofmann, "The Parameter Space of Graphene Chemical Vapor Deposition on Polycrystalline Cu," *Journal of Physical Chemistry C*, vol. 116, no. 42, pp. 22492–22501, 2012.

[198] T. Oishi, M. Goto, A. Kasahara, and M. Tosa, "Low frictional copper oxide film prepared with sodium hydroxide solution," *Surface and interface analysis*, vol. 36, no. 8, pp. 1259–1261, 2004.

[199] G. Niaura, "Surface-enhanced Raman spectroscopic observation of two kinds of adsorbed OH- ions at copper electrode," *Electrochimica Acta*, vol. 45, no. 21, pp. 3507–3519, 2000.

[200] D. S. Bodas and S. A. Gangal, "Poly (methyl methacrylate) as masking material for microelectromechanical system (MEMS) fabrication," *Journal of applied polymer science*, vol. 102, no. 3, pp. 2094–2098, 2006.

[201] C. A. Chavarin, A. A. Sagade, D. Neumaier, G. Bacher, and W. Mertin, "On the origin of contact resistances in graphene devices fabricated by optical lithography," *Applied Physics A*, vol. 122, no. 2, pp. 1–5, 2016.

[202] Y.-C. Lin, C.-C. Lu, C.-H. Yeh, C. Jin, K. Suenaga, and P.-W. Chiu, "Graphene Annealing: How Clean Can It Be?," *Nano Letters*, vol. 12, no. 1, pp. 414–419, 2012.

[203] G.-H. Lee, R. C. Cooper, S. J. An, S. Lee, A. van der Zande, N. Petrone, A. G. Hammerberg, C. Lee, B. Crawford, and W. Oliver, "High-strength chemical-vapor-deposited graphene and grain boundaries," *Science*, vol. 340, no. 6136, pp. 1073–1076, 2013.

[204] Z. A. Van Veldhoven, J. A. Alexander-Webber, A. A. Sagade, P. Braeuninger-Weimer, and S. Hofmann, "Electronic properties of CVD graphene: The role of grain boundaries, atmospheric doping, and encapsulation by ALD," *physica status solidi (b)*, 2016.

[205] A. G. F. Garcia, M. Neumann, F. Amet, J. R. Williams, K. Watanabe, T. Taniguchi, and D. Goldhaber-Gordon, "Effective Cleaning of Hexagonal Boron Nitride for Graphene Devices," *Nano Letters*, vol. 12, no. 9, pp. 4449–4454, 2012.

[206] A. Zwick and R. Carles, "Multiple-order Raman scattering in crystalline and amorphous silicon," *Physical Review B*, vol. 48, no. 9, pp. 6024–6032, 1993.

[207] W.-H. Yang, V. F. Smolen, and N. A. Peppas, "Oxygen permeability coefficients of polymers for hard and soft contact lens applications," *Journal of Membrane Science*, vol. 9, no. 1, pp. 53–67, 1981.

[208] M. Pourbaix, *Atlas of electrochemical equilibria in aqueous solutions*. Pergamon press, 1966.

[209] K. R. Trethewey and J. Chamberlain, *Corrosion for science and engineering*. NACE International, Houston, TX (United States), 1988.

[210] H. G. Yan, D. H. Song, K. F. Mak, I. Chatzakis, J. Maultzsch, and T. F. Heinz, "Time-resolved Raman spectroscopy of optical phonons in graphite: Phonon anharmonic coupling and anomalous stiffening," *Physical Review B*, vol. 80, no. 12, 2009.

[211] T. E. Brown, H. E. H. LeMay, B. E. Bursten, and C. Murphy, *Chemistry The Central Science 13th Edition*. Prentice Hall, 2014.

[212] S. Y. Yang, J. G. Oh, D. Y. Jung, H. Choi, C. H. Yu, J. Shin, C.-G. Choi, B. J. Cho, and S.-Y. Choi, "Metal-Etching-Free Direct Delamination and Transfer of Single-Layer Graphene with a High Degree of Freedom," *Small*, vol. 11, no. 2, pp. 175–181, 2015.

[213] J.-K. Choi, J. Kwak, S.-D. Park, H. D. Yun, S.-Y. Kim, M. Jung, S. Y. Kim, K. Park, S. Kang, S.-D. Kim, D.-Y. Park, D.-S. Lee, S.-K. Hong, H.-J. Shin, and S.-Y. Kwon, "Growth of Wrinkle-Free Graphene on Texture-Controlled Platinum Films and Thermal-Assisted Transfer of Large-Scale Patterned Graphene," *ACS Nano*, vol. 9, no. 1, pp. 679–686, 2015.

[214] M. Piquemal-Banci, R. Galceran, M.-B. Martin, F. Godel, A. Anane, F. Petroff, B. Dlubak, and P. Seneor, "2D-MTJs: introducing 2D materials in magnetic tunnel junctions," *Journal of Physics D: Applied Physics*, vol. 50, no. 20, p. 203002, 2017.

[215] C. B. Alcock, V. P. Itkin, and M. K. Horrigan, "Properties of the elements and inorganic compounds, vapour pressure of metallic elements," *Can. Met. Q*, vol. 23, pp. 309–313, 1984.

[216] W. Hayne, *Melting, boiling, triple, and critical points of the elements*. CRC Press, 2016.

[217] R. Wang, D. G. Purdie, Y. Fan, F. C.-P. Massabuau, P. Braeuninger-Weimer, O. J. Burton, R. Blume, R. Schloegl, A. Lombardo, R. S. Weatherup, and S. Hofmann, "A Peeling Approach for Integrated Manufacturing of Large Mono-Layer h-BN Crystals," *ACS Nano*, 2019.

[218] H. Bluhm, M. Havecker, A. Knop-Gericke, M. Kiskinova, R. Schlogl, M. Salmeron, M. Hävecker, A. Knop-Gericke, M. Kiskinova, R. Schlögl, and M. Salmeron, "In situ x-ray photoelectron spectroscopy studies of gas-solid interfaces at near-ambient conditions," *Mrs Bulletin*, vol. 32, no. 12, pp. 1022–1030, 2007.

[219] L. Wang, I. Meric, P. Y. Huang, Q. Gao, Y. Gao, H. Tran, T. Taniguchi, K. Watanabe, L. M. Campos, D. A. Muller, J. Guo, P. Kim, J. Hone, K. L. Shepard, and C. R. Dean, "One-dimensional electrical contact to a two-dimensional material," *Science*, vol. 342, no. 6158, pp. 614–617, 2013.

[220] D. G. Purdie, N. M. Pugno, T. Taniguchi, K. Watanabe, A. C. Ferrari, and A. Lombardo, "Cleaning interfaces in layered materials heterostructures," *arXiv preprint arXiv:1803.00912*, 2018.

[221] R. Trehan, Y. Lifshitz, and J. W. Rabalais, "Auger and x-ray electron spectroscopy studies of h-BN, c-BN, and N2 ion irradiation of boron and boron nitride," *Journal of Vacuum Science & Technology A: Vacuum, Surfaces, and Films*, vol. 8, no. 6, pp. 4026–4032, 1990.

[222] T. Ma, W. Ren, Z. Liu, L. Huang, L. P. Ma, X. Ma, Z. Zhang, L. M. Peng, and H. M. Cheng, "Repeated growth-etching-regrowth for large-area defect-free single-crystal graphene by chemical vapor deposition," *ACS Nano*, vol. 8, no. 12, pp. 12806–12813, 2014.

[223] B. Predel, "B-Pt (Boron-Platinum): Datasheet from Landolt-Börnstein - Group IV Physical Chemistry · Volume 5B: "B-Ba - C-Zr" in SpringerMaterials (http://dx.doi.org/10.1007/10040476_380)."

[224] S. Tanuma, C. J. Powell, and D. R. Penn, "Calculations of electron inelastic mean free paths. IX. Data for 41 elemental solids over the 50 eV to 30 keV range," *Surface and Interface Analysis*, vol. 43, no. 3, pp. 689–713, 2011.

[225] S. Saadi, F. Abild-Pedersen, S. Helveg, J. Sehested, B. Hinnemann, C. C. Appel, and J. K. Nørskov, "On the role of metal step-edges in graphene growth," *Journal of Physical Chemistry C*, vol. 114, no. 25, pp. 11221–11227, 2010.

[226] A. Nagashima, N. Tejima, Y. Gamou, T. Kawai, and C. Oshima, "Electronic structure of monolayer hexagonal boron nitride physisorbed on metal surfaces," *Physical Review Letters*, vol. 75, no. 21, pp. 3918–3921, 1995.

[227] R. Westerström, A. Mikkelsen, E. Lundgren, and A. Preobrajenski, "A single h-BN layer on Pt (1 1 1)," 2008.

[228] L. Brown, E. B. Lochocki, J. Avila, C. J. Kim, Y. Ogawa, R. W. Havener, D. K. Kim, E. J. Monkman, D. E. Shai, H. I. Wei, M. P. Levendorf, M. Asensio, K. M. Shen, and J. Park, "Polycrystalline graphene with single crystalline electronic structure," *Nano Letters*, vol. 14, no. 10, pp. 5706–5711, 2014.

[229] V. L. Nguyen, B. G. Shin, D. L. Duong, S. T. Kim, D. Perello, Y. J. Lim, Q. H. Yuan, F. Ding, H. Y. Jeong, H. S. Shin, S. M. Lee, S. H. Chae, Q. A. Vu, S. H. Lee, and Y. H. Lee, "Seamless stitching of graphene domains on polished copper (111) foil," *Advanced Materials*, vol. 27, no. 8, pp. 1376–1382, 2015.

[230] X. Xu, Z. Zhang, J. Dong, D. Yi, J. Niu, M. Wu, L. Lin, R. Yin, M. Li, J. Zhou, S. Wang, J. Sun, X. Duan, P. Gao, Y. Jiang, X. Wu, H. Peng, R. S. Ruoff, Z. Liu, D. Yu, E. Wang, F. Ding, and K. Liu, "Ultrafast epitaxial growth of metre-sized single-crystal graphene on industrial Cu foil," *Science Bulletin*, vol. 62, no. 15, pp. 1074–1080, 2017.

[231] C. V. Thompson, "Grain growth in thin films," *Annual Review of Materials Science*, vol. 20, no. 1, pp. 245–268, 1990.

[232] D. S. Lee, D. Y. Park, H. J. Woo, S. H. Kim, J. Ha, and E. Yoon, "Preferred orientation controlled giant grain growth of platinum thin films on SiO 2/Si substrates," *Japanese Journal of Applied Physics, Part 2: Letters*, vol. 40, no. 1 A/B, pp. 10–13, 2001.

[233] T. Gladman, *Grain size control*. OCP science Philadelphia, Pa/USA, 2004.

[234] F. J. Humphreys and M. Hatherly, *Recrystallization and related annealing phenomena*. Elsevier, 2012.

[235] G. Beck and C. Bachmann, "Oxygen removal at grain boundaries in platinum films on YSZ," *Solid State Ionics*, vol. 262, pp. 508–511, 2014.

[236] M. H. Kim, T.-S. Park, E. Yoon, D.-S. Lee, D.-Y. Park, H.-J. Woo, D.-I. Chun, and J. Ha, "Changes in preferred orientation of Pt thin films deposited by DC magnetron sputtering using Ar/O2 gas mixtures," *Journal of Materials Research*, vol. 14, no. 04, pp. 1255–1260, 1999.

[237] J. Preußner, E. Fleischmann, R. Völkl, and U. Glatzel, "Enrichment of boron at grain boundaries of platinum-based alloys determined by electron energy loss spectroscopy in a transmission electron microscope," *International Journal of Materials Research*, vol. 101, no. 5, pp. 577–579, 2010.

[238] J. R. Davis, *Copper and copper alloys*. ASM international, 2001.

[239] L. Schué, I. Stenger, F. Fossard, A. Loiseau, and J. Barjon, "Characterization methods dedicated to nanometer-thick hBN layers," *2D Materials*, vol. 4, no. 1, p. 015028, 2017.

[240] A. C. Ferrari, "Raman spectroscopy of graphene and graphite: Disorder, electron-phonon coupling, doping and nonadiabatic effects," *Solid State Communications*, vol. 143, no. 1-2, pp. 47–57, 2007.